eman ta zabal zazu

Universidad del País Vasco

Euskal Herriko Unibertsitatea

Pectin-based adsorbents for remediation of contaminated water with pharmaceutical products and heavy metals

Ph.D. Thesis submitted by Javier Martínez Sabando to the University of the Basque Country

Supervisor:

Dra. Silvina Cerveny

Donostia-San Sebastián, June 2023

Abstract

On our planet, we can see water in all its forms: gaseous in the clouds, solid in the glaciers, or liquid in rivers or seas. Water is essential for life on Earth since it adequately regulates the environment's temperature and, therefore, becomes a factor that determines the survival of fauna and flora. In humans, water is directly related to transporting nutrients, eliminating toxins, lubricating tissues, and participating in chemical and metabolic reactions. We can raise animals, farm, wash food, or maintain good hygiene with water.

Until the 20th century, water was considered an inexhaustible resource. However, the growth of the world population and climate change have meant that in the 21st century, it has become a scarce commodity. In addition, the available water is contaminated mainly by human activities such as agriculture, livestock, and industry and partially by natural reasons such as volcanic eruptions. In this context, it has become crucial to have methodologies or systems that allow us to decontaminate or remediate the water we have efficiently and economically.

This thesis will focus on developing adsorbents for the remediation of contaminated freshwater. While there are many different types of contaminants, I will focus on "emerging contaminants," a collection of molecules found in freshwater that encompass personal care products, drugs, pesticides, and other industrial chemicals. In fact, during 2023, the European and Spanish regulations for drinking water will include an extensive list of these contaminants.

Heavy metals come from natural sources (such as the erosion of rocks composed of heavy metals or volcanic eruptions) or human activity (mining and industrial discharges). Prolonged water consumption contaminated by heavy metals can cause serious health problems since they cannot be metabolized and accumulate in specific tissues. Different government entities (such as the European Union (EU), the World Health Organization (WHO), and the Environmental Protection Agency (EPA, United States) have established the maximum concentrations allowed in drinking water for each type of metal.

Pharmaceuticals come strictly from human activity. The primary sources of antibiotic contamination are the effluents from factories producing hospitals and personal use of these compounds. However, the most significant discharge comes from veterinary use in livestock and aquaculture productions. The biggest problem with the presence of antibiotics in drinking water is the risk of contributing to the generation of resistant bacteria. These bacteria can develop genes for resistance to these antibiotics, with the resulting chance that if a person becomes ill with this type of bacteria, the antibiotics to which the bacterium has been exposed will have no effect in

remitting the infection. Regarding regulation, more research is still needed to determine the limits of antibiotics levels in fresh water and the potential damage that these can cause in the long term.

Among the most modern treatments to mitigate the impact of emerging contaminants in water are ultraviolet irradiation, bio-electrochemical systems, oxidative processes, membrane filtration, and adsorption. This thesis has chosen adsorption due to its low cost, simple design, low energy requirement, and biodegradability of the materials used. Another premise that we have used is the non-use of nanoparticles.

This thesis will focus on the adsorption method to mitigate the impact of emerging pollutants. Adsorption is a phenomenon in which molecules, atoms, or ions present in an aqueous solution are retained on the surface of a solid material through chemical or physical interactions. Numerous adsorbents, such as activated carbon, zeolites, and mineral clays, have been developed to treat contaminated water.

The material chosen for adsorption is pectin. Pectin is a heteropolysaccharide present in the cell wall of higher plants. It is found in large quantities in fruits. It is a very economical material since it can be extracted from discards generated by the juice industry (citrus peels or apple pulp). This way, a discard is reused to give it a second use, thus stimulating the circular economy. In addition, it is a biodegradable material.

This thesis is divided into eight chapters. The first four chapters include a general introduction to the problem of water contamination and the current remediation methods. Chapter 3 introduces the pectin molecule and its main characteristics, such as transformations after being crosslinked. The experimental techniques used in this thesis are presented in Chapter 4.

Chapters 5 to 8 include the central core of this thesis. Chapter 5 discusses the effect of pectin crosslinking using calcium ions, europium ions, and the two ions simultaneously. To study the crosslinking process, adsorption isotherms and kinetics were performed. In addition, scanning electron microscopy (SEM) with the coupled energy dispersive X-ray spectroscopy (EDX) technique was used to perform morphological analysis and analyze the presence of crosslinking agents. Infrared spectroscopy (FT-IR) and X-ray diffraction analysis (XDR) were used to study the structural properties of the generated materials. These techniques revealed structural differences between the three materials, reflected in the three structural models proposed in the same section. Finally, tests were carried out on the swelling behavior of the materials, an essential property for their subsequent use in aqueous media for the remediation of heavy metals and drugs.

Chapter 6 evaluates pectin-based adsorbents crosslinked with calcium ions. First, the degree of methyl esterification was analyzed using infrared spectroscopy (FT-IR). The performance to adsorb barium using inductively coupled plasma atomic emission spectroscopy

(ICP-AES) was evaluated in parallel. The results indicate that the lower the degree of methyl esterification, the higher the adsorption yield. Next, barium adsorptions were carried out at different pH (4 to 10), revealing few differences in adsorption. pH = 7 was established for the rest of the experiments since it is the pH at which drinking water is normally found. The material morphology was studied once the barium adsorption process was finished, and adsorption kinetics and isotherms were carried out to determine the effect of the adsorbent doses and adsorption kinetics to evaluate the effect of the initial barium concentration. On the other hand, the adsorptive effectiveness of the calcium crosslinked material against nickel and zinc individually and simultaneously was evaluated at concentrations in the µg/L range (concentrations at which these contaminants appear in the environment). Subsequently, we evaluated the reusability of the film. Finally, the removal capacity of the material based on pectin crosslinked at different times was evaluated against chlorpheniramine maleate (antihistamine). For this, adsorption kinetics tests were carried out, determining the concentration of the drug through ultraviolet-visible spectroscopy (UV-VIS). Good results were obtained with this material, which, to the best of our knowledge, has not previously been reported as capable of effectively adsorbing these kinds of molecules.

In Chapter 7, the adsorption capacity of pectin crosslinked with europium and with calcium and europium is analyzed. The contaminants used are zinc and antibiotics (ciprofloxacin and tetracycline). The results obtained for zinc adsorption were also compared with those obtained for calcium-crosslinked pectin. The material with the best results was crosslinked with calcium to remove divalent metals. Regarding the results obtained for removing ciprofloxacin and tetracycline, the best results come from the crosslinked material with the two agents because it has a higher europium content responsible for the interaction with these antibiotics. Finally, tests of isotherms and adsorption kinetics of the crosslinked material with calcium and europium were carried out to remove zinc and tetracycline from the aqueous medium. It was determined that the material is a good candidate to use as a joint adsorbent for heavy metals (divalent) and antibiotics in aqueous media.

Finally, in Chapter 8, the general conclusions of the research carried out in this doctoral thesis are detailed, and possible future lines of research are explored.

Resumen

En nuestro planeta podemos ver agua en todas sus formas: gaseosa en las nubes, sólida en los glaciares, o líquida en ríos o mares. El agua es trascendental para la vida en la tierra ya que regula la temperatura del medio ambiente adecuadamente y, por lo tanto, se convierte en un factor que determina la supervivencia de la fauna y flora. En los seres humanos, el agua está directamente relacionada con el transporte de nutrientes, la eliminación de toxinas o la lubricación de tejidos participando en las reacciones químicas y en las reacciones metabólicas. Sin agua no podríamos además criar animales, cultivar, lavar los alimentos o mantener una buena higiene.

Hasta el siglo XX el agua se ha considerado un recurso inagotable. Sin embargo, el crecimiento de la población mundial y el cambio climático han provocado que en el siglo XXI se haya convertido en un bien escaso. Además, el agua disponible está contaminada fundamentalmente por actividades humanas como la agricultura, ganadería, industria y, parcialmente por razones naturales como erupciones volcánicas. En este contexto se ha vuelto crucial disponer de metodologías o sistemas que permitan de una manera eficiente y económica descontaminar o remediar el agua que disponemos.

Esta tesis se centrará en el desarrollo de adsorbentes para la remediación de agua dulce contaminada. Si bien existen muchos tipos de contaminantes diferentes, me concentraré en los llamados “contaminantes emergentes”, una colección de moléculas presente en agua dulce que engloban los productos de cuidado personal, fármacos, plaguicidas y otros productos químicos industriales. De hecho, durante 2023 las regulaciones europeas y españolas del agua para consumo incluirán una extensa lista de estos contaminantes.

Los metales pesados proceden de fuentes naturales (como la erosión de rocas compuestas por metales pesados o las erupciones volcánicas) o por actividad humana (la minería y los vertidos industriales). El consumo prolongado de agua contaminada por metales pesados puede acarrear serios problemas de salud, ya que no se pueden metabolizar y se acumulan en tejidos específicos. Diferentes entidades gubernamentales (Unión Europea (UE), la Organización Mundial para la Salud (OMS) o la *Environmental Protection Agency* (EPA, Estados Unidos) han establecido las concentraciones máximas permitidas en agua potable para cada tipo de metal.

En lo que se refiere a los fármacos, estos provienen estrictamente de la actividad humana. Las principales fuentes de contaminación por antibióticos son los efluentes de las fábricas

productoras de hospitales y del uso personal de estos compuestos. Sin embargo, el mayor vertido proviene del uso veterinario en producciones ganaderas y acuícolas. El mayor problema de la incorporación de antibióticos en el agua es el riesgo de contribuir a la generación de bacterias resistentes. Estas bacterias pueden desarrollar genes de resistencia hacia esos antibióticos, con el resultante riesgo de que, si una persona se enferma con este tipo de bacterias, los antibióticos a los cuales ha estado expuesta esa bacteria no tendrán efecto para remitir la infección. En cuanto a la regulación, aun se necesita más investigación para determinar los límites de antibióticos en agua y el daño potencial que estos pueden causar a largo plazo.

Entre los tratamientos más modernos para la mitigación del impacto de contaminantes emergentes en agua se encuentran la irradiación ultravioleta, sistemas bio-electroquímicos, procesos oxidativos, filtración por membrana y adsorción. En esta tesis, se ha elegido la adsorción debido a su bajo coste, diseño simple, bajo requerimiento energético y bio-degradablilidad de los materiales empleados. Otra premisa que hemos utilizado es la no utilización de nano-partículas.

Esta tesis se centrará en el método de adsorción para mitigar el impacto de los contaminantes emergentes. La adsorción es un fenómeno en el que moléculas, átomos o iones presentes en una solución acuosa se retienen en la superficie de un material sólido por medio de interacciones químicas o físicas. Numerosos tipos de adsorbentes han sido desarrollados para el tratamiento de aguas contaminadas, como el carbón activado, zeolitas o arcillas minerales.

El material base elegido para la adsorción es la pectina. La pectina es un heteropolisacárido presente en la pared celular de plantas superiores. Se encuentra en grandes cantidades en frutos. Es un material económico ya que se puede extraer de descartes que genera la industria del zumo (cáscaras de cítricos o la pulpa de la manzana). De esta manera se reaprovecha un descarte para darle un segundo uso, por lo que se estimula la economía circular. Además, se trata de un material biodegradable.

La presente tesis está dividida en 8 capítulos. Los primeros 2 capítulos incluyen una introducción general al problema de la contaminación agua, así como a los métodos de remediación utilizados actualmente. En el capítulo 3 se introduce la molécula de pectina y sus principales características como las transformaciones que sufre cuando es reticulada con diferentes agentes. Las técnicas experimentales empleadas en esta tesis se presentan en el capítulo 4.

Los capítulos 5 a 8 incluyen el núcleo principal de esta tesis. El capítulo 5, analiza el efecto de la reticulación (o *crosslinking*) de pectina utilizando iones de calcio, iones de europio y los dos iones (es decir, primero reticulacion con calcio y luego con europio). Para estudiar el proceso de reticulación, se realizaron isotermas y cinéticas de adsorción. Además, se realizaron análisis de microscopía electrónica de barrido (SEM) con la técnica de espectroscopia de rayos X

de energía dispersiva (EDX) acoplada que permite realizar análisis morfológico, así como confirmar la presencia de los agentes reticulantes. Para estudiar las propiedades estructurales de los materiales generados se empleó la espectroscopia infrarroja (FT-IR) y análisis por difracción de rayos X (XDR). Estas técnicas revelaron diferencias estructurales entre los 3 materiales los cuales se ven reflejados en los tres modelos estructurales propuestos en el capítulo 5. Finalmente, se realizaron ensayos de comportamiento de *swelling* de los materiales desarrollados, propiedad importante para el posterior empleo de ellos en medios acuosos para la remediación de metales pesados y fármacos.

En el capítulo 6, se evalúan los adsorbentes basados en pectina reticulados con el ion calcio. Para ello, primeramente, se analizó el grado de metilesterificación por medio de espectroscopia infrarroja (FT-IR). Paralelamente se evaluó el rendimiento para adsorber bario utilizando espectroscopia de emisión atómica por plasma acoplado inductivamente (ICP-AES). Los resultados indican que cuanto más bajo es el grado de metilesterificación, mayor rendimiento de adsorción. A continuación, se realizaron adsorciones de bario a diferentes pH (4 a 10), revelando pocas diferencias en términos de adsorción. Se estableció pH = 7 para el resto de experimentos ya que es el pH al que normalmente se encuentra el agua de consumo. Se estudió morfología del material una vez terminado el proceso de adsorción de bario, se llevaron a cabo cinéticas e isotermas de adsorción para determinar el efecto de las dosis de adsorbente y cinéticas de adsorción para evaluar el efecto de la concentración inicial de bario. Por otro lado, se evaluó la efectividad adsortiva del material reticulado con calcio contra níquel y zinc individual y simultáneamente a concentraciones en el rango de µg/L (concentraciones a las que aparecen estos contaminantes en el ambiente). Posteriormente, evaluamos la reusabilidad del film durante 5 ciclos sucesivos. Por último, se evaluó la capacidad de remoción del material basado en pectina a diferentes tiempos de reticulación contra clorfeniramina maleato (antihistamínico). Para ello se realizaron ensayos de cinética de adsorción determinando la concentración del fármaco a través de espectroscopia ultravioleta visible (UV-VIS) Se obtuvieron buenos resultados con este material, que, hasta donde sabemos, no se ha reportado anteriormente como capaz de adsorber efectivamente este tipo de moléculas.

En el capítulo 7 se analiza la capacidad de adsorción de pectina reticulada con europio y con calcio y europio conjuntamente. Los contaminantes utilizados son zinc y antibióticos (ciprofloxacina y tetraciclina). Los resultados obtenidos para la adsorción de zinc también se compararon con los obtenidos por la pectina reticulada con calcio. Se concluyó que, para la remoción de metales divalentes, el material con mejor resultados fue el reticulado con calcio. En cuanto a los resultados obtenidos para la remoción de ciprofloxacina y tetraciclina, los mejores resultados provienen del material reticulado con los dos agentes, debido a que este tiene mayor contenido de europio, el cual es el responsable de la interacción con estos antibióticos. Por último,

se realizaron ensayos de isotermas y cinéticas de adsorción del material entrecruzado con calcio y europio para la remoción simultánea de zinc y tetraciclina de medio acuoso. Se determinó que el material es un buen candidato para emplear como adsorbente conjunto de metales pesados (divalentes) y antibióticos de medios acuosos.

Finalmente, en el capítulo 8 se desarrollan las conclusiones generales de la investigación realizada en esta tesis doctoral y se exploran los posibles estudios futuros a realizar.

Contents

Chapter 1

Water Pollution

In this chapter, we introduce the topic of water pollution. This is not a particular problem of a region or country. Instead, water is polluted on the whole planet and depending on the area, different contaminants are more critical. Therefore, we present the classification of the different types of pollutants, with particular emphasis on emerging contaminants. In this chapter, we also analyze the pathways by which these contaminants reach the water, and the possible problems they generate for the people and ecosystems are discussed. Finally, we will focus on pharmaceutical compounds and heavy metals.

Social and economic development is dependent on water, as it is a crucial element for the sustenance of every human being. Water plays a pivotal role in the growth of crops, maintaining good health, and ensuring safety. Additionally, the economic prosperity of our society is linked to water, and currently, there is no alternative to this indispensable resource on the earth's surface. Water plays a critical role in the accomplishment of the Sustainable Development Goals (SDG, see Figure 1). One of the goals is entirely dedicated to water remediation (Goal 6, “Ensure availability and sustainable management of water and sanitation for all”). It plays a vital role in several SDGs and is a fundamental component of others. Regardless, as a result of the climate change effects, which are currently being experienced[1], water is turning into a more limited and unexpectedly available resource in numerous world areas[2]. Water shortage is part of the main problems the world will face in the XXI century, which is already affecting all continents.

Population growth is leading to pressure on the existing water on the planet earth (the demand for water in food production is increasing), the depletion of freshwater resources by

various industries, and the impacts of climate change. Access to clean drinking water is becoming increasingly scarce as the population grows and the environment is affected by climate change. Over 1300 children under five years old die on a daily basis as a consequence of unsafe drinking water, poor sanitation and hygiene[3]. It is estimated that by 2030, the demand for drinking water will increase up to 40%, which will create more pressure on areas where water is scarce. In addition, there will be a 50% increase in energy demand, which will exacerbate the strain on water resources as 90% of power generation relies on water. This will lead to a global water crisis, making it imperative to secure access to freshwater for all.

Figure 1. The Sustainable Development Goals, adopted on 25 September 2015 as a part of the 2030 Agenda.

When water becomes polluted, the task of eliminating the contaminants becomes challenging, expensive, and frequently unachievable. An impressive 80 percent of the world's wastewater remains untreated, comprising a wide range of substances from human waste to perilous industrial discharges. The presence and quantity of pollutants in freshwater dictate its appropriateness for essential human activities like drinking, bathing, and agriculture. Furthermore, the pollution of freshwater ecosystems can harm fish and other wildlife's habitat and overall well-being.

Pollution within freshwater ecosystems encompasses a range of elements, including pathogens derived mainly from human and animal waste, organic matter such as plant nutrients from agricultural run-off (e.g., nitrogen or phosphorus), chemical pollutants, and salinity resulting from irrigation, domestic wastewater, and mine run-off into rivers. Additionally, the proliferation of plastic pollution and emerging contaminants like pharmaceuticals pose an escalating threat to

our planet's water bodies. However, the precise extent and consequences of their presence in freshwater remain largely undisclosed.

1.1 Types of pollutants

Attending to the nature of the pollutant, there are various types and they are sorted in by the next categories: organic pollutants, inorganic impurities, radiological contaminants, suspended solids, pathogens, and thermal pollution[4].

1.1.1 Organic pollutants

The organic pollutants stem from human activities such as wastewater, urban wastewater, industrial wastewater, and agricultural waste. The organic compounds include carbon, hydrogen, oxygen, nitrogen, and sulfur[5].

Organic pollutants from agricultural sources, including fertilizers, manure, pesticides, sediment, pharmaceuticals, and household products like detergents and soaps, are the main contributors to highly dispersed pollution in rivers, streams, and estuaries. Excessive use of fertilizers, manure, and nutrients, containing nitrogen and phosphorus, leads to the development of low-oxygen eutrophic areas[6], commonly known as “dead” zones, rapidly expanding globally. Eutrophication is the excessive enrichment of nutrients in an aquatic ecosystem, reducing the biological demand for oxygen due to the overgrowth of algae and aquatic plants. This leads losing water quality and aquatic biodiversity (plants and animals)[7]. Excessive urban and industrial activities also exacerbate eutrophication by introducing organic molecules into the ecosystem.

1.1.2. Inorganic pollutants

Inorganic pollutants are classified as nonmetallic inorganic pollutants (chlorides, asbestos, fluorides…) and metallic pollutants (antimony, barium, cadmium, lead…)[8]. In the case of metal pollution, mostly from mining and technology manufacturing is another growing threat, especially in developing countries that lack environmental regulations and adequate wastewater treatment infrastructures.

1.1.3. Radiological pollutants

Radiological contaminants are chemicals with an unbalanced number of neutrons and protons resulting in unstable atoms that can emit ionizing radiation. Radioactive pollutants can come from the Earth's crust or different human activities related to radioactivity, such as nuclear plants, manufacturing, and nuclear weapon testing. Radioactive isotopes include thorium, plutonium, cesium, or uranium.

1.1.4. Suspended solids

Any solid material or particles suspended in water that can be removed from the water by filtration or centrifugation are referred to as suspended solids in water pollution. These particles may be silt, organic matter, microplastics, or other substances that enter the water due to human activity or natural processes. Suspended particles can affect water quality by obstructing light, raising turbidity, and changing the water's chemical makeup. They can also harm aquatic life by blocking eating, respiration and reducing the amount of available habitat. To gauge the overall health of marine ecosystems, regulatory bodies employ suspended solids, a crucial water quality measure[9].

1.1.5. Pathogens

Pathogens are microorganisms that cause disease, such as bacteria, fungi, viruses and other parasites[10]. The consumption of water contaminated with this type of infectious agents has a significant impact on public health. Around 80% of diseases, especially in developing countries, are caused by the consumption of water contaminated by pathogens[11].

1.1.6. Thermal pollution

Lastly, thermal pollution consists of altering the temperature of the water, usually caused by the discharge of hot water from thermal power plants for energy production[12]. These thermic variations affect severely to aquatic fauna and flora.

1.2. Emerging pollutants

A fundamental environmental challenge posed by water contamination is the presence of the so-called emerging contaminants (such as cosmetics, pharmaceutical products, microplastics, surfactants, food additives, rare earth elements, industrial chemicals, heavy metals, metalloids, pesticides, etc.), which reduce drinking water quality drastically.

Emerging contaminants are substances that are not yet regulated for monitoring or public reporting their occurrence in our water supply or wastewater, leaving potential risks to human and environmental health[13]. This is why many emerging contaminants are distributed in the categories of the above classification. The complex molecular structure and elusive detection and removal of emerging contaminants have made them a significant area of interest in water remediation research (see Figure 2 for a list of compounds). It is important to note that until 2022 these emerging contaminants were not included in the European Union (EU) regulations related to water quality. Starting this year, 2023, these emerging contaminants are partially included in the substances that the administration of each EU country should monitor. The new official gazette of the Spanish state (Boletin Oficial del Estado)[14] from January 10th 2023 announces the

incorporation of 25 emerging contaminant substances, including: 9 pharmaceuticals, 1 biocide for domestic use, and 12 pesticides.

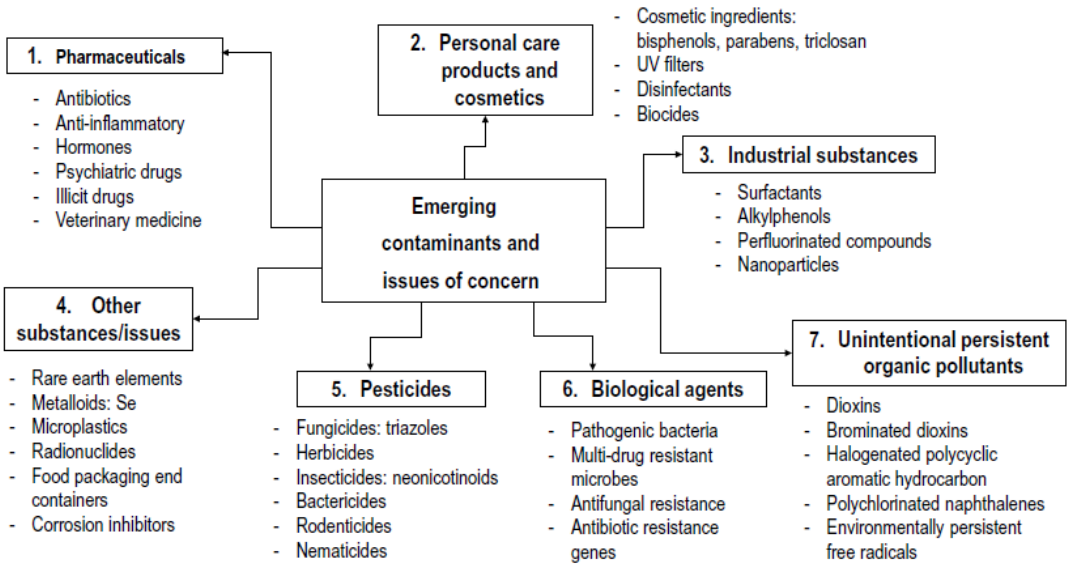

Figure 2. Classification of potential hazards and emerging pollutants in water compartments, figure extracted from[13].

Plastic waste (among emergent pollutants), especially micro-plastics, is another growing concern, with the most significant footprint existing in the industrial sectors of Asia[15]

In the past 20 years, pharmaceuticals (including personal care products) and heavy metals in water has significantly increased, leading to their recognition as significant environmental contaminants. Our research will focus on pharmaceutical compounds and heavy metals as emerging pollutants, considering their high occurrence and propensity to evade the decontamination procedures of wastewater treatment plants.

1.2.1. Pharmaceuticals

The occurrence of pharmaceuticals in surface water, groundwater, tap water and drinking water happens globally. A global study tested the presence of 713 different Active Pharmaceutical Ingredients (APIs) across the earth; 631 pharmaceuticals were detected above the detection limit of the used technique in the range of µg/L-ng/L[16]. A recent study sampled rivers from 137 geographic sites across the world for 61 different APIs. It was found that at 25.7% of the sampling sites, the concentrations of at least one API exceeded the safe levels for aquatic organisms, or raised concerns regarding the selection of genes for antimicrobial resistance[17]. We need to consider, for instance, that the EU takes second place for pharmaceutical sales for human and veterinary consumption on a global scale, Figure 3 shows a study of the number of

pharmaceuticals detected in tap water, drinking water surface, and groundwater across 2015. Moreover, there is a growing tendency towards their usage. Consequently, numerous reports have surfaced regarding the pollution of Europe's water systems by pharmaceuticals[17] [18]. Some examples are the feminization of fish[19] [20] or high antibiotic levels in the water [21].

There are various pathways through which pharmaceuticals may infiltrate the environment[22], such as agricultural runoff, urban, and industrial waste. Drugs used by humans are mainly released from wastewater treatment plants (WWTP)[22]; on the other hand, excretion is how veterinary antibiotics are released into water. This is because antibiotics are not fully metabolized and may maintain their antibiotic activity. Figure 4 shows the lifecycle of pharmaceuticals from their creation to their introduction into the aquatic ecosystem.

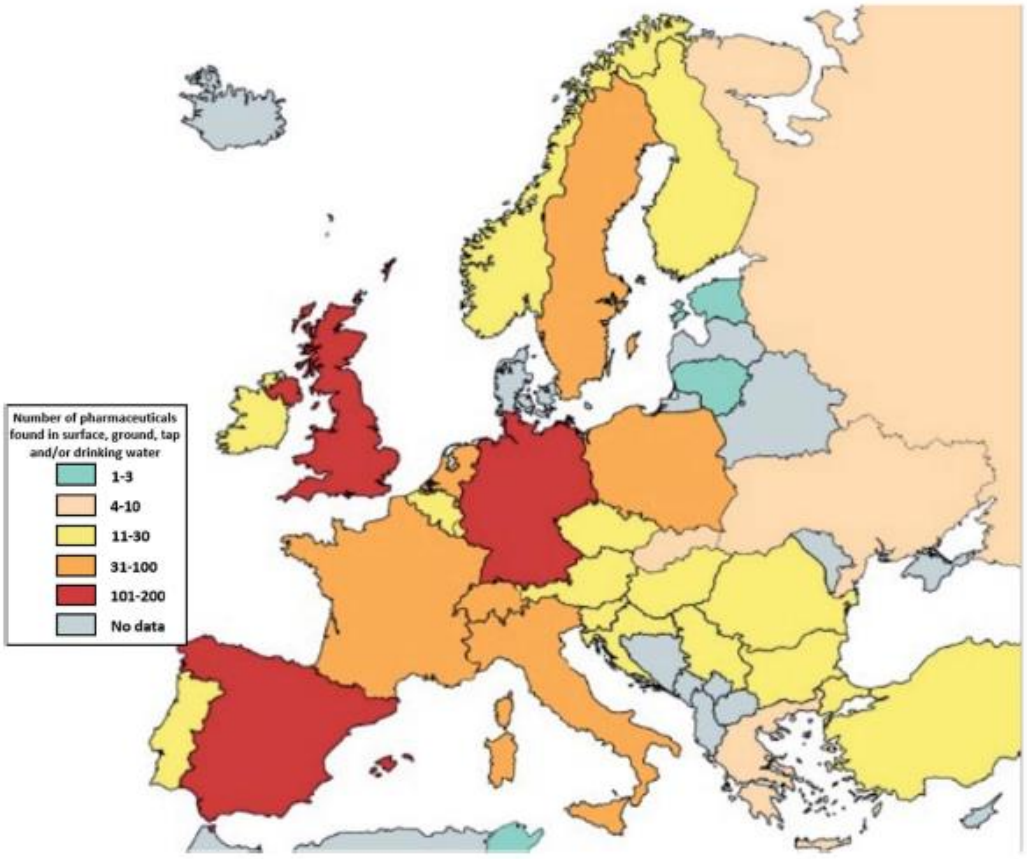

Figure 3. Number of pharmaceuticals detected in tap water, drinking water, surface water, and groundwater across the European Union during 2015. Figure taken from[17]

Regarding antibiotics, approximately 80 to 90% of the quantities consumed are expelled from the body and discharged into the environment, polluting water and soil[23]. As a result, the development of bacterial resistance raises the likelihood of toxicity when consuming this water, which could affect aquatic organisms, animals and humans[24]. Hence, a combination of antibiotics and their byproducts make their way into the sewage system and ultimately reach the WWTP, where complete removal is impossible. As a result, antibiotics have the potential to enter into natural aquatic systems such as sewage sludge, soils, and surface waters, which may be challenging to prevent. Antibiotic and antifungal medications being present can potentially expedite the proliferation and transmission of resistant bacteria and fungi, ultimately posing a threat to human well-being. Today, it is crucial to recognize that there is a lack of conclusive proof linking pharmaceuticals in the environment to any direct impact on human health. As mentioned before, the new Spanish regulation is including the nine pharmaceuticals to concern list.

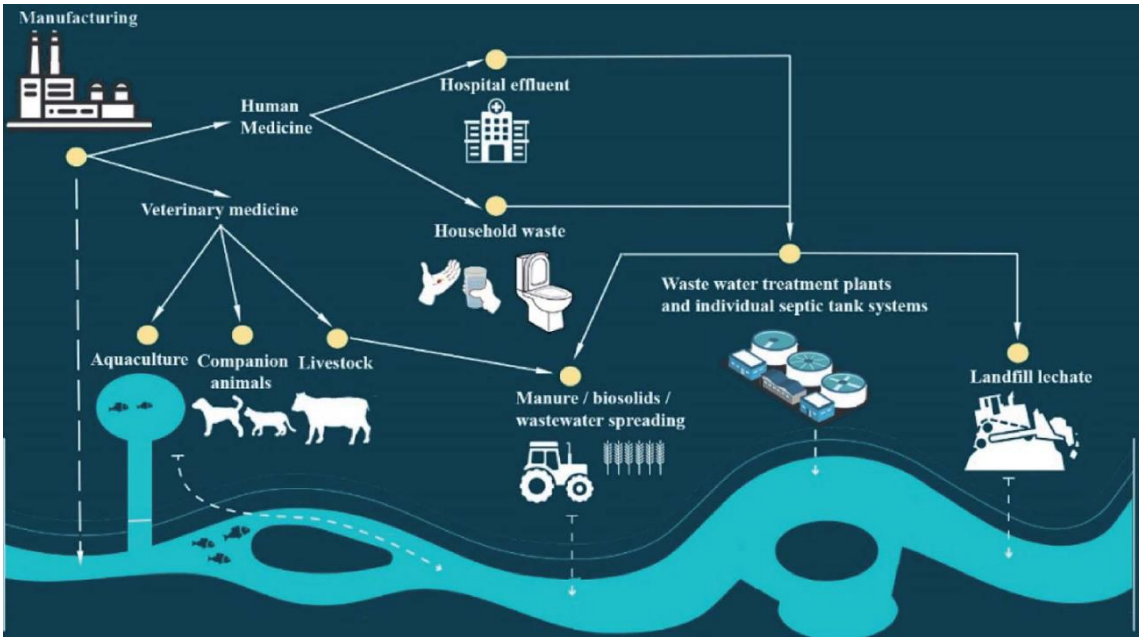

Figure 4. Pathways adopted by pharmaceuticals from their manufacture to the water bodies. Figure extracted from[17].

These are the followings: two Nonsteroidal anti-inflammatory drugs (NSAIDs) (diclofenac and Ibuprofen); one antiepileptic (carbamazepine); three antibiotics (clarithromycin, erythromycin, azithromycin); three estrogenic hormones (17 alpha-ethinylestradiol, 17 beta-estradiol, estrone). Besides the control of sulfamethoxazole and carbamazepine in groundwater is going to be added.

Regarding environmental impact of pharmaceuticals, a research investigation carried out in Asian rivers revealed the presence of chlorpheniramine in both the surface water and fish inhabiting those environments.. Tilapia fish displayed plasmatic chlorpheniramine concentrations

of 1.3 to 4.2 ng/mL, whereas the water contained a concentration of 2.6 ng/L of this antihistamine compound[25].

Nonetheless, vulnerable populations' potential long-term exposure to pharmaceuticals in the environment has been discussed by the World Health Organization (WHO)[26]. More research still needs to be done to comprehend and evaluate pharmaceutical products concerning their environmental concentrations and levels of risk[27].

1.2.2. Heavy metals

Lately, reports have also emerged regarding heavy metals, such as lead, zinc, arsenic, cadmium, mercury, chromium, and nickel. Despite a significant reduction in heavy metal discharges from industries into European water bodies between 2010 and 2020, thanks to Regulations[28] , similar decreases have not been observed in other regions, such as America or Asia. Furthermore, irrespective of industrial waste, some aspects like arsenic are naturally found in rocks and can accumulate in various aquifers[29].

Unlike medications, heavy metals occur naturally in the Earth's crust. They are brought to the surface environment through geological phenomena, such as volcanic eruptions or human activities like mining, smelting, and pesticide use. Technological processes, such as those employed by industries producing color pigments or alloys, have also contributed to heavy metal contamination in water bodies. Metals and metalloids are carried to surface and groundwater through leaching, infiltration, and runoff processes. After their release into aquatic systems, they typically become adsorbed by sediment particles, but they may also become re-released during storms or other extreme weather occurrences. Heavy metals, in water bodies do not undergo chemical degradation like other pollutants but persist in the water for a prolonged time. The presence of heavy metals in water can introduce diverse health issues[30 31] , including the risk of cancer and diabetes, skin lesions, renal injuries, cardiovascular disorders, neurotoxicity, and neuronal damage, among others.

For example, The consumption of water contaminated with heavy metals can have detrimental effects on human health. For instance, zinc exposure can lead to various symptoms such as pain, skin inflammation, fever, vomiting, anemia, while nickel exposure can result in dry cough, chest pain, breathing difficulties, nausea, diarrhea, skin eruptions, pulmonary fibrosis, gastrointestinal discomfort, and renal edema[32]. These examples highlight the range of adverse health impacts that can arise from the ingestion of water contaminated with heavy metals.

Due to all the facts exposed above, the United States Environmental Protection Agency (US EPA)[33], the World Health Organization (WHO)[34] and the European Union (EU)[35] elaborated

guidelines establishing a maximum contaminant level in drinking water (see Table 1). These guidelines are created based on a review of the available scientific evidence considering the health effects of exposure to them, the feasibility of treatment and monitoring, and the economic and social impacts of implementing the guidelines. Contrasting with heavy metals, EPA and WHO have not elaborated this type of guidelines for pharmaceuticals yet, given the complexity of the problem. There are many different pharmaceuticals with a wide range of chemical properties and potential health effects. They are difficult to measure because they are present in very low concentrations (µg/L-ng/L) and the difficulty in identifying and regulating specific sources of contamination makes this task complex. Although they recognize the emergent concern about the presence of pharmaceuticals in water for human consumption, they have recommended using a risk-based approach to the problem.

The multitude of water-related risks has significant social and financial implications. Despite considerable financial consequences, they are not typically factored into everyday business expenses. Global economic systems often consider water an inexhaustible and undervalued resource by the, resulting in extensive misuse and wastage. In terms of social impact, the effects of pollution can be far-reaching and devastating, including the displacement of densely populated communities and the subsequent impoverishment of those relocated, an increase in illness rates, a widening gap between urban and rural areas, and potential conflicts among various stakeholders.

Table 1. Maximum Contaminant Level (MCL*[1]) established by United States Environmental Protection Agency (US EPA*[2]), World Health Organization (WHO*[3]), and European Union (EU) Guideline 2020/2184, metal symbol and most common oxidation states.

Heavy Metal	**Symbol**	**Oxidation states**	**MCL*[1] US EPA*[2] [mg/L]**	**MCL*[1] WHO*[3] [mg/L]**	**MCL*[1] EU*[3] [mg/L]**
Aluminum	Al	+3	0.05 - 0.2	-	0.2
Antimony	Sb	+3, +5	0.006	0.02	0.01
Arsenic	As	-3, +3, +5	0.010	0.01	0.01
Barium	Ba	+2	2.0	0.7	-
Beryllium	Be	+2	0.004	-	-
Cadmium	Cd	+2	0.005	0.003	0.005
Chromium	Cr	+3, +6	0.1	0.05	0.05
Cobalt	Co	+2, +3	0.05	0.05	0.025
Copper	Cu	+1, +2	1.3	2.0	-
Iron	Fe	+2, +3, +6	0.3	0.3	2.0
Lead	Pb	+2	0.015	0.01	0.2
Manganese	Mn	+3, +4, +7	0.05	0.4	0.01
Mercury	Hg	+1, +2	0.002	0.006	0.05
Nickel	Ni	+2	0.1	0.07	0.001
Selenium	Se	-2, +4, +6	0.05	0.04	0.02
Thallium	Tl	+1, +3	0.002	-	0.02
Zinc	Zn	0, +2	5.0	3.0	-

REFERENCES

1. Hugonnet, R. *et al.* Accelerated global glacier mass loss in the early twenty-first century. *Nature* **592**, 726–731 (2021).

2. Mekonnen, M. M. & Hoekstra, A. Y. Sustainability: Four billion people facing severe water scarcity. *Sci. Adv.* **2**, 1–7 (2016).

3. Unicef. *Pneumonia and diarrhoea*. *United Nations Children's Fund* (2012).

4. Singh, J., Yadav, P., Pal, A. K. & Mishra, V. *Water Pollutants: Origin and Status*. (2020). doi:10.1007/978-981-15-0671-0_2

5. Sharma, A. *et al.* Carbon nano-structures and functionalized associates: Adsorptive detoxification of organic and inorganic water pollutants. *Inorg. Chem. Commun.* **141**, (2022).

6. Yu, L. & Gan, J. Mitigation of Eutrophication and Hypoxia through Oyster Aquaculture: An Ecosystem Model Evaluation off the Pearl River Estuary. *Environ. Sci. Technol.* **55**, 5506–5514 (2021).

7. Wurtsbaugh, W. A., Paerl, H. W. & Dodds, W. K. Nutrients, eutrophication and harmful algal blooms along the freshwater to marine continuum. *Wiley Interdiscip. Rev. Water* **6**, 1–27 (2019).

8. Verma, P. & Ratan, J. K. *Assessment of the negative effects of various inorganic water pollutants on the biosphere—an overview*. *Inorganic Pollutants in Water* (INC, 2020). doi:10.1016/B978-0-12-818965-8.00005-6

9. Fankhauser, R. *et al.* Sediment contamination assessment in urban areas based on total suspended solids. **7**, (2012).

10. Edwin Malefane, M., John Mafa, P., Thokozani Innocent Nkambule, T., Elizabeth Managa, M. & Tawanda Kuvarega, A. Modulation of Z-scheme photocatalysts for pharmaceuticals remediation and pathogen inactivation: Design devotion, concept examination, and developments. *Chem. Eng. J.* **452**, 138894 (2023).

11. *WHO Global Water, Sanitation and Hygiene*. (2020).

12. Kalinowska, M. B. Effect of water–air heat transfer on the spread of thermal pollution in rivers. *Acta Geophys.* **67**, 597–619 (2019).

13. Morin, N. *et al.* Worldwide cases of water pollution by emerging contaminants : a review. *Environ. Chem. Lett.* **20**, 2311–2338 (2022).

14. Ministerio de la Presidencia, R. con las C. y M. D. Royal Decree 3/2023, of January 10, which establishes the technical-sanitary criteria for the quality of drinking water, its control and supply. *Boletín Of. del Estado, núm 9* 4253–4354 (2023).

15. Mihai, F. C. *et al.* Plastic Pollution, Waste Management Issues, and Circular Economy Opportunities in Rural Communities. *Sustain.* **14**, (2022).

16. aus der Beek, T. *et al.* Pharmaceuticals in the environment—Global occurrences and perspectives. *Environ. Toxicol. Chem.* **35**, 823–835 (2016).

17. Flynn, D. O. *et al.* Analytical Methods A review of pharmaceutical occurrence and pathways in the aquatic environment in the context of a changing climate and the COVID-19 pandemic. 575–594 (2021). 8

18. Molnar, E. & Maasz, G. Environmental risk assessment of pharmaceuticals at a seasonal holiday destination in the largest freshwater shallow lake in Central Europe. 59233–59243 (2021).

19. Jobling, S. *et al.* Predicted exposures to steroid estrogens in U.K. Rivers correlate with widespread sexual disruption in wild fish populations. *Environ. Health Perspect.* **114**, 32–39 (2006).

20. Vilela, C. L. S., Bassin, J. P. & Peixoto, R. S. Water contamination by endocrine disruptors: Impacts, microbiological aspects and trends for environmental protection. *Environ. Pollut.* **235**, 546–559 (2018).

21. Polverino, G. *et al.* Psychoactive pollution suppresses individual differences in fish behaviour. *Proc. R. Soc. B Biol. Sci.* **288**, (2021).

22. Carvalho, I. T. & Santos, L. Antibiotics in the aquatic environments: A review of the European scenario. *Environ. Int.* **94**, 736–757 (2016).

23. Tomczyk, A., Kubaczyński, A. & Szewczuk-Karpisz, K. Assessment of agricultural waste biochars for remediation of degraded water-soil environment: Dissolved organic carbon release and immobilization of impurities in one- or two-adsorbate systems. *Waste Manag.* **155**, 87–98 (2023).

24. Scaria, J., Anupama, K. V. & Nidheesh, P. V. Tetracyclines in the environment: An overview on the occurrence, fate, toxicity, detection, removal methods, and sludge management. *Sci. Total Environ.* **771**, 145291 (2021).

25. Nozaki, K. *et al.* Pharmaceuticals and personal care products (PPCPs) in surface water and fish from three Asian countries: Species-specific bioaccumulation and potential ecological risks. *Sci. Total Environ.* **866**, 161258 (2023).

26. Maycock, D. S. & Watts, C. D. Pharmaceuticals in Drinking Water. *Encycl. Environ. Heal.* 472–484 (2011). doi:10.1016/B978-0-444-52272-6.00457-8

27. Ågerstrand, M. *et al.* Improving environmental risk assessment of human pharmaceuticals. *Environ. Sci. Technol.* **49**, 5336–5345 (2015).

28. Maire, É., Adrien, J. & Petit, C. Structural characterization of solid foams. *Comptes Rendus Phys.* **15**, 674–682 (2014).

29. Podgorski, J. & Berg, M. Global threat of arsenic in groundwater. *Science (80-.).* **368**, 845–850 (2020).

30. Mitra, S. *et al.* Impact of heavy metals on the environment and human health: Novel therapeutic insights to counter the toxicity. *J. King Saud Univ. - Sci.* **34**, (2022).

31. Hussain, S. *et al.* Health risk assessment of different heavy metals dissolved in drinking water. *Int. J. Environ. Res. Public Health* **16**, (2019).

32. Zamora-Ledezma, C. *et al.* Heavy metal water pollution: A fresh look about hazards, novel and conventional remediation methods. *Environ. Technol. Innov.* **22**, 101504 (2021).

33. Agency, U. S. E. P. & Water, O. 2018 Edition of the Drinking Water Standards and Health Advisories Tables. (2018).

34. Herschy, R. W. Water quality for drinking: WHO guidelines. *Encycl. Earth Sci. Ser.* 876–883 (2012). doi:10.1007/978-1-4020-4410-6_184

35. Parlamento Europeo y el Consejo de la Unión Europea. Directiva (UE) 2020/2184 del Parlamento Europeo y del Consejo de 16 de diciembre de 2020 relativa a la Calidad de las Aguas destinadas al Consumo Humano. *D. Of. la Union Eur.* **2019**, 1–435 (2020).

Chapter 2

Water Remediation

This chapter introduces the topic of water remediation and concisely explores traditional water treatment techniques. An overview of modern water treatment methods is then presented, with a particular emphasis on adsorption techniques. The chapter also covers the issue of adsorption kinetics and isotherms, which is fundamental to designing adsorbents in an actual application.

2.1. Water remediation technologies

Before distribution for human consumption, water has to pass different treatments, normally done in wastewater treatment plants (WWTP). The type of treatment selected will be determined by the nature of the contaminant, which also varies in function of the geographical area. An example of geographical variation in contaminant concentrations can be seen in the contrast between North[1] and South America[2], where high levels of arsenic are prevalent. In contrast,, high arsenic concentrations are not typically observed in eastern Africa. The quality criteria of the raw water input are determined by the regulations[3] established by authorities, which again depend on the place where there are applied (different in each country, region, or continent). Hence, other treatments are used to meet the needs of each site.

2.1.1. Conventional methods

Globally, the most prevalent pollutants in wastewater are microbes, pathogens, and suspended solids, which can be effectively eliminated using conventional treatment techniques up to a certain point, and will be briefly described in this section. See table 1 for a summary of the features of various methods utilized in wastewater treatment.

2.1.1.1. Filtration

One of the fundamental processes in water treatment is filtration. The filtration process involves passing of raw water through a bed of materials in a column to eliminate particulate matter and debris from the water. Filtration acts as a barrier for a wide range of common issues faced by the water supply industry, including color, turbidity, suspended solids and organic and inorganic pollutants[4]. In addition, filtration plays a crucial role in the multi-barrier approach utilized to eliminate pathogens from the water. Various physical characteristics, including grain size, shape, porosity, and the ratio of bed depth to media grain size, establish filtration efficiency[5].

2.1.1.2. Aeration

The aeration process involves the infusion of oxygen into water and the removal of volatile compounds and gases through air stripping[6]. Aeration is a crucial aspect of activated sludge plants as it provides adequate dissolved oxygen for the aerobic organisms involved in biological oxygen demand removal and nitrification. Additionally, aeration helps to keep the biomass in suspension[7].

2.1.1.3. Phase separation

Liquid-solid phase separation is a common technique employed in WWTPs. The most commonly used method is sedimentation, which separates suspended solids by gravity and is probably, the oldest method still in use[8].

2.1.1.4. Chemical processes

Chemical processes are also employed for water treatment. The most common is oxidation, which consists of the transfer of electrons from an oxidized reagent to a reduced chemical species to transform contaminants into innocuous products and biological processes. . The use of oxidizing agents is also effective in removing taste- and odor-causing compounds as well as reducing color in treated water; many oxidants also possess biocidal properties[9].

2.1.1.5. Biological treatments

Biological treatment employs cellular processes executed by bacteria, algae, and another type of microorganisms to decompose organic waste[10]. The goal of this treatment is to establish a system that enables easy collection of the decomposition products for appropriate disposal.

2.1.2. Modern methods

As previously mentioned, WWTPs are designed primarily to reduce organic and suspended solids and are not equipped to remove emerging contaminants effectively [11]. These

contaminants, such as pharmaceuticals, heavy metals, or industrial chemicals, are challenging to extract, transform, or degrade within the current WWTP infrastructure[12]. The removal efficiency of pharmaceuticals in WWTPs can be as low as 10%[13], and their removal has not been a primary objective. However, with the increased use of wastewater in agriculture or livestock, removing pharmaceuticals from the water must now be a primary concern.

It should be noted that even after passing through the WWTP, wastewater still contains several emerging contaminants that are not effectively removed by the treatment process[14]. Several research investigations have reported the presence of pharmaceuticals in freshwater.[15–17]. Since most WWTPs are not designed to remove emerging contaminants, they must be considered a source of pharmaceuticals for the environment[18,19]. In response to emerging contaminants in wastewater, various new treatment methods have been developed over the last two decades to remove these contaminants from water. Modern techniques will be mentioned and briefly explained below, emphasizing the adsorption method.

2.1.2.1. Bio-electrochemical systems

One of the recent advancements in water treatment includes implementing bio-electrochemical systems that can perform water treatment and energy production simultaneously within a reactor[20,21]. Bio-electrochemical systems typically consist of a chamber separated into two parts by an ion exchange membrane. Additionally, these systems can be utilized for organic matter removal[22], desalination[23], or metal recovery[24]. Despite their potential benefits, bio-electrochemical systems have drawbacks, including high production costs[25], limited scalability[26], and low energy output[27].

2.1.2.2. Ultraviolet irradiation

Ultraviolet irradiation technology (UV) is a relatively new treatment method mainly used for disinfection due to the germicidal effect of UV radiation in the range of 250-270 nm[28]. In this case, water flows around a sequence of UV lamps allowing for easy integration into conventional WWTPs. Although mercury lamps have been used as UV radiation sources, ultraviolet light-emitting diodes have become increasingly popular in recent years due to their many advantages over mercury lamps[29].

2.1.2.3. Oxidation processes

Water and wastewater treatment facilities can also utilize advanced oxidation processes through semiconductor photo-catalysis systems[30–32] for effective water treatment. They are effective in treating industrial wastewater that is contaminated with high levels of organic

substances or metals. Nevertheless, the technology is still expensive and not widely adopted in WWTPs.

2.1.2.4. Membrane filtration

Since the 1990s, membrane filtration technology has been utilized for surface water treatment[33,34]. Over the past decade, membrane filtration technology, which is a pressure-driven process with pore sizes ranging from nanometers to microns, has gained widespread use in drinking water production, including the use of reverse osmosis (RO), ultrafiltration (UF), microfiltration (MF), and nanofiltration (NF)[35–37]. Nonetheless, the major drawback of membrane technology is its tendency to become highly fouled, which is the accumulation of materials on the membrane's surface, resulting in a significant decrease in performance[38].

Table 1. Technologies for wastewater treatment, adapted from[39]

Type of treatment	Advantages	Disadvantages	Reference
Biological	Potential for removing metals	Technology is still under development	[40]
Photocatalysis	High degradation rate	Potential to harmful due to exposure to carcinogenic UV light	[41]
Membrane technology	Membrane properties could be adjusted Small occupation area High processing efficiency	Membrane fouling	[42,43]
Ultrasonication	Compact Environmentally friendly	Require high energy	[44,45]
Adsorption	Simple design Cost-effectiveness Excellent approach for removing organic pollutants	Require regeneration of the adsorbent	[46–49]
Coagulation/flocculation	Simple process Good for reclamation or removed pollutants	Require high dosage Produce massive sludge and large particles	[46,50,51]

2.1.3. Adsorption

Adsorption is a cost-effective and promising water purification technology[52] that, despite being an old technique, has found new applications in various contexts[53–55]. The advantageous characteristics of adsorption as a method for wastewater treatment, including procedural simplicity, cost-effectiveness, low energy requirements, and reversibility, make it competent and promising for water remediation[39]. Once the absorbent has been utilized, it is possible to desorb

the pollutants and restore the adsorbent for future use[56]. This makes adsorption a valuable technique for reclaiming chemicals and contributing to a circular economy[57,58]. In addition, adsorbent production usually requires lower-cost materials than other methods, and the technology can be employed effectively without needing electricity[59].

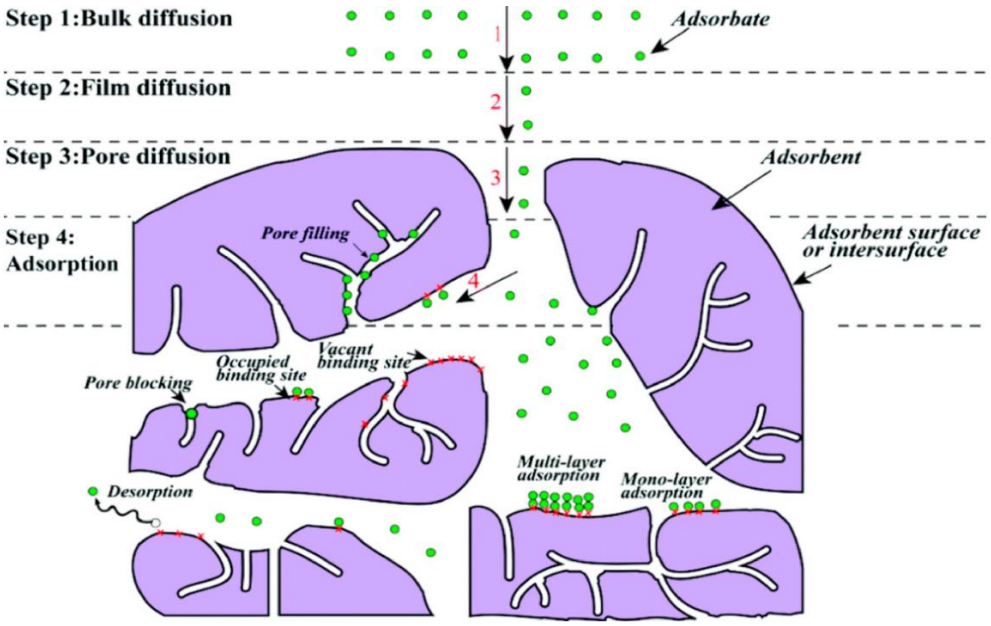

Figure 1. General process of adsorption. Reprinted from reference [60].

Purifying water by adsorption requires a solid phase (adsorbent) and a fluid (water). The adsorbate (one or more dissolved contaminants) is present in the fluid phase. During adsorption, the dissolved contaminants are transferred from the liquid phase to the adsorbent surface resulting in water purification[61]. Adsorption depends on diverse variables such as contact time, pH, temperature, surface-volume ratio, and concentration of pollutants[62,63]

2.1.3.1. Adsorption types and steps

The adsorption process consists of several steps[39]:

1. The transfer of the contaminant (molecule/solute) from the fluid phase to the adsorbate boundary layer.

2. Diffusion from the boundary layer to the external surface of the adsorbent.

3. Transport the material from the external surface to the active sites within the pores.

4. The adsorption of the pollutant onto the solid phase occurs as the final step.

It is possible to distinguish between two different types of adsorption: physical adsorption (physisorption) and chemical adsorption (chemisorption). Regarding physisorption, it is responsible for the attractive forces between molecules and generally occurs with a relatively low

degree of specificity. It is mediated by non-covalent molecular interactions, such as van der Waals forces, hydrophobic effects, π–π interactions, hydrogen bonding, and electrostatic interactions[64]. Conversely, chemisorption involves a chemical bond formation between the adsorbent surface and the adsorbate[65]. This interaction is irreversible and highly specific towards the adsorbent as normally a functional group on the surface of the adsorbents covalently interacts with the adsorbate; these characteristics make chemisorption a monolayered phenomenon. In contrast, physisorption is a reversible and multilayered phenomenon due to the weak molecular interactions involved.

Table 2. Adsorbents used for different pollutants (list restricted to papers from 2010).

Adsorbent Type	Contaminant	Reference
Activated carbon	Dyes, heavy metals	66–68
Graphene oxide	Pharmaceuticals, Organic compounds, metal ions	69,70
Silica-based materials	Inorganic and organic pollutants	71–73
Zeolites	Petroleum, fluoride, nitrate, dyes, heavy metals, cesium	74–76
Biochar	Heavy metals	77–79
GO-biochar	Persulfate, metal ions, dyes, pharmaceuticals	80
Mineral Clays (Montmorillonite, Bentonite, Kaolinite, clinoptilolite, etc.)	Nuclear waste, pharmaceuticals	81,82
Organic polymer resin	Cationic and anionic surfactants, perfluoroalkyl acids	83,84
Poly(saccharide)-based materials	Heavy metals (arsenic)	85,86
Poly(vinyl alcohol) nanofibers + Iron NPs	Arsenic	87,88
Poly(vinyl alcohol) nanofibers + L-cysteine	Arsenic	89
Polybutylene adipate terephthalate (PBAT) nanofibrous	Dyes, pharmaceuticals	90
Biohybrid membrane of polymeric nanofibers and free-living bacteria	Chromium (Cr-VI)	91

2.1.3.2. Adsorption for water treatment

Since the early 1900s, various adsorbent materials, including activated carbon, have been recognized for their potential in water remediation[92]. Table 2 presents selected examples of different types of adsorbents used in wastewater treatment from 2010 to the present. Carbon-

based materials like graphene oxide[69,70], bio-char[77–79], activated carbon[66–68], as well as silica-based materials[71–73], inorganic materials such as zeolites[74–76] and mineral clays[81,82], and organic materials like polysaccharides[85,86], are among the adsorbents used in water remediation.

2.1.3.3. Adsorption experiments and data analysis

Adsorption processes are commonly studied by liquid-solid adsorption experiments. To analyze these experiments, it is usual to measure the adsorbate concentration in the liquid phase before and after the adsorption process, and then use this information to construct adsorption kinetic and isotherm curves.

2.1.3.3.1. Adsorption kinetics and models

The kinetics of the adsorption process can be determined by measuring the amount of pollutant adsorbed by the adsorbent over time while maintaining a constant concentration of the pollutant in the water. By examining the shape of the kinetic curve, it is possible to gain insights into the nature of the adsorption process, as well as the interactions between the adsorbate and the adsorbent; it yields valuable information about the rate of adsorption, the effectiveness of the adsorbent, and the mechanisms governing mass transfer. An understanding of adsorption kinetics is crucial to design effective adsorption systems[93]. The construction of kinetic curves is carried out by plotting the adsorption capacity at a given time (q_t, [mg/g]) versus contact time (between the polluted solution and the adsorbent). Adsorption capacity is calculated as follows

$$q_t = \frac{C_0 - C_t}{d} \quad (1)$$

where C_0 represents the initial concentration [mg/L], C_t is the concentration at a given time [minutes], and *d* is the adsorbent dose [g/L].

Numerous kinetic models have been developed to explain adsorption kinetics, with the pseudo-first-order (PFO) model[94] and the pseudo-second-order (PSO) model[95] being the most extensively utilized.

The PFO model postulates that the adsorption rate is directly proportional to the disparity between the equilibrium concentration and the adsorbate concentration at a particular moment. According to this model, the rate-limiting factor in the adsorption process is the attachment of solute molecules to the adsorption sites on the adsorbent surface. The non linear form of the PFO kinetic equation is expressed as follows

$$q_t = q_e\,(1 - e^{-k_1 t}) \quad (2)$$

where q_t [mg/g] is the adsorption capacity at a given time, k_1 is the characteristic time related PFO constant, and q_e [mg/g] is the adsorption capacity at equilibrium.

The PSO model proposes that the adsorption rate is proportional to the square of the remaining adsorbate concentration at any point in time. This model suggests that the adsorption process is limited by the chemisorption of solute molecules onto the available adsorption sites on the adsorbent surface. This is widely the most employed adsorption kinetic model[96–98]. Expressed below is the non-linear form of the PSO kinetic equation:

$$q_t = \frac{q_e^2 k_2 t}{1 + q_e^{k_2 t}} \quad (3)$$

where q_t [mg/g] is the adsorption capacity at a given time, k_2 is the characteristic time related PSO constant, and q_e [mg/g] is the adsorption capacity at equilibrium.

2.1.3.3.2. Adsorption isotherms and models

The adsorption isotherm illustrates the relationship between the adsorbent's adsorptive capacity (q_e, [mg/g]) and the concentration of the adsorbate at equilibrium (C_e), which is the point when the adsorption process has reached a steady state and is no longer changing over time. This relationship is typically graphed to visualize the extent of adsorption and the efficiency of the adsorbent in removing the adsorbate from the liquid solution. The adsorption capacity at equilibrium is calculated as follows

$$q_e = \frac{C_0 - C_{eq}}{d} \quad (4)$$

where q_e [mg/g] is the adsorption capacity of the adsorbent at equilibrium, C_e [mg/L] is the adsorbate concentration at equilibrium, and c is the adsorbent dosage [g/L]

Adsorption isotherm curves can be analyzed using various isotherm models, each of which has its own assumptions and limitations. Among the commonly employed models are the Langmuir, Freundlich, and .Redlich-Peterson (R-P) isotherm models.

The Langmuir isotherm model is one of the most commonly used isotherm model[99–101]. It was developed by Irvine Langmuir and was initially used to explain gas-liquid adsorption[102,103].The Langmuir isotherm is based on several fundamental assumptions[104], including:

1. Monolayer adsorption, meaning that only a single layer of adsorbate molecules can form on the surface of the adsorbent material.

2. Homogeneous distribution of adsorption sites, implying that all available adsorption sites have the same energy and affinity for the adsorbate molecules.

3. Constant adsorption energy, indicating that the energy required to adsorb a molecule onto the surface is the same for all molecules.

4. Negligible interaction between adsorbate molecules, which assumes that there is no significant interaction between the adsorbate molecules already present on the surface and those being adsorbed.

The model equation is the following

$$q(C_{eq}) = \frac{q_M K_L C_{eq}}{1+K_L C_{eq}} \quad (5)$$

where q is the adsorption capacity [mg/g], C_{eq} is the equilibrium concentration [mg/L], q_M is the maximum adsorption capacity [mg/g], and K_L is constant of Langmuir. The Langmuir isotherm model is used to calculate the maximum adsorption capacity (q_M [mg/g] of an adsorbent.

The Freundlich model[105] is frequently employed to depict nonlinear adsorption phenomena, making it one of the most popular isotherm models in adsorption research[106–108]. The model assumes multilayer adsorption on heterogeneous surfaces. However, the Freundlich model has often been considered an empirical equation lacking physical significance[104]. Despite this, the model is commonly used in published research to represent the adsorption of solutes onto heterogeneous surfaces that involve multilayer adsorption[109]. The freundlich model equation is the following

$$q(C_{eq}) = K_F C_e^{1/n} \quad (6)$$

where q [mg/g] is the adsorption capacity, C_e [mg/L] is the adsorbate concentration in the solution at equilibrium, and K_F [$L^{1/n} mg^{1-1/n} g^{-1}$] and n are constants of the Freunlich model.

The R-P isotherm model[110], which is a combination of the Langmuir and Freundlich models, has been widely utilized in both homogeneous and heterogeneous adsorption processes[111]. The following equation can be used to represent the R-P model

$$q(C_{eq}) = \frac{K_{RP} C_{eq}}{1+a_{RP} C_{eq}^{g}} \quad (7)$$

where q [mg/g] is the adsorption capacity, C_e [mg/L] is the adsorbate concentration in the solution at equilibrium, K_{RP} [L g^{-1}] and a_{RP} [$L^g mg^{-g}$] are constants, and g is the exponent ($0 = g \leq 1$)[104].

2.1.3.3.3. Removal efficiency

The removal efficiency (R%, [%]) is a measure of the effectiveness of the adsorbent material in removing the target pollutant from the liquid solution. This efficiency is generally expressed as a percentage and is determined by employing the following equation

$$R[\%] = \left(\frac{(C_0 - C_{eq})}{C_0}\right) * 100\% \quad (8)$$

where C_0 is the initial concentration of the pollutant in the liquid solution, and C_{eq} is the concentration of the pollutant after it has been adsorbed onto the solid adsorbent material in an equilibrium state.

The removal efficiency explains how well the adsorbent material removes the pollutant from the liquid solution. A higher removal efficiency implies greater efficacy of the adsorbent in adsorbing the target pollutant, whereas a lower removal efficiency indicates reduced effectiveness. The removal efficiency can also be used to compare the performance of different adsorbent materials in removing the same pollutant under similar experimental conditions[112]. These data can be used to enhance the selection and design of adsorbent materials for specific pollutant elimination tasks.

REFERENCES

1. Srivastava, S. *Arsenic in Drinking Water and Food*. *Arsenic in Drinking Water and Food* (2020). doi:10.1007/978-981-13-8587-2

2. Kumar, R. *et al.* Emerging technologies for arsenic removal from drinking water in rural and peri-urban areas: Methods, experience from, and options for Latin America. *Sci. Total Environ.* **694**, (2019).

3. WHO. A global overview of national regulations and standards for drinking-water quality. *Verordnung über die Qual. t von Wasser für den Menschl. Gebrauch (Trinkwasserverordnung -TrinkwV 2001)* 100 (2018).

4. Ahmed, A. K. A. & Marhaba, T. F. Review on river bank filtration as an in situ water treatment process. *Clean Technol. Environ. Policy* **19**, 349–359 (2017).

5. Cescon, A. & Jiang, J. Q. Filtration process and alternative filter media material in water treatment. *Water (Switzerland)* **12**, 1–20 (2020).

6. Martínez-Sabando, J., Coin, F., Melillo, J. H., Goyanes, S. & Cerveny, S. A Review of Pectin-Based Material for Applications in Water Treatment. *Materials* **16**, (2023).

7. Åmand, L., Olsson, G. & Carlsson, B. Aeration control - A review. *Water Sci. Technol.* **67**, 2374–2398 (2013).

8. Goula, A. M., Kostoglou, M., Karapantsios, T. D. & Zouboulis, A. I. A CFD methodology for the design of sedimentation tanks in potable water treatment Case study : The influence of a feed flow control baffle. **140**, 110–121 (2008).

9. Singer, P. C. *et al.* CHAPTER 12 CHEMICAL OXIDATION 1.

10. Pacheco, D., Rocha, A. C., Pereira, L. & Verdelhos, T. Microalgae water bioremediation: Trends and hot topics. *Appl. Sci.* **10**, (2020).

11. Alexa, E. T. *et al.* Occurrence and Removal of Priority Substances and Contaminants of Emerging Concern at the WWTP of. 1–13 (2022).

12. Samal, K., Mahapatra, S. & Ali, H. Pharmaceutical wastewater as Emerging Contaminants (EC): Treatment technologies , impact on environment and human health. *Energy Nexus* **6**, 100076 (2022).

13. Patel, M. *et al.* Pharmaceuticals of emerging concern in aquatic systems: Chemistry, occurrence, effects, and removal methods. *Chem. Rev.* **119**, 3510–3673 (2019).

14. Burns, E. E., Carter, L. J., Kolpin, D. W., Thomas-oates, J. & Boxall, A. B. A. Temporal and spatial variation in pharmaceutical concentrations in an urban river system. *Water Res.* **137**, 72–85 (2018).

15. Williams, M. *et al.* Pharmaceuticals in the environment: An introduction to the ET&C special issue. *Environ. Toxicol. Chem.* **35**, 763–766 (2016).

16. aus der Beek, T. *et al.* Pharmaceuticals in the environment—Global occurrences and perspectives. *Environ. Toxicol. Chem.* **35**, 823–835 (2016).

17. Wilkinson, J. L. *et al.* Pharmaceutical pollution of the world ' s rivers. **119**, 1–10 (2022).

18. Fonseca, E., Hernández, F., Ibáñez, M., Rico, A. & Pitarch, E. Occurrence and ecological risks of pharmaceuticals in a Mediterranean river in Eastern Spain. *Environ. Int.* **144**, 106004 (2020).

19. Lindholm-Lehto, P. C., Ahkola, H. S. J., Knuutinen, J. S. & Herve, S. H. Widespread occurrence and seasonal variation of pharmaceuticals in surface waters and municipal wastewater treatment plants in central Finland. *Environ. Sci. Pollut. Res. Int.* **23**, 7985–7997 (2016).

20. Wang, H. & Ren, Z. J. A comprehensive review of microbial electrochemical systems as a platform technology. *Biotechnol. Adv.* **31**, 1796–1807 (2013).

21. Gude, V. G. Integrating bioelectrochemical systems for sustainable wastewater treatment. **20**, 911–924 (2018).

22. Pant, D., Bogaert, G. Van, Diels, L. & Vanbroekhoven, K. Bioresource Technology A review of the substrates used in microbial fuel cells (MFCs) for sustainable energy production. *Bioresour. Technol.* **101**, 1533–1543 (2010).

23. Kim, Y. & Logan, B. E. Series Assembly of Microbial Desalination Cells Containing Stacked Electrodialysis Cells for Partial or Complete Seawater Desalination. 5840–5845 (2011).

24. Wang, H. & Ren, Z. J. ScienceDirect Bioelectrochemical metal recovery from wastewater : A review. *Water Res.* **66**, 219–232 (2014).

25. Leicester, D., Amezaga, J. & Heidrich, E. Is bioelectrochemical energy production from wastewater a reality ? Identifying and standardising the progress made in scaling up microbial electrolysis cells. *Renew. Sustain. Energy Rev.* **133**, 110279 (2020).

26. Xie, J. *et al.* Bioresource Technology A feasibility investigation of a pilot-scale

bioelectrochemical coupled anaerobic digestion system with centric electrode module for real membrane manufacturing wastewater treatment. *Bioresour. Technol.* **368**, 128371 (2023).

27. Zou, S. & He, Z. Ef fi ciently " pumping out " value-added resources from wastewater by bioelectrochemical systems : A review from energy perspectives. *Water Res.* **131**, 62–73 (2018).

28. Khan, M., Mcdonald, M. & Mundada, K. Efficacy of Ultraviolet Radiations against Coronavirus , Bacteria , Fungi , Fungal Spores and Biofilm. 120–131 (2022).

29. Kheyrandish, A., Taghipour, F. & Mohseni, M. Journal of Photochemistry and Photobiology A : Chemistry UV-LED radiation modeling and its applications in UV dose determination for water treatment. *"Journal Photochem. Photobiol. A Chem.* **352**, 113–121 (2018).

30. Loeb, S. K. *et al.* The Technology Horizon for Photocatalytic Water Treatment: Sunrise or Sunset? (2019). doi:10.1021/acs.est.8b05041

31. Ollis, D. F. & Serpone, N. Photocatalyzed 1 .--. (1991).

32. Hoffmann, M. R., Martin, S. T., Choi, W. & Bahnemann, D. W. Environmental Applications of Semiconductor Photocatalysis. 69–96 (1995). doi:10.1021/cr00033a004

33. Zularisam, A. W., Ismail, A. F. & Salim, R. Behaviours of natural organic matter in membrane filtration for surface water treatment — a review. **194**, 211–231 (2006).

34. Othman, N. H., Alias, N. H., Fuzil, N. S. & Marpani, F. A Review on the Use of Membrane Technology Systems in Developing Countries. (2022).

35. Vingerhoeds, M. H. *et al.* Sensory quality of drinking water produced by reverse osmosis membrane fi ltration followed by remineralisation. *Water Res.* **94**, 42–51 (2016).

36. Fiksdal, L. & Leiknes, T. The effect of coagulation with MF / UF membrane filtration for the removal of virus in drinking water. **279**, 364–371 (2006).

37. Schlichter, B., Mavrov, V. & Chmiel, H. Study of a hybrid process combining ozonation and microfiltration / ultrafiltration for drinking water production from surface water. **168**, 307–317 (2004).

38. Guo, W., Ngo, H. & Li, J. Bioresource Technology A mini-review on membrane fouling. *Bioresour. Technol.* **122**, 27–34 (2012).

39. Sukmana, H., Bellahsen, N., Pantoja, F. & Hodur, C. Adsorption and coagulation in wastewater treatment – Review. **17**, 49–68 (2021).

40. Ahmaruzzaman, M. Role of Fly Ash in the Removal of Organic Pollutants from

Wastewater. *Energy & Fuels* **23**, 1494–1511 (2009).

41. Cheng, Y. W., Khan, M. R., Ng, K. H., Wongsakulphasatch, S. & Cheng, C. K. Harnessing renewable hydrogen-rich syngas from valorization of palm oil mill effluent (POME) using steam reforming technique. *Renew. Energy* **138**, 1114–1126 (2019).

42. Saleh., T. A. & Gupta, V. K. *Nanomaterial and polymer membranes : synthesis, characterization, and applications*. (2016).

43. Zhang, F., Gao, S., Zhu, Y. & Jin, J. Alkaline-induced superhydrophilic/underwater superoleophobic polyacrylonitrile membranes with ultralow oil-adhesion for high-efficient oil/water separation. *J. Memb. Sci.* **513**, 67–73 (2016).

44. Budiman, P. M. & Wu, T. Y. Ultrasonication pre-treatment of combined effluents from palm oil, pulp and paper mills for improving photofermentative biohydrogen production. *Energy Convers. Manag.* **119**, 142–150 (2016).

45. Mahvi, A. H. Application of ultrasonic technology for water and wastewater treatment. *Iran. J. Public Health* **38**, 1–17 (2009).

46. Ariffin, N. *et al.* Review on Adsorption of Heavy Metal in Wastewater by Using Geopolymer. *MATEC Web Conf.* **97**, (2017).

47. Bazrafshan, E., Amirian, P., Mahvi, A. H. & Ansari-Moghaddam, A. Application of adsorption process for phenolic compounds removal from aqueous environments: A systematic review. *Glob. Nest J.* **18**, 146–163 (2016).

48. Cai, L. *et al.* Effective Adsorption of Diesel Oil by Crab-Shell-Derived Biochar Nanomaterials. *Materials* **12**, (2019).

49. Diaz de Tuesta, J. L., Silva, A. M. T., Faria, J. L. & Gomes, H. T. Removal of Sudan IV from a simulated biphasic oily wastewater by using lipophilic carbon adsorbents. *Chem. Eng. J.* **347**, 963–971 (2018).

50. Ang, W. L. & Mohammad, A. W. State of the art and sustainability of natural coagulants in water and wastewater treatment. *J. Clean. Prod.* **262**, 121267 (2020).

51. Chethana, M., Sorokhaibam, L. G., Bhandari, V. M., Raja, S. & Ranade, V. V. Green Approach to Dye Wastewater Treatment Using Biocoagulants. *ACS Sustain. Chem. Eng.* **4**, 2495–2507 (2016).

52. Gisi, S. De, Lofrano, G., Grassi, M. & Notarnicola, M. Characteristics and adsorption capacities of low-cost sorbents for wastewater treatment : A review. *SUSMAT* **9**, 10–40 (2016).

53. Fu, F. & Wang, Q. Removal of heavy metal ions from wastewaters : A review. *J. Environ. Manage.* **92**, 407–418 (2011).

54. Gupta, V. K. Application of low-cost adsorbents for dye removal – A review. *J. Environ. Manage.* **90**, 2313–2342 (2009).

55. Crini, G. Recent developments in polysaccharide-based materials used as adsorbents in wastewater treatment. *Prog. Polym. Sci.* **30**, 38–70 (2005).

56. Suresh, P. *et al.* Understanding and improving the reusability of phosphate adsorbents for wastewater ef fl uent polishing. *Water Res.* **145**, 365–374 (2018).

57. Elhami, V., Antunes, E. C., Temmink, H. & Schuur, B. Recovery Techniques Enabling Circular Chemistry from Wastewater. *Molecules* **27**, (2022).

58. Beatriz, A. *et al.* Cerium recovery from aqueous solutions by bio / adsorption : A review in a circular economy context. *J. Clean. Prod.* **326**, 129395 (2021).

59. Vakili, M. *et al.* Oil Palm Biomass as an Adsorbent for Heavy Metals. **232**,

60. Siong, W. *et al.* A review on conventional and novel materials towards heavy metal adsorption in wastewater treatment application. *J. Clean. Prod.* **296**, 126589 (2021).

61. Dotto, G. L. & Mckay, G. Current scenario and challenges in adsorption for water treatment. *J. Environ. Chem. Eng.* **8**, 103988 (2020).

62. Al-degs, Y. S., El-barghouthi, M. I., El-sheikh, A. H. & Walker, G. M. Effect of solution pH , ionic strength , and temperature on adsorption behavior of reactive dyes on activated carbon. **77**, 16–23 (2008).

63. Teng, G., Yuen, X. & Fen, W. Adsorption of pollutants in wastewater via biosorbents , nanoparticles and magnetic biosorbents : A review. *Environ. Res.* **212**, 113248 (2022).

64. Huang, Y., Li, J. & Wang, X. RSC Advances Applications of conjugated polymer based composites in wastewater puri fi cation. 62160–62178 (2014). doi:10.1039/c4ra11496e

65. Agboola, O. D. & Benson, N. U. Physisorption and Chemisorption Mechanisms In fl uencing Micro (Nano) Plastics-Organic Chemical Contaminants Interactions : A Review. **9**, 1–27 (2021).

66. Streit, A. F. M. *et al.* Science of the Total Environment Development of high quality activated carbon from biological sludge and its application for dyes removal from aqueous solutions. *Sci. Total Environ.* **660**, 277–287 (2019).

67. Azam, K. *et al.* Chemosphere A review on activated carbon modifications for the

treatment of wastewater containing anionic dyes. *Chemosphere* **306**, 135566 (2022).

68. Wang, H., Xu, J., Liu, X. & Sheng, L. Preparation of straw activated carbon and its application in wastewater treatment : A review Fixed carbon. *J. Clean. Prod.* **283**, 124671 (2021).

69. Sophia, A. C., Lima, E. C., Allaudeen, N. & Rajan, S. Application of graphene based materials for adsorption of pharmaceutical traces from water and wastewater- a review. **57**, 19443994 (2016).

70. Perreault, F., Faria, A. F. De & Elimelech, M. Chem Soc Rev Environmental applications of graphene-based nanomaterials. (2015). doi:10.1039/c5cs00021a

71. Diagboya, P. N. E. & Dikio, E. D. Microporous and Mesoporous Materials Silica-based mesoporous materials ; emerging designer adsorbents for aqueous pollutants removal and water treatment. *Microporous Mesoporous Mater.* **266**, 252–267 (2018).

72. Fan, H. *et al.* Removal of cadmium (II) and lead (II) from aqueous solution using sulfur-functionalized silica prepared by hydrothermal-assisted grafting method. *Chem. Eng. J.* **198**–**199**, 355–363 (2012).

73. Sriram, G., Bendre, A., Altalhi, T., Jung, H. & Hegde, G. Chemosphere Surface engineering of silica based materials with Ni – Fe layered double hydroxide for the efficient removal of methyl orange : Isotherms , kinetics , mechanism and high selectivity studies. *Chemosphere* **287**, 131976 (2022).

74. Far, R. M., Bruggen, B. Van Der & Cornelissen, E. A review of zeolite materials used in membranes for water puri fi cation : history , applications , challenges and future trends. (2021). doi:10.1002/jctb.6963

75. Dessalegne, M., Zewge, F. & Díaz, I. Aluminum hydroxide supported on zeolites for fluoride removal from drinking water. *J. Chem. Technol. \& Biotechnol.* **92**, 605–613 (2017).

76. El Hanache, L. *et al.* Performance of surfactant-modified *BEA-type zeolite nanosponges for the removal of nitrate in contaminated water: Effect of the external surface. *J. Hazard. Mater.* **364**, 206–217 (2019).

77. Zeghioud, H., Fryda, L., Djelal, H., Assadi, A. & Kane, A. A comprehensive review of biochar in removal of organic pollutants from wastewater: Characterization, toxicity, activation/functionalization and influencing treatment factors. *J. Water Process Eng.* **47**, 102801 (2022).

78. Tareq, R., Akter, N. & Azam, M. S. Chapter 10 - Biochars and Biochar Composites: Low-Cost Adsorbents for Environmental Remediation. in (eds. Ok, Y. S., Tsang, D. C. W., Bolan, N.

& Novak, J. M. B. T.-B. from B. and W.) 169–209 (Elsevier, 2019). doi:https://doi.org/10.1016/B978-0-12-811729-3.00010-8

79. Tomczyk, A., Kubaczyński, A. & Szewczuk-Karpisz, K. Assessment of agricultural waste biochars for remediation of degraded water-soil environment: Dissolved organic carbon release and immobilization of impurities in one- or two-adsorbate systems. *Waste Manag.* **155**, 87–98 (2023).

80. Fang, Z. *et al.* Conversion of biological solid waste to graphene-containing biochar for water remediation: A critical review. *Chem. Eng. J.* **390**, 124611 (2020).

81. ElBastamy, E. *et al.* Efficiency of Natural Clay Mineral Adsorbent Filtration Systems in Wastewater Treatment for Potential Irrigation Purposes. *Sustainability* **13**, (2021).

82. Thiebault, T. *et al.* Clay minerals for the removal of pharmaceuticals: Initial investigations of their adsorption properties in real wastewater effluents. *Environ. Nanotechnology, Monit. Manag.* **12**, 100266 (2019).

83. Kassar, C., Graham, C. & Boyer, T. H. Removal of perfluoroalkyl acids and common drinking water contaminants by weak-base anion exchange resins: Impacts of solution pH and resin properties. *Water Res. X* **17**, 100159 (2022).

84. Gönder, Z. B., Vergili, I., Kaya, Y. & Barlas, H. Adsorption of cationic and anionic surfactants onto organic polymer resin Lewatit VPOC 1064 MD PH. *Environ. Geochem. Health* **32**, 267–273 (2010).

85. Kwok, K. C. M., Koong, L. F., Al Ansari, T. & McKay, G. Adsorption/desorption of arsenite and arsenate on chitosan and nanochitosan. *Environ. Sci. Pollut. Res. Int.* **25**, 14734–14742 (2018).

86. Nasrollahzadeh, M., Sajjadi, M., Iravani, S. & Varma, R. S. Starch, cellulose, pectin, gum, alginate, chitin and chitosan derived (nano)materials for sustainable water treatment: A review. *Carbohydr. Polym.* **251**, 116986 (2021).

87. Vergara-rubio, A. *et al.* An in situ approach to entrap ultra-small iron oxide nanoparticles inside hydrophilic electrospun nanofibers with high arsenic adsorption. **454**, (2023).

88. Vergara-rubio, A., Rivas-rojas, P., Fern, A. & Larra, A. Journal of Environmental Chemical Engineering Enhancing arsenic adsorption via excellent dispersion of iron oxide nanoparticles inside poly (vinyl alcohol) nanofibers. **9**, (2021).

89. Picón, D., Torasso, N., Roberto, J. & Baudrit, V. Bio-inspired membranes for adsorption of arsenic via immobilized L -Cysteine in highly hydrophilic electrospun nanofibers. *Chem. Eng.*

Res. Des. **185**, 108–118 (2022).

90. Picón, D., Vergara-Rubio, A., Estevez-Areco, S., Cerveny, S. & Goyanes, S. Adsorption of Methylene Blue and Tetracycline by Zeolites Immobilized on a PBAT Electrospun Membrane. *Molecules* **28**, (2023).

91. Pereira, P. P. *et al.* Biohybrid membranes for effective bacterial vehiculation and simultaneous removal of hexavalent chromium (CrVI) and phenol. *Appl. Microbiol. Biotechnol.* **105**, 827–838 (2021).

92. Çeçen, F. Water and Wastewater Treatment : Historical Perspective of Activated Carbon Adsorption and its Integration with Biological Processes. 1–12 (2011).

93. Wang, J. & Guo, X. Adsorption kinetic models: Physical meanings, applications, and solving methods. *J. Hazard. Mater.* **390**, (2020).

94. Lagergren, S. About the Theory of So-Called Adsorption of Soluble Substances. in

95. Ho, Y. S. & McKay, G. Pseudo-second order model for sorption processes. *Process Biochem.* **34**, 451–465 (1999).

96. Zhuang, S., Cheng, R. & Wang, J. Adsorption of diclofenac from aqueous solution using UiO-66-type metal-organic frameworks. *Chem. Eng. J.* **359**, 354–362 (2019).

97. Gogoi, S., Chakraborty, S. & Dutta Saikia, M. Surface modified pineapple crown leaf for adsorption of Cr(VI) and Cr(III) ions from aqueous solution. *J. Environ. Chem. Eng.* **6**, 2492–2501 (2018).

98. Gao, P. *et al.* Enhanced adsorption of steroid estrogens by one-pot synthesized phenyl-modified mesoporous silica: Dependence on phenyl-organosilane precursors and pH condition. *Chemosphere* **234**, 438–449 (2019).

99. Souza, W. D. M., Rodrigues, W. S., Lima Filho, M. M. S., Alves, J. J. F. & Oliveira, T. M. B. F. Heavy metals uptake on Malpighia emarginata D.C. seed fiber microparticles: Physicochemical characterization, modeling and application in landfill leachate. *Waste Manag.* **78**, 356–365 (2018).

100. Costa, J. A. S. *et al.* Applications of inorganic–organic mesoporous materials constructed by self-assembly processes for removal of benzo[k]fluoranthene and benzo[b]fluoranthene. *J. Sol-Gel Sci. Technol.* **75**, 495–507 (2015).

101. Saeidi, N., Kopinke, F.-D. & Georgi, A. Understanding the effect of carbon surface chemistry on adsorption of perfluorinated alkyl substances. *Chem. Eng. J.* **381**, 122689 (2020).

102. Langmuir, I. THE CONSTITUTION AND FUNDAMENTAL PROPERTIES OF SOLIDS AND LIQUIDS. PART I. SOLIDS. *J. Am. Chem. Soc.* **38**, 2221–2295 (1916).

103. Langmuir, I. THE ADSORPTION OF GASES ON PLANE SURFACES OF GLASS, MICA AND PLATINUM. *J. Am. Chem. Soc.* **40**, 1361–1403 (1918).

104. Wang, J. & Guo, X. Adsorption isotherm models: Classification, physical meaning, application and solving method. *Chemosphere* **258**, 127279 (2020).

105. Freundlich, H. Über die adsorption in lösungen. *Zeitschrift für Phys. Chemie* **57**, 385–470 (1907).

106. Maged, A., Iqbal, J., Kharbish, S., Ismael, I. S. & Bhatnagar, A. Tuning tetracycline removal from aqueous solution onto activated 2:1 layered clay mineral: Characterization, sorption and mechanistic studies. *J. Hazard. Mater.* **384**, 121320 (2020).

107. Xue, Y. *et al.* Mechanistic insights into selective adsorption and separation of multi-component anionic dyes using magnetic zeolite imidazolate framework-67 composites. *J. Mol. Liq.* **296**, 111990 (2019).

108. Chakraborty, P., Banerjee, S., Kumar, S., Sadhukhan, S. & Halder, G. Elucidation of ibuprofen uptake capability of raw and steam activated biochar of Aegle marmelos shell: Isotherm, kinetics, thermodynamics and cost estimation. *Process Saf. Environ. Prot.* **118**, 10–23 (2018).

109. Wang, C. *et al.* Comparison of Langmuir and Freundlich adsorption equations within the SWAT-K model for assessing potassium environmental losses at basin scale. *Agric. Water Manag.* **180**, 205–211 (2017).

110. Redlich, O. & Peterson, D. L. A useful adsorption isotherm. *J. Phys. Chem.* **63**, 1024 (1959).

111. Hossain, M. A., Ngo, H. H., Guo, W. S. & Nguyen, T. V. Palm oil fruit shells as biosorbent for copper removal from water and wastewater: Experiments and sorption models. *Bioresour. Technol.* **113**, 97–101 (2012).

112. Elkhaleefa, A. *et al.* Evaluation of the Adsorption Efficiency on the Removal of Lead(II) Ions from Aqueous Solutions Using Azadirachta indica Leaves as an Adsorbent. *Processes* **9**, (2021).

Chapter 3

Pectin

In this chapter, we introduce the structure and properties of pectin, the material we have used to prepare adsorbents. We will define pectin, extraction sources, and its chemical structure. After that, we focus on the problem of insolubilization of pectin, which is done by crosslinking with different agents. The more used crosslinker in the literature is calcium, which produces a particular structure on the pectin chains (egg-box model). Finally, we discuss the pectin applications, particularly emphasizing in their use for the remediation of heavy metals.

3.1. Pectin

Pectin, an essential constituent of the cell wall in higher plants, is a heteropolymer primarily comprised of α-1-4 D-galacturonic acid units, which may exhibit methyl esterification or remain unmodified[1]. Pectin is mostly found in the middle lamella of the cell wall of fruits or other vegetables. However, it is also present in smaller amounts in the primary and secondary walls, where it is usually associated with other components such as celluloses, hemicelluloses, or lignins[2]. These polysaccharides (pectins) are very important in plant growth and development due to their contribution to the rigidity and integrity of plant tissues[3]. Pectins play a vital role in facilitating ionic transport, determining the porosity of cell walls, and exerting influence over the activation of the plant's immune system[4]. In addition, they play an important role in the ripening, storage, and processing of raw plant material for food[5].

3.2. Pectin chemical structure

Pectin backbone is mainly composed of α-(1,4)- linked-D-galacturonic acid (GalA) residues. Different domains can be distinguished within the pectic molecules (see Figure 1):

homogalacturonan (HG), rhamnogalacturonan I (RGI), rhamnogalacturonan II (RGII), xylogalacturonan (XGA), apiogalacturonan (AGA), arabinan, galactan, arabinogalactan I (AGI) and arabinogalactan II (AGII)[6].

3.2.1. Homogalaturonan (HG)

The most abundant domain in the pectin macromolecule is homogalacturonan, which makes up 60% of the full macromolecule. The HG domain is formed by a linear chain composed of α-1,4-D-galacturonic acid residues, where the carbon 6 (C-6) of the D-galacturonic acid residues exhibit the potential for methyl esterification ($COOCH_3$) or carboxylation (COO^-, when deprotonated) (see Figure 2). Additionally, acetylation at the oxygen 2 (O-2) and/or O-3 position of the GalA residues is less frequently observed[3].

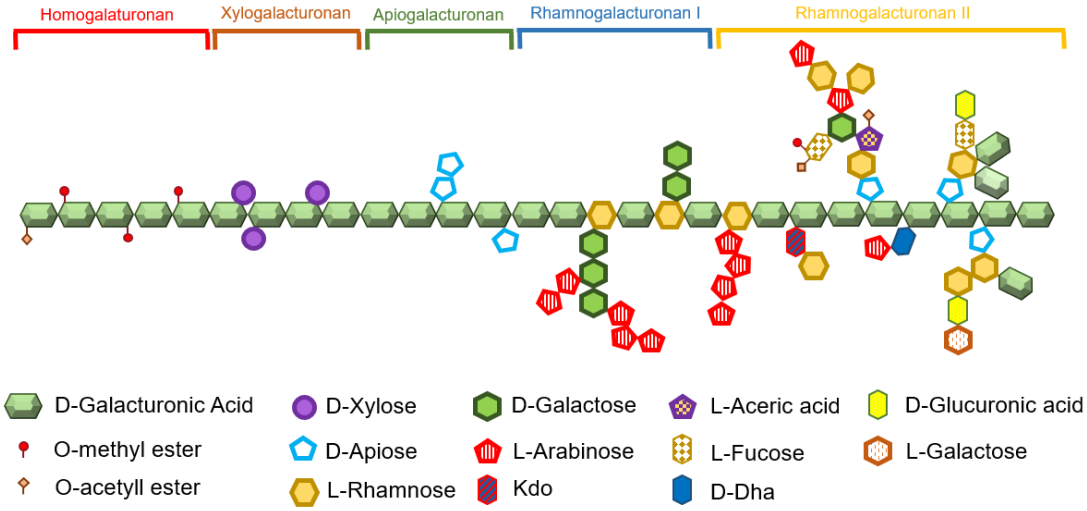

Figure 1. Representation of the chemical structure of pectin, the main molecule domains (HG, RG I, RG II, XGA and AGA) and the different monosaccharides that compose them.

3.2.1.1. Pectin Degree of Methyl Esterification (D.M.)

The degree of esterification (D.M.) of pectin is the ratio of methyl esterified GalA residues to the total amount of GalA residues. This D.M. is expressed as a % and theoretically it can range from 0-100%[7]. Pectins are classified into two types according to their D.M.: high methoxyl (HM) and low methoxyl (LM) pectins. HM pectins are those that have the methyl ester group on more than half of the GalA residues. LM pectins, on the other hand, are those that present less than half of the methylesterified GalA residues. The D.E. plays a crucial role in the gelling properties and mechanism[8], as discussed later.

3.2.2. Rhamnogalacturonan I (RGI)

The rhamnogalacturonan domain I is formed by repeating residues of α-1,4-D-galacturonic acid and α-1,2-L-rhamnose (see Figure 1). The galacturonic acid residues may be acetylated and both residues may contain side chains of neutral sugars such as galactose, arabinose, and xylose[9]. The proportion of branched rhamnose units varies from 20% to 80% and depends on the origin of the pectin[10]. HG is assumed to be covalently bound to RGI[3]. Thus, these polysaccharides cannot be cleaved without chain cleavage using, for example, enzymes such as endopolygalacturonase[11].

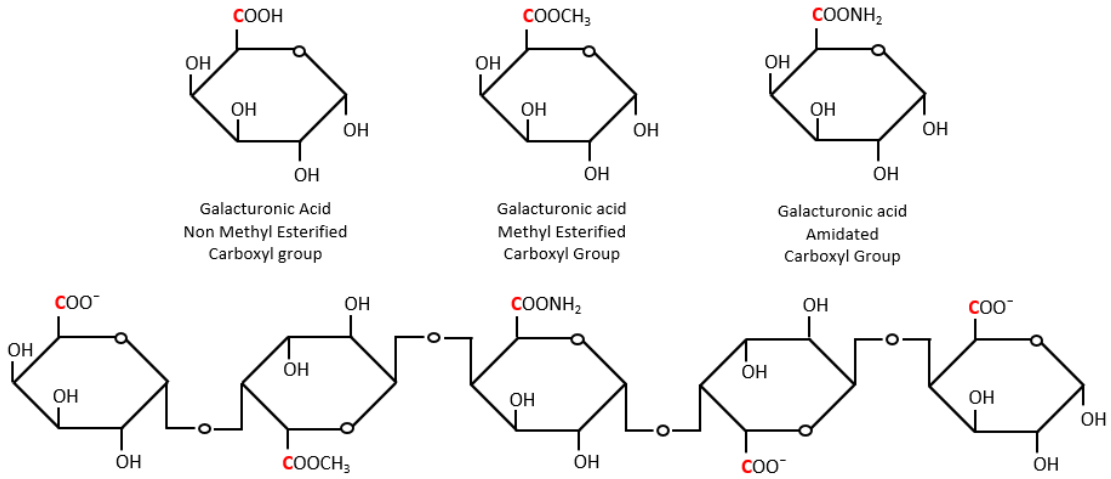

Figure 2. Schematic representation of the poly(galacturonic) acid chain. Carbon 6 of the GalA residues is marked in red, and the different functional groups that can be exhibited are depicted.

3.2.3. Rhamnogalacturonan II (RGII)

Ramnogalacturonan II (see Figure 1) is composed of a backbone consisting of 7-9 branched galacturonic acid residues with four side chains at C-2 and C-3, which can be arabinose, apiose, fructose, galactose, ramose, aceric acid, acetone,, glucuronic acid, galacturonic acid, 2-O-methyl-xylose, 2-O-methyl-fucose, 3-deoxy-lixo-2-herptulosaric acid (DHA), and 3-deoxy-manno-2-octusolonic acid (KDO)[12]. The side chains of RGII are composed of 12 different types of sugars with more than 20 different types of linkages, making it the most complex pectin domain in terms of structure. Crosslinking between RGII chains of two adjacent pectin molecules increases the integrity of pectin[1].

3.2.4. Other pectin domains

Xylogalacturonan (XGA) is a polymer containing an HG backbone with O-3-linked xylose residues on some galacturonic acid units[3]. In the apiogalacturonan (AGA) domain, one or two interconnected apiosyl residues are linked to galacturonic acid units[13].

Arabinans are chains consisting of α-1,5-L-arabinofuranosyl units with α-arabinofuranosyl residues linked at C-2 and/or C-3 in the arabinose molecule[14]. The arabinans in the primary cell wall are mostly RGI side chains[15].

Arabinogalactan domain I is composed of a backbone of β-1,4-D-galactopyranosyl residues attached to short chains of α-1,5-arabinose residues at C-3 of the galactose molecule[16]. Arabinogalactan II also contains β-1,4-D-galactopyranosyl chains, but the linkages occur at the C-1, C-3, and C-6 carbons on the galactose molecule[17]. This type of arabinogalactan is highly branched[10].

3.3. Pectin sources

Pectin is present in most of the higher plant tissues, thus, is always extracted from vegetal material[18]. The most common sources for commercial pectin extraction are by-products generated by the industry, and among these, the most widely used ones are apple pomace and citrus peels.

Reported maximum extraction yields of pectin from apple pomace are between 16.65 - 18.79 % depending on the apple variety[19]. Citrus fruits, specifically their peels, exhibit a notable richness in pectin, with concentrations ranging from 25% to 30% of their dry weight[20].

Citrus peels have become the leading commercially available pectin source due to the large amount of this waste generated by the juice industry and the high yields obtained by extraction. The available literature offers a detailed account of the pectin composition in various citrus fruit varieties such as lime, lemon, orange, and grapefruit[21]. Yields of extraction of pectin from lime peels up to 25.6 % have been achieved by high hydrostatic pressure treatment[22].

Sugar beet pulp has emerged as an additional viable source for commercial pectin production. Its remarkable pectin content, ranging from 15% to 30% on a dry weight basis, coupled with its abundant availability stemming from extensive production within the sugar industry, positions it favorably[23]. The yield of pectin derived from sugar beet pulp varies between 6.3% and 23.0%, depending on the specific extraction method employed[24].

Another source, due to the high amount of by-products generated by the industry, is tomato pomace produced by the canning industry, which contains approximately 7.55% pectin content on a dry basis[25]. Carrot pomace, a by-product of carrot processing, is also significant. It boasts a high dietary fiber content of 29.6%, with pectin comprising 22-25% of the total nutritional fiber[26]. Watermelon rinds, typically discarded, exhibit a pectin content ranging from 19% to 21% (w/w)[27]. Lastly, banana peels, accounting for approximately 30% of the total banana weight on average, are often discarded but can yield about 9% pectin (w/w) [28].

The essential characteristics of pectin, including galacturonic acid content, degree of esterification, molecular weight, and neutral monosaccharide content, exhibit a strong dependence on various factors, namely the source from which pectin is extracted, as well as the specific batch and ripening stage of said source[18].

3.4. Pectin isolation

Pectin isolation usually comprises three stages: Extraction, purification and fractionation.

3.4.1. Pectin extraction

The process of pectin extraction can be described as a physical-chemical procedure that involves a series of stages, including hydrolysis and extraction of pectin macromolecules from plant tissue, followed by their solubilization into the surrounding solvent. These stages occur continuously, influenced by various process parameters, with temperature, pH, and time being the primary factors at play[30].

Pectin, being a complex macromolecule, possesses an intricate structure that requires meticulous attention to preserve its integrity. This preservation is crucial as it directly impacts essential properties such as molecular weight, water solubility, and gelation capabilities. The choice of extraction and isolation method employed for pectin from plant material assumes great

Figure 3. Cartoon depiction representing the evolution of Ca2+ cross-linking of LM pectin and its final structure[29].

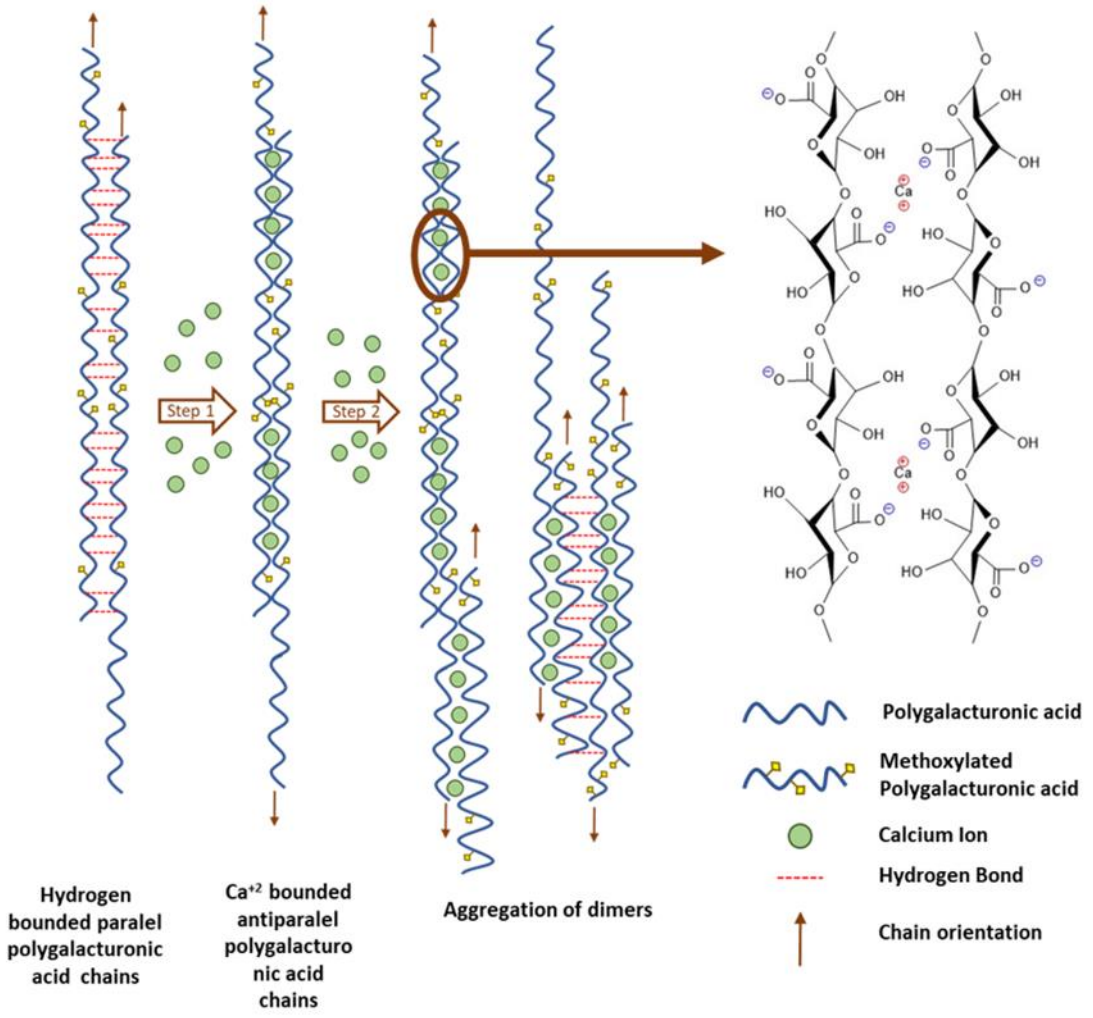

significance in maintaining these fundamental attributes. Diverse approaches are available for extracting pectin from cell walls, utilizing various techniques, including chemical, physical, and enzymatic treatments[31].

3.4.2. Pectin purification and fractionation

Several techniques are utilized to achieve a refined pectin product after extraction, including ionic exchange, nitration, dialysis, precipitation, and combinations thereof. These purification procedures also impact the quantity of pectin, as well as the macromolecular characteristics and DE achieved[32].

In cases where the research objective involves a comprehensive exploration of the extracted pectin's composition, purification is commonly coupled with fractionation, which can be accomplished using an array of techniques[18]. Among these techniques are: Anion exchange chromatography[33], gel permeation chromatography[34], membrane separation[35], ultrafiltration[17], and enzymatic fractionation[36].

3.5. Pectin crosslink

Pectin is a water-soluble material that can be transformed into an insoluble form through cross-linking. The DE is directly related to the gelling mechanisms of pectin. As a result, HM pectin and LM pectin follow different cross-linking mechanisms.

3.5.1. HM pectin cross-link mechanism

The sensitivity of HM pectin to acidity is notable, as it readily undergoes gelation in acidic environments, usually at a pH below 3.5. Furthermore, a higher sugar concentration (around 65%, w/w) is required to achieve optimal gel formation in HM pectin[37]. Moreover, the gelation mechanism of HM pectin entails the creation of junction zones, which arise from the interaction of polymer chains[38] and are fortified through hydrogen bonds and hydrophobic interactions[39]. These forces belong to noncovalent interactions so the gel is physically cross-linked and often has some application shortcomings including low strength, toughness, and relatively weak stability. These forces are classified as noncovalent interactions, resulting in a physically cross-linked gel[40]. However, such gels often exhibit certain limitations regarding strength, toughness, and stability[41].

3.5.2. LM pectin cross-link mechanism

LM pectin, unlike HM pectin, undergoes cross-linking in the presence of divalent metals like Ca^{2+} [42]. Historically, the development of Ca^{2+}–pectin gels has been attributed to the "egg-box" model[43,44], initially proposed for alginates[45]. The binding mechanism of pectin involves the cooperative interaction of two or more chains, resulting in the creation of junction zones instead of individual cross-links. Forming a stable junction zone requires a minimum length of consecutive non-methyl esterified units, typically ranging from 6[46] to 20[47]. According to the "egg box" model, the process can be divided into two stages: first, the dimerization occurs, followed by the subsequent aggregation of these pre-formed dimers (see figure). Based on a molecular modeling simulation study, a modified model known as the "shifted egg-box" model was proposed to describe pectin–calcium gels[47]. Unlike alginate, pectin–calcium gels exhibit a slight shift in the dimer conformation, where one chain is displaced relative to the other. This modified model offers a more accurate representation of these systems. Recent research has also revealed that, in certain cases, calcium ions can interact with individual dissociated carboxyl groups, forming mono-complexes through charge reversal on a single chain. This interaction leads to unspecific or random cross-linking between the pectin chains, in addition to or instead of dimerization.

Table 1. Parameters (intrinsic to pectin and extrinsic) that influence the gel formation

Intrinsic Parameters	
Methoxylation degree (DM)	As the degree of methoxylation (DM) decreases, the number of non-methoxylated GalA residues with sufficient length for the formation of the egg-box structure increases, leading to a significant augmentation in the calcium ion binding capacity.
Pattern of methoxylation	At higher degrees of methoxylation (DM), pectin containing a block-wise distribution of non-methoxylated carboxyl groups has the ability to associate with egg-box formation. Egg-box structure are not formed when pectin has a random distribution of carboxyl groups
Chain length	A decrease in the molecular mass of pectin correlates with a reduction in the strength of the gel..
Branching	Steric hindrance, possibly induced by large side chains, can impede the interactions between pectin molecules.
Amidation	The presence of amidation in pectin facilitates the formation of stronger gels, particularly under low pH conditions, due to the formation of hydrogen bonds between amide groups.
Acetylation	The presence of acetyl groups significantly diminishes the binding strength of pectin with calcium ions.
Extrinsic Parameters (Environment)	
Calcium content	The impact of calcium ion concentration on LM pectin gelation is primarily explained in relation to a stoichiometric ratio: $R = 2[Ca^{2+}]/[COO^{-}]$. R = 0.5, theoretically, all calcium ions are bound, forming the “egg-box” structure.
Pectin content	When the value of R remains constant, the gel strength demonstrates an increase as the concentration of the polymer rises.
pH	In order for ionic cross-links to be established between the carboxyl groups of pectin and calcium ions, pectin must be in a charged state, meaning the carboxyl groups need to dissociate. While the gel properties of a pectin-calcium gel remain relatively unaffected by pH levels above 4.5, a decrease in pH below 4.5 leads to a reduction in the charge density of pectin and subsequently decreases its attraction to calcium ions. However, this impact is partially counterbalanced by the formation of hydrogen bonds between protonated carboxyl groups.
Temperature	Elevated temperatures facilitate chain scission, resulting in the formation of dimers. However, upon cooling, these junction zones are stabilized through hydrogen bonding, which coincides with the cooperative immobilization of calcium.

X-ray diffraction studies and dynamic mechanical measurements[48] were used to study the reorganization of pectin and alginate crosslinked by Ca^{2+}. These studies evidenced that the "fringe-micellar" structure describes the amorphization of pectin due to the binding of Ca^{2+}. This suggests that the reorganization of molecular network structure led to the destruction of specific certain pectin crystalline tie points. Various factors, both "intrinsic" and "extrinsic," such as methyl ester amount and distribution, chain length, pectin concentration, amidation and acetylation degrees, molecular weight, calcium content, temperature, and pH, exert an influence on the formation of the final pectin gel[49]. The influence of these parameters on the ultimate characteristics of the gel is elucidated in Table 1.

3.5.3. LM pectin cross-linking agents

The most common and widely used method to crosslink pectin is the utilization of cations (ionic crosslinking), due to advantages such as the possibility of releasing the adsorbed pollutant (sometimes very valuable) and recovering the adsorbent for subsequent uses. Besides ionic crosslinking, non-ionic crosslink also can be performed with compounds such as glutaraldehyde[50] or laccase[51].

Among ionic crosslinking used to crosslink LM pectin, we can differentiate into monovalent (Na^+, K^+, Li^+)[52–56], divalent (Ca^{2+}, Cu^{2+}, Sr^{2+}, Ni^{2+}, Zn^{2+}, Cd^{2+}, Pb^{2+} or Mg^{2+})[33,34,57–64] or trivalent (Al^{3+}, La^{3+}, and Fe^{3+})[65–68] being most used.

The classic "egg-box" structure is a well-known model used to describe pectin crosslinked by divalent cations, commonly studied using Ca^{2+}. However, when a divalent cation other than Ca^{2+} is used, there may be slight variations in the resulting structure. Crosslinking LM pectin with Ca^{2+} primarily involves the interaction of cations with carboxyl groups, leading to the formation of uniform pectin network fibers known as "egg-box" dimers. On the other hand, when Zn^{2+} is used, it interacts with both carboxyl and hydroxyl groups, resulting in a less homogeneous crosslinked pectin network[69].

Interactions between pectin and divalent cations can be monodentate (interaction of a single carboxyl group from pectin and a cation) or bidentate (two carboxyl groups from independent galacturonic acid chains and a cation). The interaction between divalent cations and poly(galacturonic) acid is monodentate for Mg^{2+} and Zn^{2+}, while it is bidentate for Ba^{2+} and Ca^{2+}. The binding mechanism of Zn^{2+}, Ca^{2+}, and Ba^{2+} divalent cations is associated with mono-complexation and the formation of point-like cross-links or dimers, depending on the molar ratio (R) between the cation and galacturonic acid. This conclusion is drawn based on the coordination of water molecules with the different cations. In the case of Zn^{2+}, Ca^{2+}, and Ba^{2+}, the coordination with water was comparatively weaker than that of Mg^{2+}. During the cross-linking process, Zn^{2+} loses one water molecule, while Ca^{2+} and Ba^{2+} lose two water molecules each. In contrast, Mg^{2+}

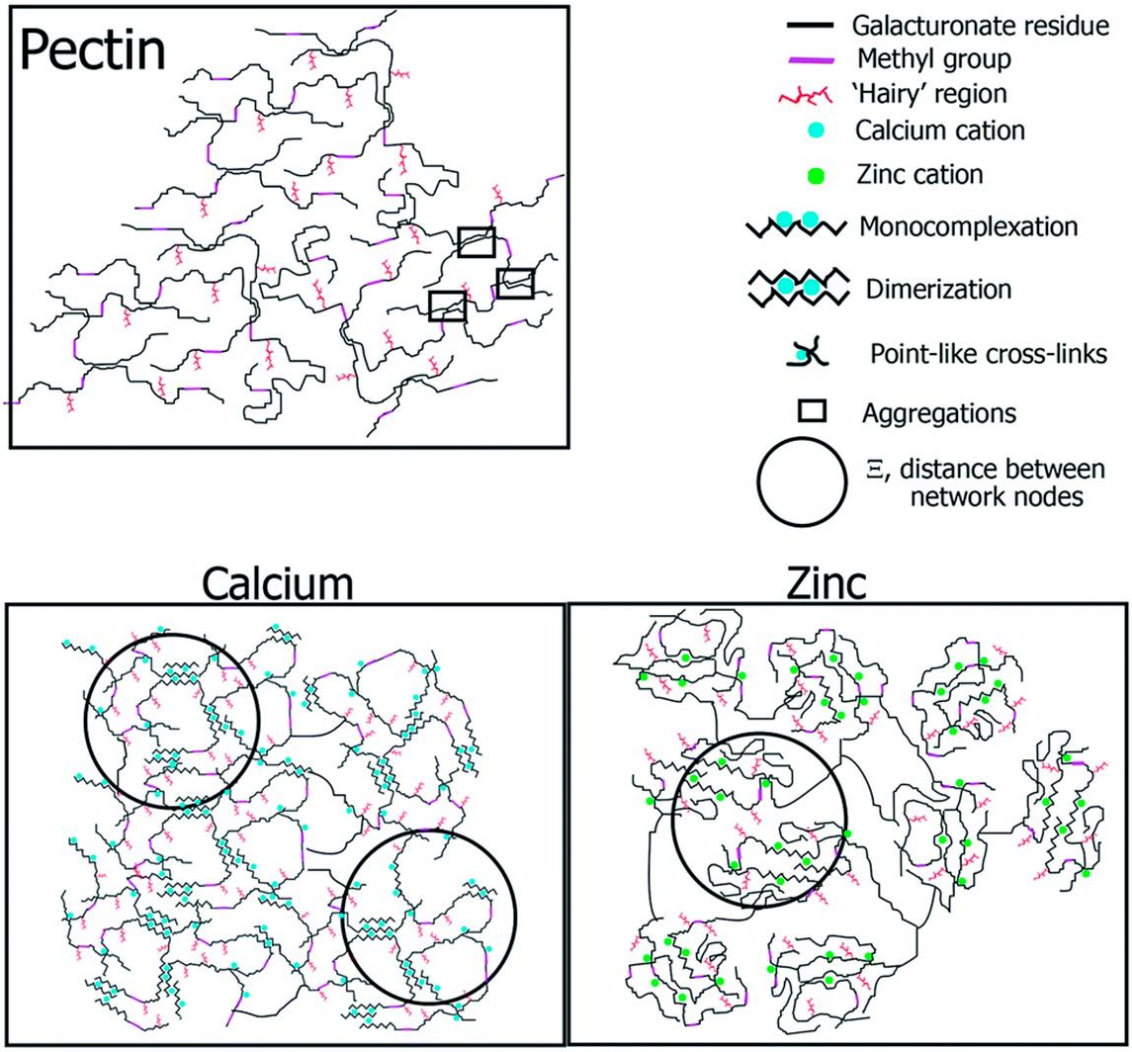

Figure 4. Proposed network arrangement for calcium and zinc pectate complexes at two different molar ratios, namely R = 0 (pectin alone) and R = 0.4. Figure extracted from[71].

exhibits strong interaction with water and remains weakly bound to poly(galacturonic) acid by sharing water molecules from its coordination shell with the carboxylate groups[70].

3.6. Pectin applications

The potential applications of pectin span various industries, particularly in the realms of health, pharmacy, food, and packaging. Being a natural component found in vegetables and fruits, pectin serves as an incredibly safe and versatile food additive (E440), employed as a texturizer or gelling agent in food applications. Moreover, pectin's widespread use extends to diverse scientific fields, thanks to its abundance, safety, cost-effectiveness, and functional properties. With unique structural characteristics conferred by its functional groups and the possibility of chemical modification, pectin emerges as an excellent candidate for numerous purposes, including food innovations[72], nutritional enhancement[73], drug delivery systems[41], disease treatment[74], tissue

engineering[75], and other innovative approaches[76]. Significantly, pectin exhibits resistance to hydrolyzing enzymes in the gastrointestinal tract and withstands acidic or alkaline environments. This characteristic makes it particularly suitable for applications involving targeted delivery to the colon through oral administration under specific conditions.

Specifically, low-esterification pectin possesses significant value as a functional food ingredient[77], offering extensive potential for diverse applications. Moreover, it has garnered attention as a promising biomaterial for biomedical and tissue engineering purposes[78]. While pectin films have found utility in packaging, their mechanical properties and high hydrophilicity present certain limitations[79,80]. However, these challenges can be addressed by incorporating other polymers[81], cross-linkers, and/or filler materials to enhance the film's performance and overcome these drawbacks[82].

3.6.1. LM Pectin in water treatment

Numerous studies have concentrated on the utilization of pectin as an adsorbent for the remediation of heavy metals from water. An overview of the maximum binding capacities for various divalent metals onto pectin with an LM degree (<50) is presented in Table 4.

In the study conducted by Cataldo et al.[83], pectate and poly(galacturonate) calcium gel beads were prepared for mercury (II) removal. Their investigation of different pH values, they determined that the optimal pH range for effective Hg^{2+} removal fell between 3 and 3.6. Another research effort by Celus et al.[84] explored the adsorption capacity of citrus pectin for Fe^{2+}. It highlighted two structural properties: the degree of methyl esterification (DM) and the degree of blockiness (the ratio of non-methyl esterified GalA units organized in blocks to the total amount of GalA units). The results indicated that both DM and DBabs influenced the interactions between pectin and Fe^{2+}, with a higher DBabs or lower DM resulting in an increased binding capacity for Fe^{2+}.

As part of an independent study, pectin micro-gel particles were utilized to eliminate methylene blue (MB)[85]. The researchers observed remarkably high absorption ratios (as shown in Table 4), even within time frames shorter than 20 minutes. Furthermore, LM pectin was utilized to remediate mineral soils contaminated with Cu^{2+}[86]. More recently, a sweet potato residue, subjected to modification through high hydrostatic pressure (HHP)-assisted pectinase treatment, was prepared[87]. This modified sweet potato pectin was subsequently utilized for the removal of Pb^{2+}. The study demonstrated that the modified sweet potato pectin exhibited superior adsorption performance for both Pb^{2+} and Cu^{2+} compared to natural pectin.

LM Pectin was also combined with other biopolymers, such as chitosan, to produce chitosan-pectin gel beads through an environmentally friendly approach [88]. These gel beads were

designed to remove numerous heavy metals, including Cu^{2+}, Cd^{2+}, Hg^{2+}, and Pb^{2+}. The study investigated various parameters such as pH, contact time, heavy metal concentration, temperature, and adsorption mechanism. It was discovered that adding pectin enhanced the adsorption capacities, porosity, and stability of the adsorbents. Infrared analysis of the adsorbents revealed that the interaction between the heavy metals and chitosan-pectin gel beads occurred through complexation with functional groups like carboxyl, hydroxyl, amine, and amide.

Another research conducted by Mata et al.[89] involved the creation of sugar-beet pectin xerogels utilizing sugar industry residues. Their investigation focused on continuous biosorption conditions rather than stationary ones. The adsorbent was employed for metal recovery from effluents in continuous systems. Different experimental conditions were examined, including feed flow rate and bed height (amount of biosorbent). The optimal conditions for Cu^{2+} sorption in column reactors were 3 g of biomass, 25 mg/L metal concentration, 2 mL/min feed flow rate, and a reverse feeding system.

It is important to highlight a significant variation in the results reported in the literature regarding the adsorption capacity of pectin-based adsorbents. This variation can be attributed to the diverse chemical characteristics of pectin, which are influenced by factors such as the source from which pectin is derived and the extraction method employed. Hence, the adsorption capacity of pectin is highly dependent on these factors, leading to a notable dispersion of results across different studies.

For example, an early study conducted by Kartel et al.[90] demonstrated that apple pectin exhibited the highest affinity for Co^{2+} ions, while beet pectin displayed better affinity for Cu^{2+} and Cd^{2+} ions. In contrast, citrus pectin showed a distinct preference for Ni^{2+}, Zn^{2+}, and Pb^{2+} ions. These variations in affinity can be attributed to the structural disparities among different types of pectin. For instance, the galacturonic acid content in apple pomace ranges from 20% to 44%[91], whereas in orange peel, it is between 66% and 70% on a dried basis. Moreover, apple pectin obtained through various extraction methods exhibited high degrees of methylation, ranging from 54.5% to 79.5%[92], whereas the degree of methoxylation was considerably lower in orange peels. Consequently, the source of pectin and the extraction process employed determine the structural properties of pectin, which, in turn, dictate the adsorption capacity of heavy metals.

The methoxylation degree (DM) of pectin stands out as a significant structural property influencing the binding of heavy metals[3,93]. A lower DM value results in higher availability of carboxyl groups on pectin, facilitating stronger interactions with metal ions and increasing adsorption capacity. Furthermore, studies have highlighted the importance of the pattern of methyl esterification in determining the adsorption capacities of pectin[94].

The impact of DM on the adsorption of metal ions has been investigated in several studies, including Zn^{2+} [95], Fe^{3+} [84], and Ca^{2+}, Zn^{2+}, Fe^{2+}, and Mg^{2+} [96]. However, the influence of other structural parameters of pectin, such as the degree of acetylation (DA), chain length, or the presence of branched domains (e.g., RG I, RG II, etc., as depicted in Figure 1), has received comparatively less attention about the adsorption capacity.

The adsorption capacity of pectin is also influenced by its molecular weight. It has been observed that a lower molecular weight corresponds to a higher adsorption capacity[97]. This phenomenon can be attributed to smaller pectin chains that expose additional active sites, enabling a stronger electrostatic attraction and enhancing the capture of heavy metal ions[98]. Furthermore, longer pectin chains tend to form more robust gels that restrict the penetration of metal ions.

Furthermore, the considerable heterogeneity in terms of chemical composition and physicochemical properties of pectin, including variations in molecular weight, degree of esterification, dispersion, and galacturonic acid content, makes it challenging to predict the metal-binding capacity of different pectin batches accurately.

Table 2. Pectin composites used for water remediation.

Origin	Adsorbent	CA	DM [%]	Pollutant	q_{max} [mg/g]	Ref.
Citrus fruit	Pectin	Ca^{2+}	<50	Hg^{2+}	1.7 mmol/g	83
Commercial pectin	Demethylated pectin	Ca^{2+}/Mg^{2+}	13	Fe^{2+}	0.523 mol Fe^{2+}/mol GalA	84
Commercial pectin	Pectin microgel particles	Ca^{2+}	16.4	MB **	284 mg/g	85
Citrus peel	Pectin with Oxisol Pectin with Utisol	Nr.	6.7	Cu^{2+} Cu^{2+}	33.8 mmol/kg 37.0mmol/kg	86
Sweet potato residue	HHP-AP* modified pectin Pectin	Nr.	16.11 28.01	Pb^{2+}	263.15 mg/g 163.93 mg/g	99
Commercial pectin	Chitosan-pectin gel beads	Alkaline solution	6.68	Cu^{2+} Cd^{2+} Hg^{2+} Pb^{2+}	169 mg/g 177.6 mg/g 208.5 mg/g 266.5 mg/g	88
Sugar beet pectin	Pectin xerogel beds	Ca^{2+}	<50	Cd^{2+} Pb^{2+} Cu^{2+}	0.151 mmol/g 0.290 mmol/g 0.343 mmol/g	89
Citrus pectin	Pectin microspheres LM pectin microspheres Pectic acid microspheres	Ca^{2+}	47.9 18.04 0.9	Pb^{2+}	127 mg/g 292 mg/g 325 mg/g	100
Citrus peel	Pectin and guar gum beds	Ca^{2+}	20	Pb^{2+}	104.8 mg/g	101
Citrus peel	Pectin-alginate beds	Ca^{2+}	<50	Cu^{2+} Cd^{2+}	2.79 µmol/bead 3.4 µmol/bead	83
Phyllospadix iwatensis	Native Pectin Hydrolized Pectin	Nr.	6.91 2.54	Pb^{2+} Cd^{2+} Pb^{2+} Cd^{2+}	2.447 mM/g 1.643 mM/g 2.818 mM/g 2.396 mM/g	98
Grapefruit peel	Biochar-pectin-alginate beads	Ca^{2+}	17.5	Cu^{2+}	80.6 mg/g	102
Commercial pectin	Pectin	Ca^{2+}	<50	MB **	354.6 mg/g	103
Orange Waste	Pectin/cellulose microfibers beds	Ca^{2+}	<50	Fe^{2+} Cu^{2+} Cd^{2+}	98.0 mg/g 88.5 mg/g 192.3 mg/g	104

REFERENCES:

1. Mohnen, D. Pectin structure and biosynthesis. *Curr. Opin. Plant Biol.* **11**, 266–277 (2008).

2. Mellerowicz, E. J. & Sundberg, B. Wood cell walls: biosynthesis, developmental dynamics and their implications for wood properties. *Curr. Opin. Plant Biol.* **11**, 293–300 (2008).

3. Voragen, A. G. J., Coenen, G.-J., Verhoef, R. P. & Schols, H. A. Pectin, a versatile polysaccharide present in plant cell walls. *Struct. Chem.* **20**, 263–275 (2009).

4. Baldwin, L. *et al.* Structural alteration of cell wall pectins accompanies pea development in response to cold. *Phytochemistry* **104**, 37–47 (2014).

5. Laurent, M. A. & Boulenguer, P. Stabilization mechanism of acid dairy drinks (ADD) induced by pectin. *Food Hydrocoll.* **17**, 445–454 (2003).

6. Gawkowska, D., Cybulska, J. & Zdunek, A. Structure-related gelling of pectins and linking with other natural compounds: A review. *Polymers (Basel).* **10**, (2018).

7. Morris, G. A., Foster, T. J. & Harding, S. E. The effect of the degree of esterification on the hydrodynamic properties of citrus pectin. *Food Hydrocoll.* **14**, 227–235 (2000).

8. Yapo, B. M. Biochemical Characteristics and Gelling Capacity of Pectin from Yellow Passion Fruit Rind as Affected by Acid Extractant Nature. *J. Agric. Food Chem.* **57**, 1572–1578 (2009).

9. Willats, W. G. T., Knox, J. P. & Mikkelsen, J. D. Pectin: new insights into an old polymer are starting to gel. *Trends Food Sci. Technol.* **17**, 97–104 (2006).

10. Graham b., S. & Knox, J. P. Pectins and their manipulation. *Nat. Prod. Rep.* **20**, xxv–xxv (2003).

11. Zhan, D., Janssen, P. & Mort, A. J. Scarcity or complete lack of single rhamnose residues interspersed within the homogalacturonan regions of citrus pectin. *Carbohydr. Res.* **308**, 373–380 (1998).

12. Voragen, F., Schols, H. & Visser, R. *Advances in Pectin And Pectinase Research*. *Journal of Chemical Information and Modeling* **53**, (2003).

13. Longland, J. M., Fry, S. C. & Trewavas, A. J. Developmental Control of

Apiogalacturonan Biosynthesis and UDP-Apiose Production in a Duckweed 1. *Plant Physiol.* **90**, 972–976 (1989).

14. Whitaker, J. R. Pectic substances, pectic enzymes and haze formation in fruit juices. *Enzyme Microb. Technol.* **6**, 341–349 (1984).

15. Albersheim, P., Darvill, A. G., O'Neill, M. A., Schols, H. A. & Voragen, A. G. J. An hypothesis: The same six polysaccharides are components of the primary cell walls of all higher plants. in *Pectins and Pectinases* (eds. Visser, J. & Voragen, A. G. J. B. T.-P. in B.) **14**, 47–55 (Elsevier, 1996).

16. Clarke, A. E., Anderson, R. L. & Stone, B. A. Form and function of arabinogalactans and arabinogalactan-proteins. *Phytochemistry* **18**, 521–540 (1979).

17. Leivas, C. L., Iacomini, M. & Cordeiro, L. M. C. Pectic type II arabinogalactans from starfruit (Averrhoa carambola L.). *Food Chem.* **199**, 252–257 (2016).

18. Dranca, F. & Oroian, M. Extraction , puri fi cation and characterization of pectin from alternative sources with potential technological applications. *Food Res. Int.* **113**, 327–350 (2018).

19. Kumar, V., Sinha, A. K., Makkar, H. P. S., de Boeck, G. & Becker, K. Dietary Roles of Non-Starch Polysachharides in Human Nutrition: A Review. *Crit. Rev. Food Sci. Nutr.* **52**, 899–935 (2012).

20. Aravantinos-Zafiris, G., Oreopoulou, V., Tzia, C. & Thomopoulos, C. D. Fibre Fraction from Orange Peel Residues after Pectin Extraction. *LWT - Food Sci. Technol.* **27**, 468–471 (1994).

21. Sharma, K., Mahato, N., Cho, M. H. & Lee, Y. R. Converting citrus wastes into value-added products: Economic and environmently friendly approaches. *Nutrition* **34**, 29–46 (2017).

22. Naghshineh, M., Olsen, K. & Georgiou, C. A. Sustainable production of pectin from lime peel by high hydrostatic pressure treatment. *Food Chem.* **136**, 472–478 (2013).

23. Yapo, B. M., Robert, C., Etienne, I., Wathelet, B. & Paquot, M. Effect of extraction conditions on the yield, purity and surface properties of sugar beet pulp pectin extracts. *Food Chem.* **100**, 1356–1364 (2007).

24. Li, D. *et al.* Combined effects of independent variables on yield and protein content of pectin extracted from sugar beet pulp by citric acid. *Carbohydr. Polym.* **129**, 108–114 (2015).

25. Valle, M. Del & Torija, M. Chemical characterization of tomato pomace. **1236**, 1232–1236 (2006).

26. Stabnikova, O., Wang, J.-Y. & Ivanov, V. Value-Added Biotechnological Products from

Organic Wastes BT - Environmental Biotechnology. in (eds. Wang, L. K., Ivanov, V. & Tay, J.-H.) 343–394 (Humana Press, 2010). doi:10.1007/978-1-60327-140-0_8

27. Banerjee, J. *et al.* Bioactives from fruit processing wastes: Green approaches to valuable chemicals. *Food Chem.* **225**, 10–22 (2017).

28. Happi Emaga, T., Ronkart, S. N., Robert, C., Wathelet, B. & Paquot, M. Characterisation of pectins extracted from banana peels (Musa AAA) under different conditions using an experimental design. *Food Chem.* **108**, 463–471 (2008).

29. Martínez-Sabando, J., Coin, F., Melillo, J. H., Goyanes, S. & Cerveny, S. A Review of Pectin-Based Material for Applications in Water Treatment. *Materials* **16**, (2023).

30. Methacanon, P., Krongsin, J. & Gamonpilas, C. Pomelo (Citrus maxima) pectin: Effects of extraction parameters and its properties. *Food Hydrocoll.* **35**, 383–391 (2014).

31. Panouillé Maud, Thibault, J.-F. & Bonnin, E. Cellulase and Protease Preparations Can Extract Pectins from Various Plant Byproducts. *J. Agric. Food Chem.* **54**, 8926–8935 (2006).

32. Yapo, B. M. Pectin quantity, composition and physicochemical behaviour as influenced by the purification process. *Food Res. Int.* **42**, 1197–1202 (2009).

33. Lin, L. *et al.* Structural elucidation of a pectin from flowers of Lonicera japonica and its antipancreatic cancer activity. *Int. J. Biol. Macromol.* **88**, 130–137 (2016).

34. Patra, P., Das, D., Behera, B., Maiti, T. K. & Islam, S. S. Structure elucidation of an immunoenhancing pectic polysaccharide isolated from aqueous extract of pods of green bean (Phaseolus vulgaris L.). *Carbohydr. Polym.* **87**, 2169–2175 (2012).

35. Li, P., Xia, J., Nie, Z. & Shan, Y. Pectic oligosaccharides hydrolyzed from orange peel by fungal multi-enzyme complexes and their prebiotic and antibacterial potentials. *LWT - Food Sci. Technol.* **69**, 203–210 (2016).

36. Moore, J. P. *et al.* Profiling the main cell wall polysaccharides of grapevine leaves using high-throughput and fractionation methods. *Carbohydr. Polym.* **99**, 190–198 (2014).

37. Giacomazza, D., Bulone, D., San Biagio, P. L., Marino, R. & Lapasin, R. The role of sucrose concentration in self-assembly kinetics of high methoxyl pectin. *Int. J. Biol. Macromol.* **112**, 1183–1190 (2018).

38. Saha, D. & Bhattacharya, S. Hydrocolloids as thickening and gelling agents in food: a critical review. *J. Food Sci. Technol.* **47**, 587–597 (2010).

39. Oakenfull, D. G. CHAPTER 5 - The Chemistry of High-Methoxyl Pectins. in *Food*

Science and Technology (ed. Walter, R. H. B. T.-T. C. and T. of P.) 87–108 (Academic Press, 1991). doi:https://doi.org/10.1016/B978-0-08-092644-5.50010-8

40. Kim, M. H., Park, H. & Park, W. H. Effect of pH and precursor salts on in situ formation of calcium phosphate nanoparticles in methylcellulose hydrogel. *Carbohydr. Polym.* **191**, 176–182 (2018).

41. Li, D. *et al.* Pectin in biomedical and drug delivery applications: A review. *Int. J. Biol. Macromol.* **185**, 49–65 (2021).

42. Thibault, J.-F. & Ralet, M.-C. Physico-Chemical Properties of Pectins in the Cell Walls and After Extraction BT - Advances in Pectin and Pectinase Research. in (eds. Voragen, F., Schols, H. & Visser, R.) 91–105 (Springer Netherlands, 2003). doi:10.1007/978-94-017-0331-4_7

43. Morris, E. R., Powell, D. A., Gidley, M. J. & Rees, D. A. Conformations and interactions of pectins: I. Polymorphism between gel and solid states of calcium polygalacturonate. *J. Mol. Biol.* **155**, 507–516 (1982).

44. Powell, D. A., Morris, E. R., Gidley, M. J. & Rees, D. A. Conformations and interactions of pectins: II. Influence of residue sequence on chain association in calcium pectate gels. *J. Mol. Biol.* **155**, 517–531 (1982).

45. Grant, G. T., Morris, E. R., Rees, D. A., Smith, P. J. C. & Thom, D. Biological interactions between polysaccharides and divalent cations: The egg-box model. *FEBS Lett.* **32**, 195–198 (1973).

46. Luzio, G. A. & Cameron, R. G. Demethylation of a model homogalacturonan with the salt-independent pectin methylesterase from citrus: Part II. Structure–function analysis. *Carbohydr. Polym.* **71**, 300–309 (2008).

47. Braccini, I. & Pérez, S. Molecular Basis of Ca2+-Induced Gelation in Alginates and Pectins: The Egg-Box Model Revisited. *Biomacromolecules* **2**, 1089–1096 (2001).

48. Gohil, R. M. Synergistic blends of natural polymers, pectin and sodium alginate. *J. Appl. Polym. Sci.* **120**, 2324–2336 (2011).

49. Fraeye, I. *et al.* Influence of pectin structure on texture of pectin-calcium gels. *Innov. Food Sci. Emerg. Technol.* **11**, 401–409 (2010).

50. Yoshimura, T., Sengoku, K. & Fujioka, R. Pectin-based surperabsorbent hydrogels crosslinked by some chemicals: Synthesis and characterization. *Polym. Bull.* **55**, 123–129 (2005).

51. Chen, B., McClements, D. J., Gray, D. A. & Decker, E. A. Stabilization of Soybean Oil

Bodies by Enzyme (Laccase) Cross-Linking of Adsorbed Beet Pectin Coatings. *J. Agric. Food Chem.* **58**, 9259–9265 (2010).

52. Chen, R. *et al.* The influence of pH and monovalent ions on the gelation of pectin from the fruit seeds of the creeping fig plant. *Food Hydrocoll.* **111**, 106219 (2021).

53. Wang, H. *et al.* Unexpected gelation behavior of citrus pectin induced by monovalent cations under alkaline conditions. *Carbohydr. Polym.* **212**, 51–58 (2019).

54. Jonassen, H., Treves, A., Kjøniksen, A.-L., Smistad, G. & Hiorth, M. Preparation of Ionically Cross-Linked Pectin Nanoparticles in the Presence of Chlorides of Divalent and Monovalent Cations. *Biomacromolecules* **14**, 3523–3531 (2013).

55. Ström, A., Schuster, E. & Goh, S. M. Rheological characterization of acid pectin samples in the absence and presence of monovalent ions. *Carbohydr. Polym.* **113**, 336–343 (2014).

56. Yoo, S.-H., Fishman, M. L., Savary, B. J. & Hotchkiss, A. T. Monovalent Salt-Induced Gelation of Enzymatically Deesterified Pectin. *J. Agric. Food Chem.* **51**, 7410–7417 (2003).

57. Chaichi, M., Badii, F., Mohammadi, A. & Hashemi, M. Water resistance and mechanical properties of low methoxy-pectin nanocomposite film responses to interactions of Ca2+ ions and glycerol concentrations as crosslinking agents. *Food Chem.* **293**, 429–437 (2019).

58. Ngouémazong, D. E. *et al.* Effect of debranching on the rheological properties of Ca2+–pectin gels. *Food Hydrocoll.* **26**, 44–53 (2012).

59. Yang, X. *et al.* Low methoxyl pectin gelation under alkaline conditions and its rheological properties: Using NaOH as a pH regulator. *Food Hydrocoll.* **79**, 560–571 (2018).

60. Capel, F., Nicolai, T., Durand, D., Boulenguer, P. & Langendorff, V. Calcium and acid induced gelation of (amidated) low methoxyl pectin. *Food Hydrocoll.* **20**, 901–907 (2006).

61. Yuliarti, O., Hoon, A. L. S. & Chong, S. Y. Influence of pH, pectin and Ca concentration on gelation properties of low-methoxyl pectin extracted from Cyclea barbata Miers. *Food Struct.* **11**, 16–23 (2017).

62. Tkalec, G., Knez, Ž. & Novak, Z. PH sensitive mesoporous materials for immediate or controlled release of NSAID. *Microporous Mesoporous Mater.* **224**, 190–200 (2016).

63. Kohila rani, K., Liu, Y.-X., Devasenathipathy, R., Yang, C. & Wang, S.-F. Simple preparation of gold nanoparticle-decorated copper cross-linked pectin for the sensitive determination of hydrogen peroxide. *Ionics (Kiel).* **25**, 309–317 (2019).

64. Nešić, A. *et al.* Design of pectin-sodium alginate based films for potential healthcare

application: Study of chemico-physical interactions between the components of films and assessment of their antimicrobial activity. *Carbohydr. Polym.* **157**, 981–990 (2017).

65. Wehr, J. B. *et al.* Hydrolysis and Speciation of Al Bound to Pectin and Plant Cell Wall Material and Its Reaction with the Dye Chrome Azurol S. *J. Agric. Food Chem.* **58**, 5553–5560 (2010).

66. McKenna, B. A., Nicholson, T. M., Wehr, J. B. & Menzies, N. W. Effects of Ca, Cu, Al and La on pectin gel strength: implications for plant cell walls. *Carbohydr. Res.* **345**, 1174–1179 (2010).

67. Wu, X. *et al.* Fully physically crosslinked pectin-based hydrogel with high stretchability and toughness for biomedical application. *Int. J. Biol. Macromol.* **149**, 707–716 (2020).

68. Pellerin, P. & O'Neill, M. A. The interaction of the pectic polysaccharide Rhamnogalacturonan II with heavy metals and lanthanides in wines and fruit juices. *Analusis* **26**, 32–36 (1998).

69. Assifaoui, A. *et al.* Structural behaviour differences in low methoxy pectin solutions in the presence of divalent cations (Ca2+ and Zn2+): a process driven by the binding mechanism of the cation with the galacturonate unit. *Soft Matter* **11**, 551–560 (2015).

70. Huynh, U. T. D., Lerbret, A., Neiers, F., Chambin, O. & Assifaoui, A. Binding of Divalent Cations to Polygalacturonate: A Mechanism Driven by the Hydration Water. *J. Phys. Chem. B* **120**, 1021–1032 (2016).

71. Assifaoui, A., Loupiac, C., Chambin, O. & Cayot, P. Structure of calcium and zinc pectinate films investigated by FTIR spectroscopy. *Carbohydr. Res.* **345**, 929–933 (2010).

72. Gavahian, M., Mathad, G. N., Pandiselvam, R., Lin, J. & Sun, D.-W. Emerging technologies to obtain pectin from food processing by-products: A strategy for enhancing resource efficiency. *Trends Food Sci. Technol.* **115**, 42–54 (2021).

73. Hu, W., Cassard, A.-M. & Ciocan, D. Pectin in Metabolic Liver Disease. *Nutrients* **15**, (2023).

74. Houron, C. *et al.* Gut Microbiota Reshaped by Pectin Treatment Improves Liver Steatosis in Obese Mice. *Nutrients* **13**, (2021).

75. Munarin, F. *et al.* Pectin-Based Injectable Biomaterials for Bone Tissue Engineering. *Biomacromolecules* **12**, 568–577 (2011).

76. Freitas, C. M., Coimbra, J. S., Souza, V. G. & Sousa, R. C. Structure and Applications of Pectin in Food, Biomedical, and Pharmaceutical Industry: A Review. *Coatings* **11**, (2021).

77. Moslemi, M. Reviewing the recent advances in application of pectin for technical and health promotion purposes: From laboratory to market. *Carbohydr. Polym.* **254**, 117324 (2021).

78. Reichembach, L. H. & Lúcia de Oliveira Petkowicz, C. Pectins from alternative sources and uses beyond sweets and jellies: An overview. *Food Hydrocoll.* **118**, 106824 (2021).

79. Oliva-Moreno, E. E. & Encinas, A. Addition of Pine Rosin to Pectin bioplastic films for improved water resistance. *Mater. Lett.* **290**, 129488 (2021).

80. Espitia, P. J. P., Du, W. X., Avena-Bustillos, R. de J., Soares, N. de F. F. & McHugh, T. H. Edible films from pectin: Physical-mechanical and antimicrobial properties - A review. *Food Hydrocoll.* **35**, 287–296 (2014).

81. Huang, S. *et al.* Fabrication and performance evaluation of pectin–fish gelatin–resveratrol preservative films. *Food Chem.* **361**, 129832 (2021).

82. Makaremi, M. *et al.* Safely dissolvable and healable active packaging films based on alginate and pectin. *Polymers (Basel).* **11**, 1–18 (2019).

83. Cataldo, S., Gianguzza, A., Pettignano, A. & Villaescusa, I. Mercury(II) removal from aqueous solution by sorption onto alginate, pectate and polygalacturonate calcium gel beads. A kinetic and speciation based equilibrium study. *React. Funct. Polym.* **73**, 207–217 (2013).

84. Celus, M. *et al.* Fe2+ adsorption on citrus pectin is influenced by the degree and pattern of methylesterification. *Food Hydrocoll.* **73**, 101–109 (2017).

85. Yu, L. *et al.* Pectin microgel particles as high adsorption rate material for methylene blue: Performance, equilibrium, kinetic, mechanism and regeneration studies. *Int. J. Biol. Macromol.* **112**, 383–389 (2018).

86. Wang, R., Zhu, X., Qian, W., Yu, Y. & Xu, R. Effect of pectin on adsorption of Cu(II) by two variable-charge soils from southern China. *Environ. Sci. Pollut. Res.* **22**, 19687–19694 (2015).

87. Brian., S. C. *Fundamental of Fourier Transform Infrared Spectroscopy Second Edition*. (2011). doi:10.1002/1521-3773(20010316)40:6<9823::AID-ANIE9823>3.3.CO;2-C

88. Shao, Z. *et al.* Novel green chitosan-pectin gel beads for the removal of Cu(II), Cd(II), Hg(II) and Pb(II) from aqueous solution. *Int. J. Biol. Macromol.* **176**, 217–225 (2021).

89. Mata, Y. N., Blázquez, M. L., Ballester, A., González, F. & Muñoz, J. A. Optimization of the continuous biosorption of copper with sugar-beet pectin gels. *J. Environ. Manage.* **90**, 1737–1743 (2009).

90. Kartel, M. T., Kupchik, L. A. & Veisov, B. K. Evaluation of pectin binding of heavy metal ions in aqueous solutions. *Chemosphere* **38**, 2591–2596 (1999).

91. Wang, X., Chen, Q. & Lü, X. Pectin extracted from apple pomace and citrus peel by subcritical water. *Food Hydrocoll.* **38**, 129–137 (2014).

92. Garna, H. *et al.* Effect of Extraction Conditions on the Yield and Purity of Apple Pomace Pectin Precipitated but Not Washed by Alcohol. *J. Food Sci.* **72**, C001–C009 (2007).

93. Ralet, M.-C., Crépeau, M.-J., Buchholt, H.-C. & Thibault, J.-F. Polyelectrolyte behaviour and calcium binding properties of sugar beet pectins differing in their degrees of methylation and acetylation. *Biochem. Eng. J.* **16**, 191–201 (2003).

94. Löfgren, C., Guillotin, S., Evenbratt, H., Schols, H. & Hermansson, A.-M. Effects of Calcium, pH, and Blockiness on Kinetic Rheological Behavior and Microstructure of HM Pectin Gels. *Biomacromolecules* **6**, 646–652 (2005).

95. Khotimchenko, M., Kovalev, V. & Khotimchenko, Y. Equilibrium studies of sorption of lead(II) ions by different pectin compounds. *J. Hazard. Mater.* **149**, 693–699 (2007).

96. Kyomugasho, C. *et al.* Pectin nanostructure influences pectin-cation interactions and in vitro-bioaccessibility of Ca2+, Zn2+, Fe2+ and Mg2+-ions in model systems. *Food Hydrocoll.* **62**, 299–310 (2017).

97. Cao, L., Lu, W., Mata, A., Nishinari, K. & Fang, Y. Egg-box model-based gelation of alginate and pectin: A review. *Carbohydr. Polym.* **242**, 116389 (2020).

98. Khozhaenko, E., Kovalev, V., Podkorytova, E. & Khotimchenko, M. Removal of the metal ions from aqueous solutions by nanoscaled low molecular pectin isolated from seagrass Phyllospadix iwatensis. *Sci. Total Environ.* **565**, 913–921 (2016).

99. Mudugamuwa Arachchige, M. P., Mu, T. & Ma, M. Effect of high hydrostatic pressure-assisted pectinase modification on the Pb2+ adsorption capacity of pectin isolated from sweet potato residue. *Chemosphere* **262**, 128102 (2021).

100. Li, F. *et al.* Preparation and characterization of Ca(II) cross-linking modified pectin microspheres for Pb(II) adsorption. *Water Sci. Technol.* **79**, 1484–1493 (2019).

101. Subroto, N. N. P., Tarmidzi, F. M., Wati, I. & Armans, V. M. Lead Ion Removal in Water Using Low Methoxy Pectin-Guar Gum Beads Hybrid Adsorbent. *Indo. J. Chem. Res.* **10**, 53–57 (2022).

102. Zhang, W. *et al.* Novel pectin based composite hydrogel derived from grapefruit peel for enhanced Cu(II) removal. *J. Hazard. Mater.* **384**, 121445 (2020).

103. Li, D., Wang, J., Guo, Z., Li, J. & Shuai, J. Pectin gels cross-linked by Ca2+: An efficient material for methylene blue removal. *J. Mol. Liq.* **238**, 36–42 (2017).

104. Lessa, E. F., Medina, A. L., Ribeiro, A. S. & Fajardo, A. R. Removal of multi-metals from water using reusable pectin/cellulose microfibers composite beads. *Arab. J. Chem.* **13**, 709–720 (2020).

Chapter 4

Materials and Methods

This chapter summarizes the protocols for preparing the pectin films and their crosslinking with the different crosslinking agents. We also described the batch experiments done for crosslinking and the models we used to analyze the adsorption data. Additionally, we present the contaminants used and the batch experiments for adsorption. Finally, we summarize all the experimental techniques used in this thesis.

4.1. Materials

4.1.1. Pectin-based film preparation

Herbstreith and Fox gently provided low-methoxyl pectin (methylation degree, DM = 9.9%). Glycerol was purchased from Merck and was used without any further purification.

Pectin-based films were produced by the solvent-casting method. Solvent casting, also known as the casting method, remains the prevailing approach for film formation in laboratory and at pilot scales. The determining factor is the polymer's solubility rather than its melting characteristics[1]. This technique encompasses a three-step process for the creation of biopolymer films[2]:

1) Dissolution of the biopolymer in a compatible solvent.

2) Pouring the solution into a mold.

3) Air-drying the casted solution until solidification is achieved.

Deionized water (pH = 7) was used as a solvent since pectin is water-soluble. In addition, we have added 6% w/v glycerol to provide homogenization in the final film.

3% w/v pectin solutions were prepared in an Erlenmeyer flask under vigorous magnetic stirring. The stirring was kept for 1.5 hours at a temperature of 70 ℃ until homogeneous dissolution was achieved. The solution was then ultrasonicated (at 70 ℃ for 1.5 h) to homogenize and eliminate any bubbles in the viscous solution. 10 ml of the casting solution was poured onto a Petri dish covering the entire surface. Solvent evaporation was performed in a vacuum chamber for 12 hours. Finally, thin hydrogels were carefully detached from the petri dish, dried in a vacuum oven at 40 ºC, and stored until further use.

4.1.2. Pectin-based film crosslinking

The crosslink was performed by exposing the pectin films in aqueous solutions containing the corresponding crosslinking agent. Cross-linking solutions were prepared from calcium chloride ($CaCl_2$) or europium chloride hexahydrate ($EuCl_3$) purchased from Merck and used without any further purification. pH was kept constant at 7, adding 0.1 M de NaOH.

Crosslink was performed using a fixed amount of adsorbent (2.5 g/L) and varying initial Ca^{+2} or Eu^{+3} concentrations in the 25−1500 mg/L range. Batch experiments were prepared in 20 mL tubes, and equilibrium concentration was measured after 24 hours. Kinetic adsorption studies were prepared at a fixed cross-linking agent concentration (500 mg/L) at different times (10 to 1440 min).

Three crosslinking procedures were performed

Ca^{+2} crosslinking: Pectin films were crosslinked with calcium chloride ($CaCl_2$). The dried pectin films were immersed in 500 mg/L of Ca^{2+} solution for 40 min.

Eu^{+3} crosslinking: Pectin films were crosslinked with europium chloride ($EuCl_3$). The dried pectin films were immersed in 500 mg/L of Eu^{3+} solution for 40 min.

Ca^{+2} and Eu^{+3} crosslinking: We first crosslinked the dried pectin films with 500 mg/L of Ca^{2+} solution for 40 min, followed by crosslinking with Eu^{3+} for 40 min.

In the three cases, after crosslinking, the films were rinsed five times with 200 ml of deionized water for 1 h to remove excess crosslinking agent.

In this way, we obtained three pectin films with different crosslinking systems: P–Ca (samples crosslinked by Ca^{2+}), P–Eu (samples crosslinked by Eu^{3+}), and P–Ca–Eu (samples crosslinked by dual crosslinking).

4.1.3 Batch adsorption experiments for crosslinking monitoring

Adsorption isotherm and kinetic experiments were performed to ascertain the maximum adsorption capacities and suitable crosslinking levels for each sample.

4.1.3.1. Crosslinking reactions

Adsorption isotherms were obtained using adsorbents with different initial Ca^{2+} or Eu^{3+} concentrations in the range of 25–1500 mg/L. A fixed amount of adsorbent (2.5 g/L) was used for each measurement. Batch experiments were performed in 20 mL tubes, and the equilibrium concentration was measured after 24 h. Kinetic adsorption studies were performed at a fixed crosslinking agent concentration (500 mg/L) for different durations (10 to 1440 min). Crosslinking solutions were prepared from $CaCl_2$ or $EuCl_3$, and the pH was maintained at 7 by adding 0.1 M NaOH.

The equilibrium concentration (C_{eq}) and concentration at time t (C_t) were measured using ICP–AES. The amount of adsorbed crosslinking agent was determined based on the difference between the initial and final concentrations in the solution. Aliquots were collected at certain intervals to measure C_t, and C_{eq} was taken as the equilibrium value of C_t. The equilibrium adsorption capacity (q_{eq}; mg/g) and adsorption at time t (q_t; mg/g) were calculated as follows:

$$q_{eq} = \frac{C_0 - C_{eq}}{d} \quad (1)$$

$$q_t = \frac{C_0 - C_t}{d} \quad (2)$$

where C_0 is initial concentration of a given crosslinking agent (mg/L) and d is the adsorbent dose. The removal efficiency (R%) was calculated as follows:

$$R\% = \left(\frac{(C_0 - C_{eq})}{C_0}\right) \times 100\% \quad (3)$$

4.1.4. Materials for batch adsorption experiments – contaminants

In this thesis, we have work with two types of contaminants: heavy metals and pharmaceuticals products. Among heavy metals, we have used: Zinc, Nickel and Barium.

Among pharmaceuticals products, we have used: (ciprofloxacin (CIP), tetracycline (TC), trimethoprim (TMP)), and one antihistamine (chlorpheniramine maleate (CPM). Figure 1 shows the molecular structure of the antibiotics, antihistamine, and anti-inflammatory products used.

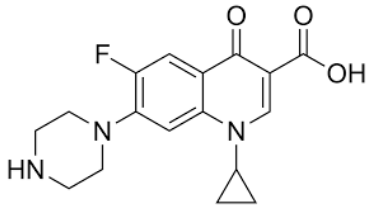

CIPROFLOXACIN (CIP)

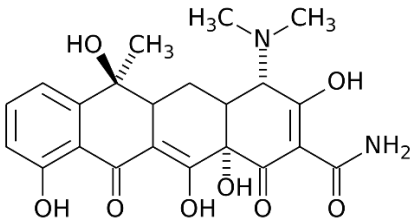

TETRACICLINE (TC)

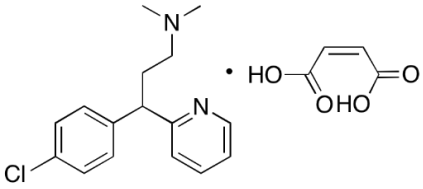

CHLORPHENIRAMINE MALEATE (CPM)

Figure 1. Pharmaceutical products used in this thesis.

4.1.5. Batch adsorption experiments for adsorption of heavy metals and pharmaceuticals

Adsorption experiments were performed in batches using a dose of 0.5 g/L, 1 g/L and 2.5 g/L under agitation at 125 rpm and (25 ± 1) °C.

Adsorption isotherms were measured at various initial pollutant concentrations. For the kinetic experiments, we measured the pollutant concentration at different times ranging from 10 to 1440 min at a fixed initial concentration of 150 mg/L for zinc, barium, and at 50 mg/L for the pharmaceuticals. In the event that a kinetic experiment is conducted with a distinct initial concentration of the pollutant, the specific details regarding the altered pollutant concentration will be explicitly stated.

In both the cases, the equilibrium concentration (C_{eq}) and concentration at time t (C_t) were measured using ICP–AES for the heavy metals whereas UV–Vis was used to determine C_{eq} and C_t for pharmaceuticals. The amount of adsorbed pollutant was determined based on the difference between the initial and final concentrations in the solution. Aliquots were collected at certain intervals to measure C_t, and C_{eq} was taken as the equilibrium value of C_t. The equilibrium adsorption capacity (q_{eq}; mg/g) and adsorption at time t (q_t; mg/g) were calculated using the equations (1) and (2) and the removal efficiency (R%) using the equation (3).

4.1.6 Adsorption data analysis

All models to fit isotherms and kinetic experiments were detailed and explained in Chapter 2. Here, we only summarize the models we have used in this Thesis.

The adsorption isotherms were fitted using the Langmuir (Eq. 4) and Redlich–Peterson (Eq. 5) models.

$$q(C_{\mathrm{eq}}) = \frac{q_{\mathrm{M}}\, K_{\mathrm{L}}\, C_{\mathrm{eq}}}{1 + K_{\mathrm{L}} C_{\mathrm{eq}}} \tag{4}$$

$$q(C_{\mathrm{eq}}) = \frac{K_{\mathrm{RP}}\, C_{\mathrm{eq}}}{1 + \alpha\, {C_{\mathrm{eq}}}^{\beta}} \tag{5}$$

where q is the adsorption capacity; q_{M} is the maximum adsorption capacity; K_{L} is the Langmuir constant; and KL_{RP}, β, and α are Redlich–Peterson constants. β is a dimensionless parameter between 0 and 1, representing the heterogeneity factor. The closer the value to zero, the more heterogeneous the surface where the adsorbate interacts.

The adsorption data were analyzed using a nonlinear fitting of the empirical pseudo-first-order (PFO; Eq. 6) and pseudo-second-order (PSO; Eq. 7) kinetic models.

$$\text{PFO:} \quad q_t = q_{\mathrm{e}}(1 - \mathrm{e}^{-k_1 t}) \tag{6}$$

$$\text{PSO:} \quad q_t = \frac{q_{\mathrm{e}}^2 k_2 t}{1 + q_{\mathrm{e}}\, k_2 t} \tag{7}$$

where k_1 and k_2 are the characteristic time-related constants of the PFO and PSO models, respectively, indicating the adsorption speed at the beginning of the adsorption process.

All these models were detailed explained in Chapter 2.

4.2. Experimental tehcniques

4.2.1. Infrared Spectroscopy (FTIR)

Certain spectroscopic techniques use electromagnetic radiation to gather insights into atoms and molecules by examining the interactions between the analyzed sample (matter) and energy (a specific portion of the electromagnetic spectrum)[3]. The electromagnetic spectrum spans a vast range, encompassing long wavelengths (with low frequencies) employed in modern radio communication, and short wavelengths (with high frequencies) associated with gamma radiation. This expansive spectrum covers wavelengths ranging from kilometers to dimensions smaller than an atom.

Regarding the range of the infrared region (expressed in wavenumbers; 12800 - 33 cm^{-1}), it can be categorized into three distinct regions: the near-infrared region (12800 - 4000 cm^{-1}), the mid-infrared region (4000 – 200 cm^{-1}), and the far-infrared region (200 - 33 cm^{-1})[4]. This thesis primarily focuses on the mid-infrared region (see Figure 2).

When the wavelength of the infrared (IR) radiation approaches the natural frequency of distinct molecular vibrations, the molecule absorbs it, leading to its excitation into a higher vibrational state[5]. The frequency can also emerge as the summation of two natural frequencies, constituting a "combination" of two vibrations. The resultant outcome is an infrared (IR) spectrum that signifies the absorption of infrared light by a sample, showcasing the wavelengths and intensities of these absorptions. Thus, it creates a distinctive molecular fingerprint. This fingerprint manifests as absorption peaks that correspond to the vibrational frequencies of atomic bonds within the material. As each compound possesses a unique amalgamation of atoms, no two compounds exhibit the same infrared spectrum. Capitalizing on this principle, infrared absorption spectroscopy serves as a tool for characterizing molecular structures and identifying functional groups based on their characteristic infrared absorption patterns.

In this thesis, the infrared spectroscopy technique was mainly used to determine the principal chemical functional groups of pectin, variations in the spectra after crosslinking with different systems, and to determine the D.M. of pectin at room temperature. All samples were dried at 40 ºC in a vacuum oven to ensure the same water content throughout all samples. The main focus is on the bands present at 1735cm^{-1} which corresponds to the carbonyl group

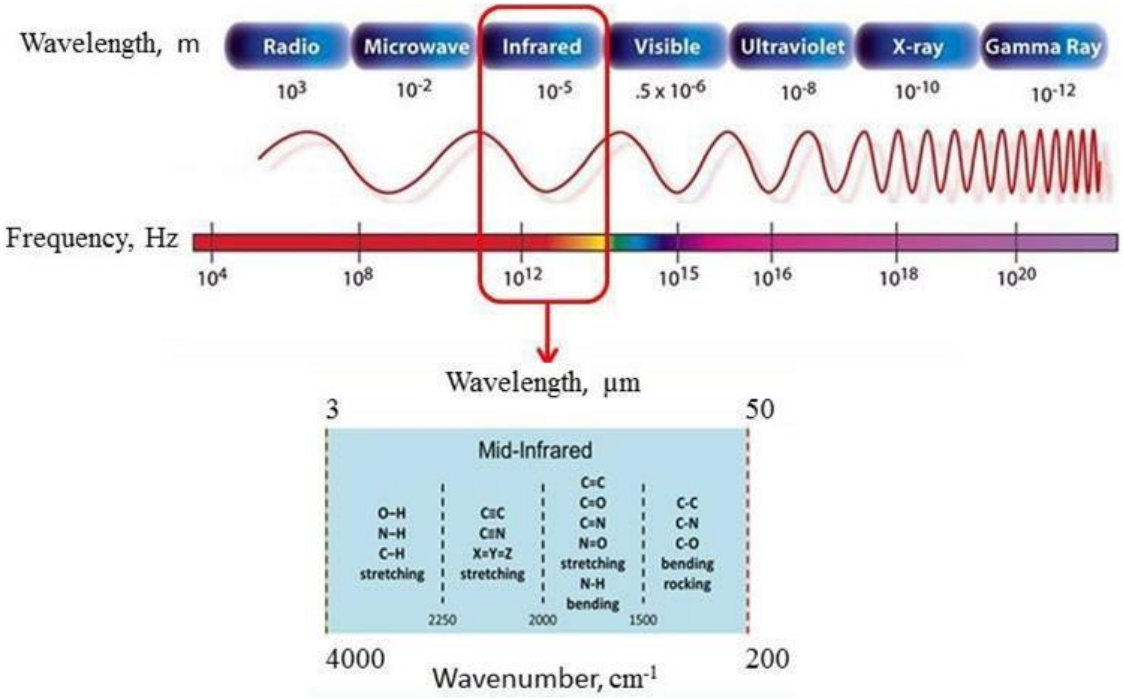

Figure 2. Electromagnetic spectrum (above). Mid-infrared region (4000 - 400 cm^{-1}) (below).

(C=O) present in the carbon 6 of the galacturonic acid residue. This peak is related to the esterified form –$COOCH_3$, On the other hand, the peak at a wavelength of 1630cm^{-1} is associated to the deprotonated carboxyl group (COO^-) and the changes along the crosslink process can be detected in this band.

On the other hand, it is also possible to determine the dree of methylation of pectin using FTIR. The D.M. [%] was obtained normalizing all the FT-IR spectra in function of the intensity of the peak at 1325 cm^{-1}. Subsequently, peaks where deconvoluted in order to obtain the area values. Finally, the D.E. was calculated[6] by the following formula:

$$D.M.[\%] = \left(\frac{A_{1735}}{(A_{1735}+A_{1635})}\right) * 100 \quad (8)$$

where $A_{1735}$is the area of the peak situated at 1735 cm^{-1} and A_{1630} is the area of the peak at 1630 cm^{-1}.

The infrared spectra were acquired utilizing a Jasco 6300 spectrometer, which was outfitted with an attenuated total reflectance (ATR) unit comprising a diamond prism crystal (refer to Figure 3). This setup facilitated sample analysis with minimal preparation. ATR spectroscopy selectively captures spectra from the immediate few microns above the crystal surface, achieved by firmly securing the sample against the crystal to ensure intimate contact. Baselines were rectified using Jasco's Spectra Analysis software, without applying any data smoothing techniques. To establish a reference, a background spectrum was obtained by measuring the air without a sample in the beam. By subtracting the background spectra from the sample measurements, the resulting spectrum lacking of any instrumental artifacts was obtained, ensuring that all spectral characteristics observed were solely attributed to the sample.

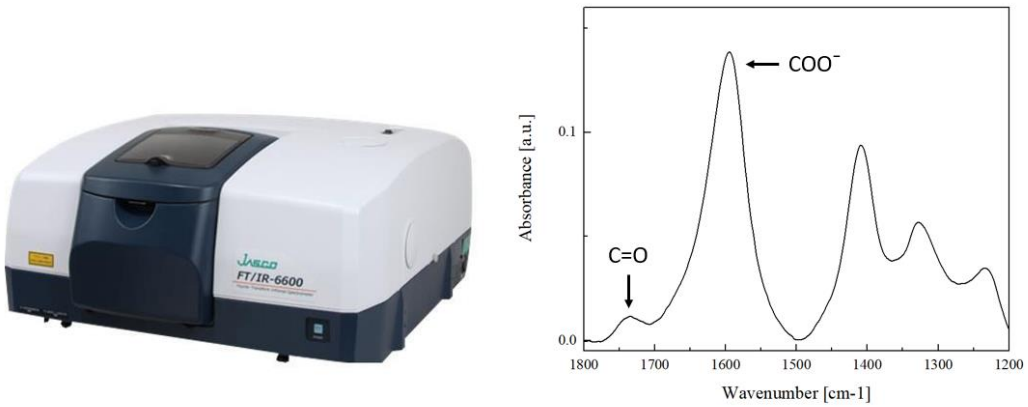

Figure 3. FTIR spectrometer 6000 series by Jasco employed for FTIR experiments (left) and vibration bands for C=O and COO^-(right).

4.2.2. Ultraviolet-Visible spectroscopy (UV-VIS)

Ultraviolet-visible spectroscopy (UV-Vis) is a technique used to analyze the interaction between light and matter in the visible and adjacent near-UV and near-IR ranges. It involves studying the absorption and transmission of ultraviolet (UV) and visible light by a sample. UV-Vis spectroscopy provides information about the electronic structure and composition of substances. The basic principle behind UV-Vis spectroscopy is that atoms, molecules, or ions can absorb specific wavelengths of light, causing electrons to transition from lower energy states to higher energy states. These transitions occur within the UV and visible regions of the electromagnetic spectrum and it can occur in transition metal ions, including d-d transitions and metal-ligand chain transfers, and inorganic and organic molecules, especially n-π* and π-π* orbital transitions in double bonds from conjugated organic compounds. Electrons with small energy gaps between the Highest Occupied Molecular Orbital (HOMO) and the Lowest Unoccupied Molecular Orbital (LUMO), and therefore easily excited to higher orbitals, absorb light at longer wavelengths than those with larger gaps.

In practice, a UV-Vis spectrophotometer is used to measure the intensity of light passing through a sample at different wavelengths. The spectrophotometer emits a beam of light that passes through the sample, and a detector measures the intensity of the transmitted light. By scanning across a range of wavelengths, a UV-Vis spectrum is generated, which represents the absorption or transmission characteristics of the sample.

Figure 4. UV-Vis equipment

The Beer-Lambert law relates the attenuation of light to the properties of the material through which the light is traveling. The absorbance of a solution (A) is directly proportional to

the concentration of the solute (c) and the optical path length (ℓ). The expression of the Beer–Lambert law is

$$A = log_{10} \frac{Io}{I} = \varepsilon \, c \, \ell \tag{9}$$

where Io is the incident intensity of light, I the transmitted intensity and ε is the molar attenuation coefficient, which is an intrinsic property of the sample. Beer-Lambert law is often only valid for values of A < 1.

In this thesis, UV-Vis spectra were recorded in an Agilent 8453A UV-Vis spectrometer with Peltier thermostatic cell holder T-controller 89096A (Figure 4.).

The application of the Beer-Lambert law involved constructing calibration curves using known concentrations ranging from 1 to 50 mg/L (see Figure 5(a)) in order to establish a correlation between the adsorption intensity of each solution and its concentration. Subsequently, a plot of absorbance at a certain peak (characteristic to each compound) against concentration was generated (see Figure 5(b)). This plot was then subjected to linear regression analysis, and if a satisfactory correlation was achieved (indicated by a higher Adj R^2 value closer to 1, indicating a good fit), the obtained slope could be employed to determine the concentration of an unknown solution by dividing its absorbance by the slope of the calibration curve. This is the methodology employed to ascertain the concentrations of pharmaceuticals in solutions.

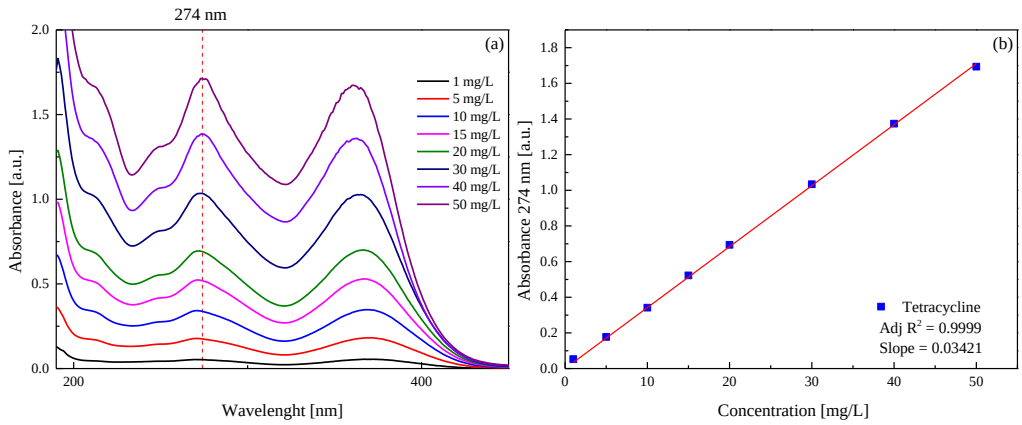

Figure 5. Obtained UV-Vis spectra for tetracycline at different concentrations (a) and calibration curve with the absorbance at the peak situated at 274 nm (b).

4.2.4. Energy-dispersive X-ray spectroscopy (EDX)

Energy Dispersive X-Ray Analysis (EDX) is a method that utilizes X-rays to determine the elemental composition of materials. EDX systems are incorporated into Electron Microscopy instruments, such as scanning electron microscopy (SEM) or Transmission Electron Microscopy (TEM), where the microscope's imaging capability helps identify the specific specimen under examination. The information obtained from EDX analysis comprises spectra that exhibit peaks corresponding to the elements present in the actual composition of the sample being studied.

The EDX-SEM measurements were done in the CIC-nanogune center using a Quanta 250 ESEM, FEI, Netherlands, and energy dispersive X-ray (EDX) spectroscopy (silicon drift detector, EDAX). The beam voltage and current were set to 10 kV and 5 pA, respectively. Electrons were detected using a large-field detector in low-vacuum mode. The chamber was evacuated to 80 Pa. The samples were mounted on an aluminum stub using double-sided tape.

4.2.5. Inductively Coupled Plasma-Atomic Emission Spectroscopy (ICP-AES)

Inductively coupled plasma atomic emission spectroscopy (ICP-AES) is an analytical technique to detect chemical elements, often-metal atoms, in solution. This technique uses inductively coupled plasma to excite atoms and ions emitting light at characteristic wavelengths. A gas (usually argon) is ionized in a plasma source, forming a plasma. The free electrons are accelerated by an electromagnetic field, producing more ions and heating the plasma to 6000-10000 K. Then, the sample is introduced into the flame. The plasma's heat breaks the chemical bonds of the sample molecules, and the free atoms are excited into excited electronic states. When the excited electrons return to the ground state, they emit photons of a frequency characteristic to each element. This light is detected by a spectrometer[7].

In this thesis, inductively coupled plasma–atomic emission spectrometry (ICP–AES; Agilent 5100) was used to measure the concentrations of heavy metals and crosslinking agents (Ca^{2+} and Eu^{3+}).

4.2.6. X-ray Diffraction (XDR)

X-ray diffraction enables the analysis of material crystallinity, phase composition, and the determination of crystallite size. Since the wavelength of X-rays is similar to the distance between crystal layers, incident X-rays will be diffracted, interacting with certain crystalline layers and diffraction patterns containing important structural information about the crystal can be obtained. The diffraction pattern is considered the fingerprint of the crystal because each crystal structures produce unique diffraction patterns and every phase in a mixture produces its

diffraction pattern independently. We can use grinded bulk sample into fine powders, which are typical under 10 μm,2 as samples in powder X-ray Diffraction (XRD).

By directing an X-ray beam onto a sample, the material's electrons scatter the electromagnetic radiation. While destructive interference occurs for most of the waves, the application of Bragg's law leads to a constructive component emerging when the X-rays meet specific conditions. (equation x)[8]:

$$n\lambda = 2\ d\ sin\theta \tag{9}$$

where, θ is the incidence angle, d is the lattice spacing, n is the diffraction order and λ is the beam wavelength. When a crystal is exposed to X-ray, the resulting diffraction pattern reveals multiple reflections, which can be transformed into a model of the crystal's electron density through Fourier transformation.

In this thesis, powder XRD was used to characterize the neat pectin and pectin crosslinked with the three agents. Diffractograms where analyzed to calculate the degree of crystallinity and the d-spacing. Philips X'pert PRO automatic diffractometer using Cu-Kα radiation (λ = 1.5418 Å), with a secondary monochromator and a PIXcel solid-state detector was employed. The radiation source was operated at a generator voltage of 40 kV and a current of 40 mA. The scans were performed with a 0.026 step size in the 2θ range of 2°–80° at room temperature. The percentage crystallinity was calculated using the following formula:

$$\%\ crystallinity = \frac{crystalline\ area}{total\ area}\ 100 \tag{10}$$

4.2.7. Swelling experiments

The crosslinked pectin films were cut, accurately weighed, and placed in vials containing 100 mL of water (pH = 7). The films were agitated at room temperature and removed at certain intervals for weighing after drying the surface water filter paper. The same sample was used for each immersion time. The percentage water uptake was calculated as:

$$\text{Water uptake} = ((M_{swollen} - M_{dry})/M_{dry})\ 100 \tag{11}$$

where $M_{swollen}$ is the weight of the film after after immersion in the solution, while M_{dry} corresponds to the initial dry weight of the film. This formula was use in this thesis to calculate the swelling capacity of the films.

4.2.7. Film reusability

To evaluate the reusability of the film, successive adsorption desorption cycles were performed. For the calculation of the desorption efficiency the following formula was used:

$$Desorption\ Efficiency\ [\%] = \left(\frac{C_{des}}{C_0 - C_{eq}}\right) * \ 100 \quad (12)$$

where, C_{des} is the desorption solution concentration of the adsorbate, C_0 is the initial concentration of the adsorbate in the initial solution and C_{eq} is the concentration of the adsorbate after the adsorption.

REFERENCES

1. Koide, Y., Ikake, H., Muroga, Y. & Shimizu, S. Effect of the cast-solvent on the morphology of cast films formed with a mixture of stereoisomeric poly(lactic acids). *Polym. J.* **45**, 645–650 (2013).

2. Suhag, R., Kumar, N., Petkoska, A. T. & Upadhyay, A. Film formation and deposition methods of edible coating on food products: A review. *Food Res. Int.* **136**, 109582 (2020).

3. Ma, X., Jing, J., Wang, J., Xu, J. & Hu, Z. Extraction of Low Methoxyl Pectin from Fresh Sunflower Heads by Subcritical Water Extraction. *ACS Omega* **5**, 15095–15104 (2020).

4. Berthomieu, C. & Hienerwadel, R. Fourier transform infrared (FTIR) spectroscopy. *Photosynth. Res.* **101**, 157–170 (2009).

5. Synytsya, A., Čopíková, J., Matějka, P. & Machovič, V. Fourier transform Raman and infrared spectroscopy of pectins. *Carbohydr. Polym.* **54**, 97–106 (2003).

6. Filippov, M., Shkolenko, G. A. & Kohn, R. Determination of the esterification degree of the pectin of different origin and composition by the method of infrared spectroscopy. in (2013).

7. MANNING, T. J. & GROW, W. R. Inductively Coupled Plasma - Atomic Emission Spectrometry. *Chem. Educ.* **2**, 1–19 (1997).

8. Aslam, A. *et al.* Study of structural, optical and electrical properties of La3+doped Mg0.25 Ni0.15 Cu0.25 Co0.35 Fe2-x Lax O4 spinel ferrites. *Phys. B Condens. Matter* **602**, 412565 (2021).

Chapter 5

Crosslinking of pectin films – structure

This chapter focuses on the comprehensive analysis of synthesized pectin-based adsorbents. The investigation includes monitoring and characterizing crosslink reactions of pectin films through batch adsorption experiments, employing ICP-AES for precise measurements. We will first discuss the crosslinking with calcium, and after that, we will use europium alone and a combination of calcium and europium as crosslinkers. The resulting kinetic and isotherm data will be analyzed using various models to gain deeper insights. Furthermore, the morphology and presence of crosslinkers will be examined using SEM and EDX techniques. The structural properties of the generated materials will be evaluated through XRD and FT-IR analysis. Additionally, the swelling capacities of the films, a vital feature of their effectiveness as adsorbents, will be thoroughly assessed. This extensive analysis will explain the structure of the pectin-based adsorbent's properties.

5.1. Crosslink reactions

5.1.1. Isotherms

The crosslink reactions on pectin were thoroughly analyzed by investigating their adsorption isotherms. In this study, LM pectin was crosslinked using three distinct agents: calcium, europium, and a double crosslinking approach comprising calcium and europium. LM pectin was initially crosslinked with calcium, followed by europium crosslinking. It is important to note that all three systems were crosslinked under identical conditions, as detailed in the section number 4.1.2. 'Pectin-Based Film Crosslinking' in the materials and methods (Chapter 4).

Consequently, the resulting films were given specific designations based on the crosslinking agent utilized for each film, namely P-Ca^{2+}, P-Eu^{3+}, and P-Ca^{2+}-Eu^{3+}. This detailed characterization comprehensively explains of the different crosslinking variations and their respective effects on the pectin matrix.

According to the data presented in Fig. 5.1 and Table 5.1., the maximum adsorption capacity of pectin for calcium is approximately 21 mg/g, while for europium is 56 mg/g. However, when pectin was crosslinked with calcium before europium, the adsorption capacity of Eu^{3+} significantly increased to 140 mg/g. This indicates that the ability of pectin to adsorb europium after dual-crosslinking with calcium was more than twice as compared to single europium crosslinks. Hence, it can be concluded that the dual-crosslinking system effectively enhances the adsorption of europium on pectin films.

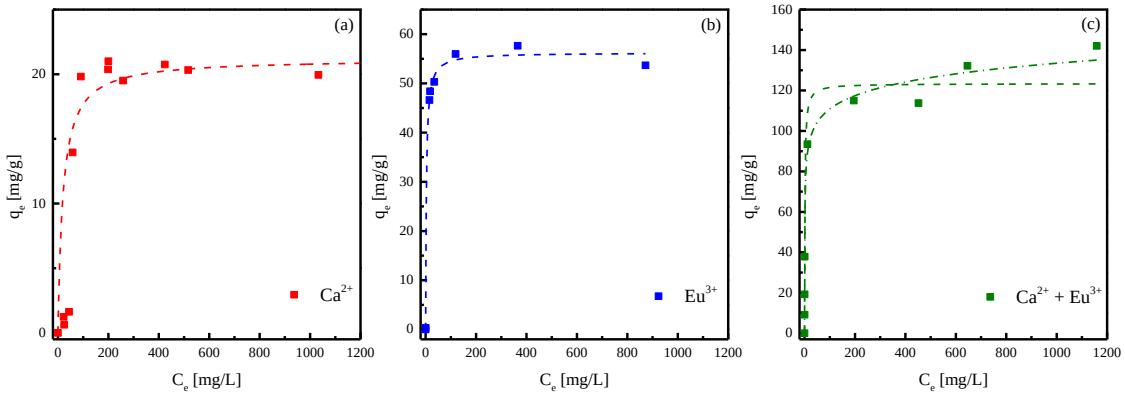

Figure 5.1. Adsorption isotherms of pectin films (at a dose of 2.5 g/L) at pH=7 using calcium (a), europium (b), and a combination of calcium and europium (c) as the crosslinking agents. The dashed lines represent the nonlinear fittings obtained using the Langmuir model, while the dotted-dashed lines represent the nonlinear fittings obtained using the Redlich-Peterson model.

The adsorption isotherms of pectin crosslinked with calcium or europium were analyzed using the Langmuir isotherm model, as shown in Table 1. This model assumes that adsorption occurs at identical sites, allowing only one molecule to be adsorbed at each location [1,2]. However, in the case of the pectin sample crosslinked with the dual system, the Langmuir isotherm model exhibited poorer fit (R^2 = 0.96) than the Redlich-Peterson model (R^2= 0.99), which also was employed [3]. This suggests that the dual-crosslinking system does not exhibit an ideal monolayer adsorption behavior. The adsorption sites can be either homogeneous or heterogeneous, indicating structural differences[4] between samples crosslinked with calcium or europium alone and those crosslinked with both Ca^{2+} and Eu^{3+}.

Regarding the fitting parameters, the K_L and K_{RP} values suggest a favorable interaction between the adsorbate and adsorbent. The parameter α plays a crucial role in shaping the isotherm curve. As α approaches zero, the isotherm exhibits a linear trend, signifying adherence to the

Langmuir isotherm model. Conversely, as α rises, the isotherm increasingly deviates from linearity, pointing towards pronounced deviations from Langmuir behavior. The obtained value for the parameter α was 1.78 ± 0.64 mg/L, indicating a slight departure from Langmuir behavior and suggesting a subtle presence of heterogeneous adsorption. On the other hand, the β parameter, ranging from 0 to 1, represents the surface heterogeneity where the adsorbate interacts. A value closer to zero signifies a more heterogeneous surface, yet the determined value for β was 0.92 ± 0.02, suggesting a predominantly homogeneous adsorption surface.

Table 5.1. The Langmuir and Redlich-Peterson adsorption isotherm models were employed to estimate parameters for the three cations in pectin films. The maximum binding capacity, $q_{M,}$ is expressed in mg/g.

Sample	Model	R^2_{adj}	K_L [L/mg]	K_{RP} [L/mg]	q_{Max} [mg/g]
P–Ca^{2+}	Langmuir	0.99	0.050 ± 0.032	---	21.2 ± 0.6
P–Eu^{3+}	Langmuir	0.99	0.32 ± 0.06	---	56.2 ± 0.9
P–Ca^{2+}-Eu^{3+}	Langmuir	0.96	0.65 ± 0.26	---	123.4 ± 5.4
P–Ca^{2+}-Eu^{3+}	Redlich–Peterson	0.99	---	139.2 ± 39.7	

5.1.2. Kinetics

The crosslink reaction was also analyzed using the adsorption kinetic curves for each crosslinking agent.

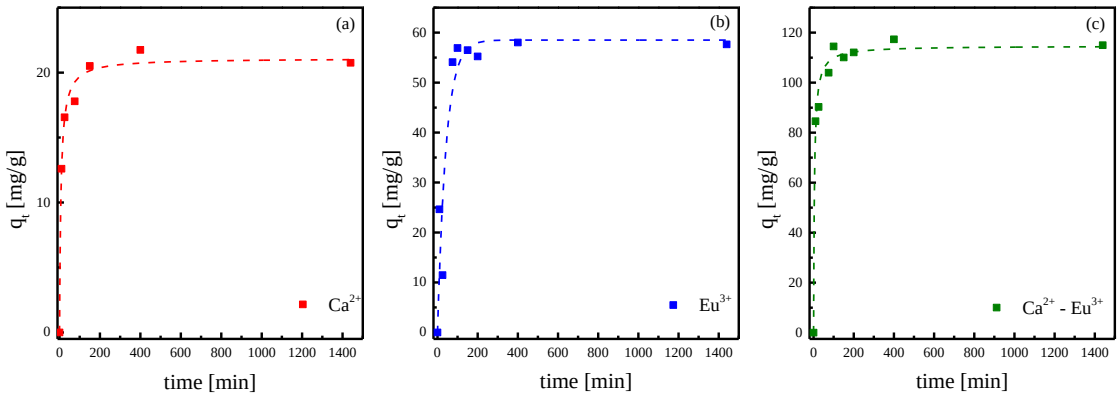

Figure 5.2. Depiction of the adsorption kinetics of pectin films (at a dose of 2.5 g/L) using calcium (a), europium (b), and a combination of calcium and europium (c) as crosslinking agents at pH = 7. The dashed lines represent the nonlinear fittings obtained through the implementation of the PSO and PFO models.

The adsorption isotherms demonstrate that the dual-crosslinking system exhibited a significantly higher uptake of europium compared to the system with europium alone. The data highlights the superior adsorption performance achieved through the dual-crosslinking approach.

To determine the appropriate kinetic model (PFO or PSO) and gain insights into the ion adsorption mechanism, we employed three criteria: the R^2_{adj} value obtained from nonlinear fitting, Akaike´s information criterion (AIC), and Bayesian information criterion (BIC)[5]. The results showed that the crosslinking reactions of pectin with calcium and the dual system were best described by the PSO model, indicating a chemisorption-driven adsorption process[6]. In contrast, the crosslinking reaction with europium exhibited the best fit using the PFO model, suggesting that the adsorption process was primarily governed by electrostatic interactions or physisorption rather than chemisorption [7,8]. The fitting results are illustrated in Fig. 5.2. and summarized in Table 5.2. Therefore, it can be concluded that the samples crosslinked with calcium and the dual system (calcium and europium) exhibited stronger interactions between the ions and pectin compared to those crosslinked solely with Eu^{3+}.

The rate constants K_1 and K_2, derived from the PFO and PSO kinetic models, respectively, offer insights into the speed or rate of the adsorption process. A higher value of K_1/K_2 indicates a faster rate of adsorption, while a lower value suggests a slower rate. In our study, we observed that the adsorption proceeded most rapidly with P-Eu^{3+}, followed by P-Ca^{2+}-Eu^{3+}, and finally P-Ca^{2+}, exhibiting respective values of 0.024 L/min, 0.0064 g/mg min, and 0.002 g/mg min for the rate constants.

Table 5.2. Parameters estimated for the three cations of pectin films modeled using adsorption kinetics models.

Sample	**Model**	R^2_{adj}	K_1 **[L/min]**	K_2 **[g/(mg min)]**	q_{eq} **[mg/g]**
P–Ca^{2+}	PSO	0.99	----	0.0064 ± 0.0013	21.1 ± 0.5
P-Eu^{3+}	PFO	0.89	0.024 ± 0.007	----	58.5 ± 4.0
P–Ca^{2+}-Eu^{3+}	PSO	0.99	----	0.0020 ± 0.0004	114.7 ± 2.1

5.2. Morphology

The SEM images in Figures 5.3.a–d present a visual comparison of untreated and crosslinked pectin, revealing noticeable morphological changes that occur following crosslinking with the three agents. P-Ca^{2+} exhibited a homogeneous size with a spherical granular shape, while P-Eu^{3+} displayed a granular surface with a distinct preferential orientation. On the other hand, P-Ca+Eu showed a more consistently uniform surface than the untreated pectin.

The EDX spectra in Figure 3 confirm the presence of either calcium or europium in all crosslinked samples. Notably, the EDX spectrum of the untreated pectin (Fig. 5.3.a) revealed the presence of Na^+, which additionally facilitated the reticulation reaction[9]. Upon crosslinking with Ca^{2+} (Fig. 5.3.b) or Ca^{2+} and Eu^{3+} (Fig. 5.3.d), a distinct peak emerged at 3.70 keV, indicating the presence of Ca^{2+}. Similarly, after crosslinking with Eu (Fig. 5.3.c) or Ca^{2+} and Eu^{3+} (Fig. 5.3.d), two distinct peaks associated with Eu^{3+} were observed at 1.13 and 5.8 keV. These peaks served as definitive evidence for the occurrence of crosslinking in all three cases. Notably, the EDX spectra exhibited consistent patterns throughout the samples, suggesting a homogeneous dispersion of calcium, europium, or both without significant variations across different sections.

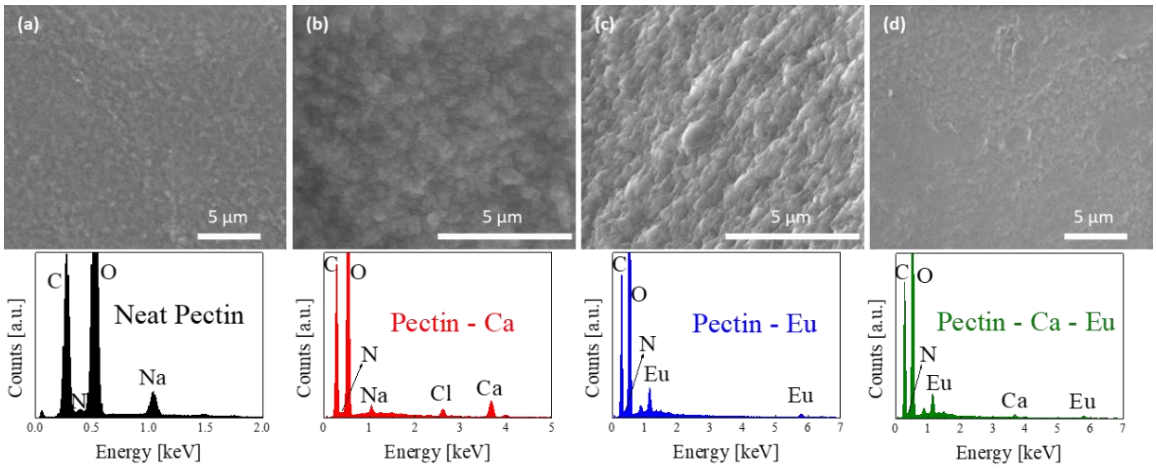

Figure 5.3. Scanning electronic microscopy images and EDX spectra of pectin-based films with (a) neat pectin and pectin samples crosslinked with (b) Ca, (c) Eu, and (d) Ca+Eu. Fig. S2 shows images of the regions used for EDX mapping.

5.3. Structural properties of different crosslinked pectin-based adsorbents

In this section, we will delve into an extensive analysis of the structural properties exhibited by the three crosslinked samples. To evaluate and discern the structural disparities among the crosslinking agents, Figure 5.4 shows the infrared spectra of both the untreated and crosslinked pectin samples. Within the spectra, a highly prominent band emerges within the range of approximately 3600–3000 cm^{-1}, corresponding to the stretching vibrations of hydroxyl groups (–OH). Simultaneously, distinct bands manifest within the 3000–2850 cm^{-1} range, signifying the vibrations of methyl groups ($–CH_3$). Further examination reveals a conspicuous peak at around 1725 cm^{-1}, attributing to the C=O stretching of nonionic carboxyl groups (–COOH, $–COOCH_3$). Additionally, an assigned peak at approximately 1610 cm^{-1} corresponds to the asymmetric

stretching vibrations of carboxylate anions (COO^-)[10,11]. These detailed structural analyses provide valuable insights into the differing characteristics imparted by the various crosslinking agents.

An in-depth analysis of the structural changes induced by crosslinking reveals the most significant alterations in the carboxylate anion band (~1600 cm^{-1}). Specifically, the band at 1591 cm^{-1} in the untreated pectin experienced a blueshift to 1598 cm^{-1} upon crosslinking, a phenomenon previously reported[9]. This blueshift to higher wavenumbers arises from the strong interaction between calcium ions and the ionized carboxyl group. However, in the case of dual crosslinking, a slight redshift was observed, with the band shifting to 1590 cm^{-1}, while in the case of Eu^{3+} crosslinking, the shift was more pronounced, reaching 1583 cm^{-1}. This disparity suggests that, unlike calcium ions, europium ions exhibit a weaker interaction with the ionized carboxylate group, which becomes particularly evident in the case of europium alone.

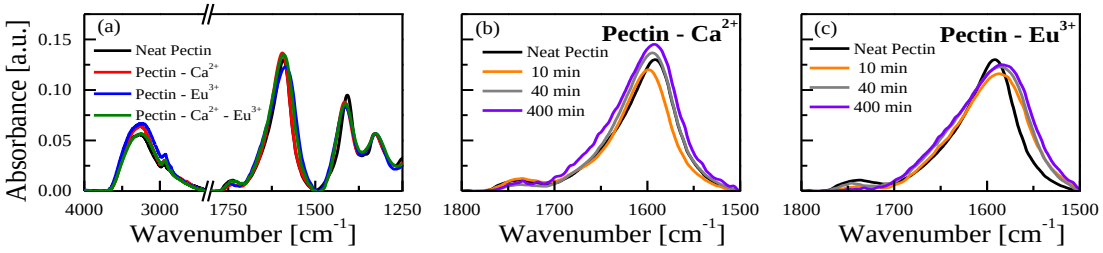

Figure 5.4. Infrared spectra of (a) neat and crosslinked pectin using three different crosslinking agents and (b) P–Ca and (c) P–Eu films crosslinked for different durations (10, 40, and 400 min).

To validate this finding, we conducted separate crosslinking experiments using calcium and europium with pectin at different durations (10, 40, and 400 min). As depicted in Figures 4b and c, even within the initial minutes of the crosslinking reaction, the weaker interaction between europium ions and the ionized carboxylate group is apparent (Figure 5.4(c)). This observation challenges the notion of the formation of an "egg-box" structure when pectin is crosslinked with europium, suggesting a distinct mechanism at play.

These comprehensive analyses provide valuable insights into the intricate interplay between crosslinking agents and pectin, emphasizing the distinct behaviors of calcium and europium ions when interacting with the ionized carboxylate groups.

The XRD patterns presented in Figure 5.5 offers further extensive insights into the structural characteristics of each crosslinking system within the pectin films. Specifically, these XRD patterns serve as a valuable tool for discerning the presence and properties of the amorphous and crystalline phases in the respective materials[12]. Examining the XRD pattern of the neat pectin

film, distinct and well-defined crystalline peaks emerged prominently at 2θ values of 12.6°, 22.6°, and 33.8°, serving as precise indicators of a high degree of crystallinity (refer to the fitting procedure in Figure 5.5 (b) for detailed analysis). Concurrently, the XRD analysis revealed the existence of amorphous halos observable at 2θ values of 31° and 41.9°, manifesting as less distinct XRD patterns and signifying the presence of the amorphous fraction within the neat pectin film. Moreover, through careful examination of the most intense diffraction peak, a characteristic d-spacing of 0.70 nm was ascertained for the neat pectin film, aligning with prior research findings and supporting existing reports[13].

Upon crosslinking with calcium, noticeable changes in the XRD patterns became apparent, showcasing deviations from the crystalline properties of the neat pectin film. Specifically, the diffraction peaks observed after calcium crosslinking appeared broader than those of the neat pectin film, signifying a reduced degree of crystallinity in the crosslinked structure. However, distinct peaks persisted at 2θ values of 14°, 23.7°, and 27.0°, accompanied by amorphous halos discernible at 2θ values of 30° and 40°. Analyzing the most prominent diffraction peak, a typical d-spacing of 0.63 nm was derived for the calcium-crosslinked pectin film, indicating a notable alteration in the lateral spacing between pectin chains compared to the untreated sample (0.70 nm). This XRD pattern aligns with previous studies on polymer chain dimerization through calcium coordination, as elucidated by the egg-box model[14]. Initially, a 2/1 helical conformation was proposed[15], but subsequent investigations revised this to a 3/1 helical conformation[13] concerning the junction zones. These findings provide substantial evidence regarding the structural changes induced by calcium crosslinking and shed light on the underlying mechanisms associated with the modified pectin network.

The dual-crosslinked sample (calcium and europium) exhibited an even more significant reduction in crystallinity compared to the calcium crosslinked sample, as evidenced by the broader diffraction peaks. Despite the decreased crystallinity, distinct peaks were still discernible at 2θ values of 14.5° and 21.0°, accompanied by broader peaks at 2θ values of 26° and 41°. Calculating the typical d-spacing based on the diffraction peak at 14.5° resulted in a value of 0.61 nm. Thus, a systematic decrease in the interlayer distance was observed across the neat pectin, P-Ca^{2+}, and P-Ca^{2+}-Eu^{3+} samples, accompanied by broader and less intense peaks. Employing the integration method, we estimated the crystallization percentages to be 34%, 21%, and 15% for the neat pectin, calcium crosslinked, and calcium and europium crosslinked samples, respectively. These findings indicate that introducing Eu^{3+} led to a significant reduction in the crystalline phase, with a gradual amorphization of the pectin material as the crosslinking transitioned from Ca^{2+} to Ca^{2+} and Eu^{3+}. This comprehensive analysis sheds light on the progressive changes in the crystalline structure induced by the incorporation of europium in the crosslinking process, emphasizing the impact of dual-crosslinking on the overall crystallinity of the pectin network.

By contrast, upon crosslinking pectin with Eu^{3+} alone, the XRD pattern exhibited solely amorphous halos at 2θ values of 21° and 42°, signifying the absence of well-defined crystals or, at best, highly defective ones. Moreover, the crystalline fraction was eliminated, leaving no trace of crystallinity. As a result, the crosslinking process involving Eu^{3+} alone induced a thorough amorphization of the pectin material, rendering it devoid of any indications of the characteristic "egg-box" model typically associated with crosslinking. The loss of crystalline structure observed in this case further emphasizes the distinctive influence of europium as a crosslinking agent, leading to a complete transformation of the pectin's molecular arrangement into an amorphous state.

In the absence of divalent cations, pure pectin chains primarily interact through hydrogen bonding[16]. However, in the presence of Ca^{2+} ions, a more complex interaction mechanism occurs. The carboxyl groups of different pectin chains form noncovalent calcium bridges, leading to dimerization[17], while the hydrogen bonds within the network also contribute to the overall structure[18]. These findings are consistent with the observations from FT-IR and XRD analyses. Introducing Eu^{3+} atoms into the P-Ca^{2+} lattice, produces defects in the periodic network, resulting in a loss of crystallinity and a diminished interaction between carboxylate groups. However, it remains uncertain whether the entry of Eu^{3+} solely disrupts the periodicity or completely

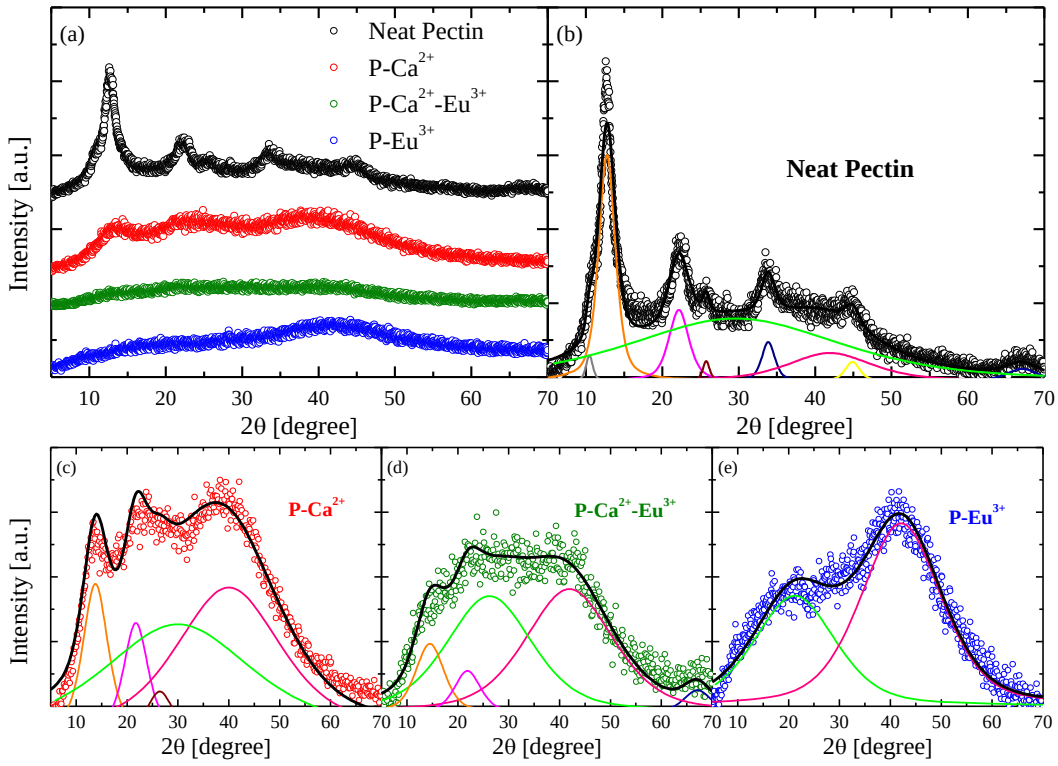

Figure 5.5. (a) Comparison of the XRD patterns of pectin adsorbents crosslinked by differnt agents. (b–d) XRD patterns of neat and crosslinked pectin films. Experimental data are indicated by points, and fittings of the experimental data with the pseudo Voigt profiles are indicated by solid lines.

dismantles the "egg-box" structure in this particular sample. Further investigation is needed to elucidate the exact nature of the structural changes induced by introducing europium into the network.

To gain further insights, we conducted ICP-AES experiments to investigate the release of Ca^{2+} ions upon crosslinking with Eu^{3+}. After crosslinking pectin with Ca^{2+}, the P-Ca^{2+} films underwent extensive washing procedures (100 mL of water, agitated for 1 hour, repeated five times). Each wash cycle's water was analyzed using ICP to determine the presence of released Ca^{2+} ions, indicating their detachment from the pectin chains. Additionally, we aimed to explore the possible ion exchange between calcium and europium in the dual-crosslinking system.

Specifically, we wanted to determine if, during Eu^{3+} crosslinking, some Ca^{2+} ions were displaced from the sample. The findings revealed that, during Eu^{3+} crosslinking, nearly 70% of the Ca^{2+} ions were released. This indicates that Eu^{3+} played a significant role in dismantling the "egg-box" structure, leading to the loss of a substantial portion of the bound Ca^{2+} ions. For instance, when considering P-Ca^{2+} crosslinked for 40 minutes, the Ca^{2+} uptake was measured at 2.69×10^{-5} mol, while during Eu^{3+} crosslinking, the sample released 1.77×10^{-5} mol Ca^{2+}. These results demonstrate that the sample experienced a 67% reduction in the concentration of calcium ions due to the crosslink with europium.

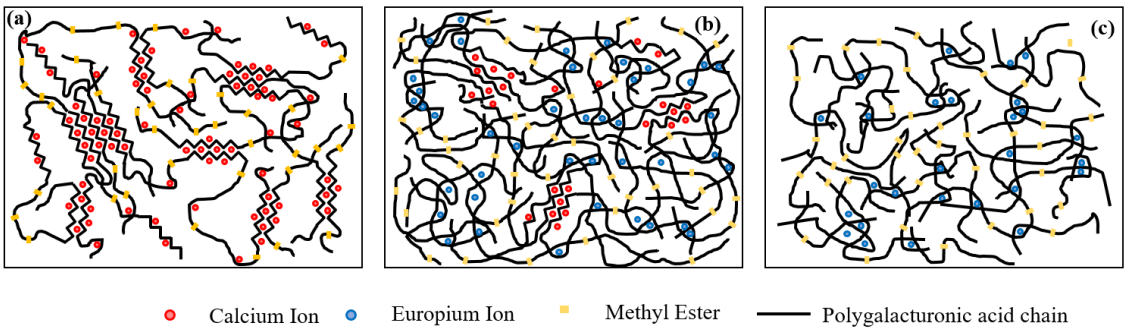

Figure 5.6. Illustrations depicting three crosslinked systems: (a) P-Ca^{2+} (a), (b) P-Ca^{2+}-Eu^{3+}, and (c) P-Eu^{3+}.

The sample crosslinked solely with Eu^{3+} exhibited a complete loss of crystallinity, indicating a fully amorphous structure characterized by reduced interaction between the carboxyl groups. The established crosslinks in this system could involve localized interactions between two or three chains, allowing for the formation of a stable three-dimensional network. Fig. 5.6. provides schematic representations of the expected structures of pectin using the three different crosslinking agents, drawing insights from the SEM, XRD, and FT-IR findings. For P-Ca^{2+}, we anticipated an egg-box model where each Ca^{2+} ion is associated with two carboxyl groups, as depicted in Fig. 5.6.a. In contrast, Eu^{3+}-induced crosslinking resulted in an amorphous network

with random crosslinking points, as illustrated in Fig. 5.6.c. Finally, the dual-crosslinked sample containing both Eu^{3+} and Ca^{2+} exhibited a combination of crystalline and amorphous phases, as represented in Fig. 5.6.b.

5.4. Swelling of pectin based adsorbents

The distinct structural characteristics of the various crosslinking systems also significantly affected the swelling properties, as demonstrated in Fig. 5.7. This property holds relevance in water treatment applications, as pollutants need to diffuse into the matrix to reach the adsorption sites. Considering that swelling behavior is influenced by sample size, all measurements were performed on samples with similar dimensions (specifically, thicknesses of 0.154 ± 0.031 mm, 0.157 ± 0.015 mm, and 0.141 ± 0.024 mm for P-Ca^{2+}, P-Eu^{3+}, and P-Ca^{2+}-Eu^{3+}, respectively). These controlled sample dimensions ensured consistency and comparability in assessing the swelling properties among the different crosslinked systems.

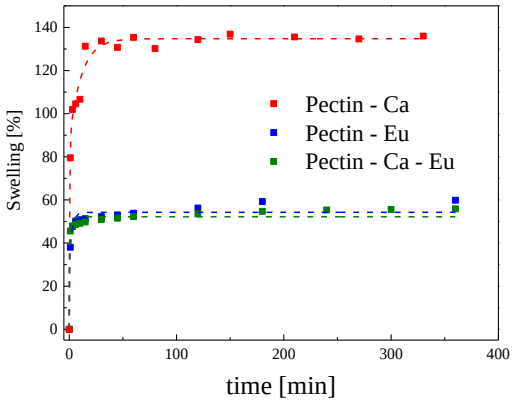

Figure 5.7. Swelling properties of P-Ca^{2+},P- Eu^{3+}, and P-Ca^{2+}-Eu^{3+}.

The equilibrium water uptake behavior of the crosslinked films varied among the different systems. The P-Ca^{2+} films required approximately 2 hours to reach water uptake equilibrium, whereas the P-Eu^{3+} and P-Ca^{2+}-Eu^{3+} films achieved equilibrium much faster, within just 15 minutes. Notably, the P-Ca^{2+} film exhibited the highest swelling, indicating a greater affinity for water compared to the P-Eu^{3+} and P-Ca^{2+}-Eu^{3+} films. This observation suggests that the calcium crosslinked pectin possessed a larger number of available hydroxyl, carboxyl, and carboxylate groups, which facilitated the establishment of hydrogen bonds with water molecules, compared to the Eu^{3+} and Ca^{2+}-Eu^{3+} films. Consequently, we can infer indirectly that Eu^{3+} ions have a higher propensity to interact with hydroxyl, carboxyl, and carboxylate groups than Ca^{2+} ions.

5.5. Conclusions

In this chapter, we studied the crosslinking of pectin with different agents. First, we explore the well-known crosslinking of low DM pectin by calcium. After that, we propose crosslinking pectin with europium and a combination of calcium + europium.

We determined the ion content in each sample by studying the crosslinking reaction through kinetic and isotherm adsorption experiments. These results demonstrated that the sample crosslinked with Ca^{2+}+Eu^{3+} ions could capture more europium than the sample crosslinked with Eu^{3+}alone. This is because the second crosslink with Europium removes around 70% of the calcium ions.

Regarding the structural changes of the three reticulated pectins, we observed critical differences in the carboxylate anion band measured by infrared spectroscopy (1610 cm-1). Unlike calcium, the Eu^{3+} ions interact less with the ionized carboxylate group, which is most noticeable in the case of the crosslink produced by Eu^{3+} alone. This suggests that it is difficult to rationalize the formation of an “egg-box” structure when pectin is crosslinked with Eu^{3+}.

To study these structural differences we analyze the XRD response of the three-crosslinked samples. We estimated a gradual decrease in the crystallization percentage from 21 to 15% for Ca^{2+}, and Ca^{2+}+Eu^{3+} reticulated samples, respectively. Moreover, for the pectin crosslinked with Europium alone, we cannot detect any crystallinity. This indicates that Europiium crosslinking causes a progressive amorphization of the pectin material.

Thus, we showed that Eu^{3+} crosslinking did not form the same structure as with calcium crosslinking, being a sample with a complete amorphization as compared with the calcium crosslinking.

REFERENCES

1. Wang, J. & Guo, X. Adsorption isotherm models: Classification, physical meaning, application and solving method. *Chemosphere* **258**, 127279 (2020).

2. Wang, J. & Guo, X. Adsorption kinetic models: Physical meanings, applications, and solving methods. *J. Hazard. Mater.* **390**, (2020).

3. Liu, Q.-S., Zheng, T., Wang, P., Jiang, J.-P. & Li, N. Adsorption isotherm, kinetic and mechanism studies of some substituted phenols on activated carbon fibers. *Chem. Eng. J.* **157**, 348–356 (2010).

4. Foo, K. Y. & Hameed, B. H. Insights into the modeling of adsorption isotherm systems. *Chem. Eng. J.* **156**, 2–10 (2010).

5. Vareda, J. P. On validity, physical meaning, mechanism insights and regression of adsorption kinetic models. *J. Mol. Liq.* **376**, 121416 (2023).

6. Sivagangi Reddy, N., Madhusudana Rao, K., Sudha Vani, T. J., Krishna Rao, K. S. V & Lee, Y. I. Pectin/poly(acrylamide-co-acrylamidoglycolic acid) pH sensitive semi-IPN hydrogels: selective removal of Cu2+ and Ni2+, modeling, and kinetic studies. *Desalin. Water Treat.* **57**, 6503–6514 (2016).

7. Huda, M. N., Li, W., Dai, M. & Lin, L. Kinetic Study on Mercury Sorption from Fuel Gas. *Energy & Fuels* **31**, 1820–1824 (2017).

8. Bhuyan, M. M., Okabe, H., Hidaka, Y. & Hara, K. Pectin-[(3-acrylamidopropyl) trimethylammonium chloride-co-acrylic acid] hydrogel prepared by gamma radiation and selectively silver (Ag) metal adsorption. *J. Appl. Polym. Sci.* **135**, 45906 (2018).

9. Assifaoui, A., Loupiac, C., Chambin, O. & Cayot, P. Structure of calcium and zinc pectinate films investigated by FTIR spectroscopy. *Carbohydr. Res.* **345**, 929–933 (2010).

10. Balaria, A. & Schiewer, S. Assessment of biosorption mechanism for Pb binding by citrus pectin. *Sep. Purif. Technol.* **63**, 577–581 (2008).

11. Veisi, Z., Gallant, N. D., Alcantar, N. A. & Toomey, R. G. Responsive coatings from naturally occurring pectin polysaccharides. *Colloids Surfaces B Biointerfaces* **176**, 387–393 (2019).

12. Murthy, N. S. & Minor, H. General procedure for evaluating amorphous scattering and

crystallinity from X-ray diffraction scans of semicrystalline polymers. *Polymer (Guildf).* **31**, 996–1002 (1990).

13. Li, L., Fang, Y., Vreeker, R., Appelqvist, I. & Mendes, E. Reexamining the Egg-Box Model in Calcium−Alginate Gels with X-ray Diffraction. *Biomacromolecules* **8**, 464–468 (2007).

14. Walkinshaw, M. D. & Arnott, S. Conformations and interactions of pectins: II. Models for junction zones in pectinic acid and calcium pectate gels. *J. Mol. Biol.* **153**, 1075–1085 (1981).

15. Mackie, W. Conformations of crystalline alginic acids and their salts. *Biochem. J.* **125**, 89P (1971).

16. Braccini, I. & Pérez, S. Molecular Basis of Ca2+-Induced Gelation in Alginates and Pectins: The Egg-Box Model Revisited. *Biomacromolecules* **2**, 1089–1096 (2001).

17. Powell, D. A., Morris, E. R., Gidley, M. J. & Rees, D. A. Conformations and interactions of pectins: II. Influence of residue sequence on chain association in calcium pectate gels. *J. Mol. Biol.* **155**, 517–531 (1982).

18. Li, D. *et al.* Pectin in biomedical and drug delivery applications: A review. *Int. J. Biol. Macromol.* **185**, 49–65 (2021).

Chapter 6

Remediation of water by crosslinked pectin with Ca^{2+}

This chapter focuses on water remediation using calcium crosslinked pectin. As mentioned in the introduction (see Table 2 from Chapter 3), this material was used in the literature to remediate water from heavy. However, pectin crosslinked with calcium was not used as an adsorbent for other contaminants such as pharmaceuticals. In this chapter, we initially examined pectin with varying methyl esterification degrees (D.M) and assessed their barium adsorption capabilities. Once the appropriate D.M. was identified, we conducted SEM-EDX analysis to characterize the pectin structure. Subsequently, we investigated the impact of pH, adsorbent dos¡e, and initial concentration (C_0) on barium adsorption through batch adsorption experiments involving isotherms and kinetics. In addition, we assessed the reusability of the P-Ca^{2+} film. Finally, we also prove that pectin-calcium crosslinked pectin can be used to remediate pharmaceuticals, as we showed here for chlorpheniramine maleate. This opens a new route to develop pectin-based adsorbents.

6.1. Influence of the Degree of Methylesterification of pectin on water remediation capabilities

6.1.1. Degree of esterification calculation (FT-IR)

To assess the impact of the degree of methyl esterification (D.M.) [%] on the water remediation capabilities of pectin-based adsorbents, we obtained four commercial pectins from Hebstreith and Fox (H&F) with varying D.M. values. The reported D.M. values provided by the supplier were as follows: 9.9%, 40%, 50%, and 70%.

To begin, films were produced using each variant of pectin, and the D.M. for each sample was determined through an experimental calculation using FT-IR analysis. It is well-known that the D.M. of pectins tends to decrease over time[1], thus by employing this approach, we can ascertain the current D.E. values for the pectin samples under investigation.

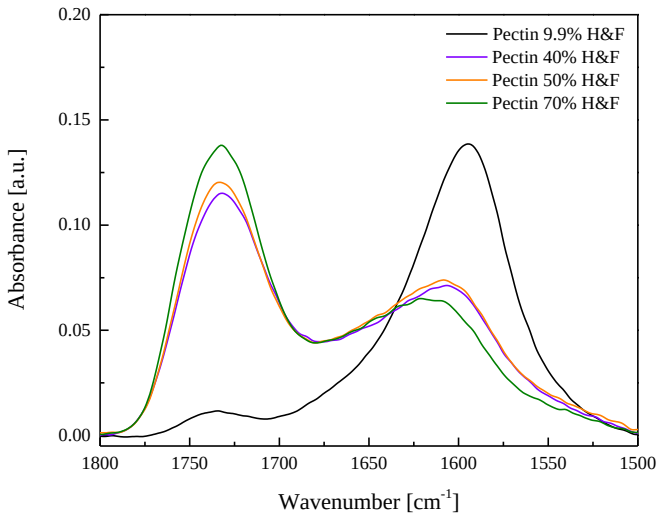

Figure 6.1. FT-IR spectra of pectin with different D.M..

The D.M. was determined by analyzing the peak areas associated with the deprotonated carboxyl group (COO^-) at 1630 cm^{-1} and the C=O group at 1735 cm^{-1}, as described in the materials and methods section on FT-IR analysis. Spectra were collected for all four pectin types (see Fig. 6.1), and the D.M. values were calculated based on the area of each peak. The results of the D.M. calculations using FT-IR can be found in Table 6.1.

Table 6.1. Calculated D.M. using FT-IR measurements

H&F Pectins	D.M [%].
H&F 9.9%	8.98
H&F 40%	55.69
H&F 50%	55.99
H&F 70%	72.01

Noticeably, the peak at the wavenumber 1630 cm^{-1}, corresponding to the -COO^{-} group, for the sample 9.9% H&F exhibits a higher intensity than the other samples. This enhanced intensity suggests a potential affinity for the uptake of Ca^{2+} and Ba^{2+} ions, given the well-known interaction between these metallic divalent cations and the functional group[2].

6.1.2. Different D.M. pectin crosslinked with Ca^{2+} and Ba^{2+} adsorption evaluation

This section aims to assess the potential of P-Ca^{2+} films for the remediation of heavy metals. Extensive research has been conducted on the interaction between pectins and divalent metallic cations, such as Ca^{2+}, Ni^{2+}, Fe^{2+}, Cd^{2+}, Cu^{2+}, Pb^{2+}, and Zn^{2+}, as documented in various studies[3–6]. However, the literature provides limited information regarding the interaction between pectin and Ba^{2+}, making it a particular focus of this study. To evaluate the adsorption capacity of the films with different D.M., we performed ICP-AES experiments to quantify the uptake of Ca^{2+} during the crosslinking process, followed by the subsequent removal of Ba^{2+} from aqueous media. The H&F 50% film was not considered for further analysis due to the significant similarity in methyl esterification content observed with the H&F 40% film, as indicated by the FT-IR analysis results in Table 6.1.

Different D.M. pectin films were crosslinked in a 500 mg/L Ca^{2+} solution with a dose of 3.4 g/L at pH = 7 for 40 minutes. The calcium uptake by the pectin films was: 2.95 mg/g, 6.68 mg/g, and 17.44 mg/g by H&F 70%, H&F 40%, and H&F 9.9%, respectively. The pectin films exhibited the following levels of calcium uptake: H&F 70% absorbed 2.95 mg/g, H&F 40% absorbed 6.68 mg/g, and H&F 9.9% film absorbed 17.44 mg/g.

The H&F 70% film did not attain sufficient crosslinking to retain its integrity in an aqueous solution. This could be attributed to the high degree of esterification, which results in a limited number of consecutive galacturonic acid residues that possess deprotonated -COO^{-} groups necessary to form a stable "egg-box" structure. A minimum of 6-20 subunits[7,8] with the abovementioned characteristics is required to establish this structure.

We still have two potential candidates for removing Ba^{2+} from water: H&F 9.9% and H&F 40% films. To assess the performance of P-Ca^{2+} films with different D.M., we conducted

experiments at pH = 7 and at a Ba^{2+} concentration of 130 mg/L. The dose of these experiments was 2.5 g/L and allowed to interact with the solution for 24 hours. Through ICP-AES measurements, we determined that the H&F 9.9% P-Ca^{2+} film exhibited an adsorption capacity of 40.6 mg/g, while the H&F 40% P-Ca^{2+} film resulted in 34.68 mg/g. Regarding removal efficiency, the H&F film eliminated 77.5% of the barium present in the 130 mg/L aqueous solution, while the H&F 40% film achieved a removal rate of 66.4%.

Considering the above results, we conclude that the most effective candidate for Ba^{2+} remediation is the H&F 9.9% pectin. From now on, references to P-Ca^{2+} films will refer specifically to those made with H&F 9.9% pectin.

6.2. SEM-EDX

SEM measurements were conducted to examine the potential modifications in surface morphology following the remediation process. Additionally, EDX measurements were performed to verify the presence of Ba^{2+} and Ca^{2+} in the films. Two P-Ca^{2+} films were soaked in Ba^{2+} 150 mg/L pH = 7 solution for 10 and 400 minutes with a dose of 2.5 g/L.

Upon analyzing the SEM images (Figure 6.2.), it is evident that both examined samples exhibit a uniformly rough surface without any noticeable distinction compared to the film before Ba^{2+} remediation (see Figure 5.3).

The results obtained from EDX analysis confirm the successful cross-linking of pectin with a D.M. of 9.9% using Ca^{2+}. The calcium content in the films was found to be 5.3% and 6.2% (Wt%) for the 10-minute and 400-minute crosslinking time, respectively. Furthermore, EDX analysis revealed the presence of Ba^{2+} in the films, with a Ba^{2+} content of 2.1% (Wt%) for the 10-minute film and 8.7% (Wt%) for the 400-minute film. The ICP-AES analysis of the remediated samples was in correspondence with the EDX results, showing a q value of 8.7 mg/g and a removal efficiency of 15.6% for the 10-minute film, and a q value of 41.6 mg/g and a removal rate of 70.3% for the 400-minute film. Thus, the EDX results corroborate the findings obtained through ICP-AES analysis.

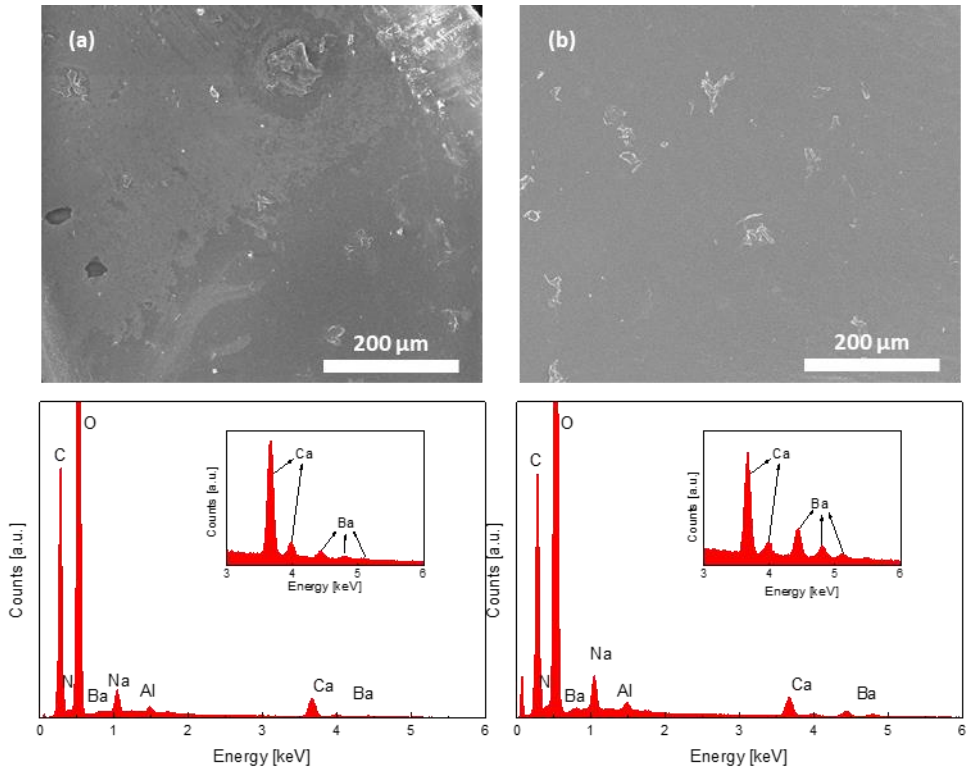

Figure 6.2. SEM images of P-Ca^{2+} after crosslinking (10 minutes) of Ba^{2+} remediation (C_o = 150 ppm) (a), after 400 minutes (b). EDX Spectra of the 10 minutes crosslinking (c) and 400 minutes (d).

6.3. Effect of pH on Ba^{2+} adsorption by P-CA^{2+} adsorbents

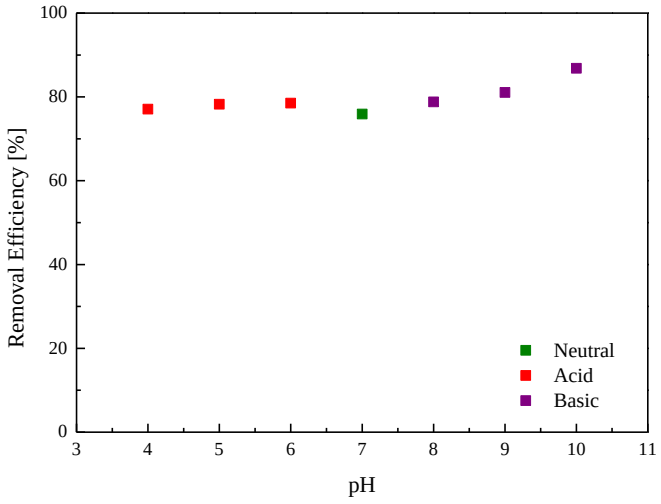

Figure 6.3. Removal efficiency [%] at 24 h of Ba^{2+} (150 mg/L = 150 ppm) using the P-Ca^{2+} adsorbent (dose 2.5 g/L) at different pH´s.

We evaluated the impact of pH on the removal efficiency of Ba^{2+} from a 150 mg/L solution using P-Ca^{2+} at a dose of 2.5 g/L for 24 hours. Interestingly, as depicted in Figure 6.3, no substantial differences were observed across different pH values. ICP-AES measurements indicated that the removal efficiency remained nearly constant at acidic pH values (pH 4: 77%, pH 5: 78%, pH 6: 78%). A slight decrease was observed at neutral pH (pH 7: 76%), while a trend of improvement was observed as the media became more alkaline (pH 8: 79%, pH 9: 81%, pH 9: 87%). Since pKa value of pectin is 3.5[9], all the COO^{-} groups are going to in the deprotonated form, which are the active binding sites for Ba^{2+} ions. This is the reason why we don´t see big differences on adsorption efficiencies between pH´s above 3.5.

Despite the lower removal efficiency at neutral pH, we focused on these conditions for several reasons. Firstly, the variations in removal efficiency among the tested pH levels were negligible. Additionally, considering that the intended application of this material is to remediate polluted water bodies, it is noteworthy that the pH of tap water typically falls within the neutral range (pH 6.5 to pH 8.5). Subsequent experimental procedures will be consistently conducted under controlled conditions at a pH of 7.

6.4. Effect of the P-Ca^{2+} dose on Ba^{2+} remediation

6.4.1. Isotherm

To gain insights into the adsorption process and assess the impact of the adsorbent dose, batch adsorption experiments were conducted to determine the isotherms of P-Ca^{2+} films on Ba^{2+} adsorption. Three different P-Ca^{2+} doses were employed: 0.5 g/L, 1 g/L, and 2.5 g/L. The Ba^{2+} solution concentrations ranged from 10 mg/L to 300 mg/L, and a contact time of 24 hours. The obtained isotherms, presented in Figure 6.4, demonstrated that the lowest dose tested (0.5 g/L) exhibited the highest maximum adsorption capacity (q_{max}) of 111.4 ± 3.9 mg/g. This was followed by the 2.5 g/L dose, which achieved a q_{max} of 87.1 ± 5.7 mg/g, and the 1 g/L dose, with a q_{max} of 81.3 ± 2.9 mg/g.

The maximum removal efficiency [%], it follows the expected trend, where the higher dose exhibits the highest removal efficiency, and as the amount of pectin decreases, the removal efficiency also decreases. The corresponding removal rates were 75.9%, 48.8%, and 34.9%, for 2.5 g/L, 1 g/L and 0.5 g/L respectively.

Table 6.2. Fitting parameters (K_L and q_{max}) of P-Ca^{2+} isotherm for Ba^{2+} remediation and maximum removal efficiencies

Isotherm parameters for P-Ca^{2+} for Ba^{2+} remediation					
Dose [g/L]	**Model**	**R^2_{adj}**	**K_L[L/mg]**	**q_{max} [mg/g]**	**Removal Efficiency [%] C_0 =150 mg/L**
2.5	Langmuir	0.97	0.025 ± 0.01	87.1 ± 5.7	75.9
1	Langmuir	0.99	0.09 ± 0.01	81.3 ± 2.9	48.8
0.5	Langmuir	0.99	0.0035 ± 0.0044	111.4 ± 3.9	34.9

All adsorption isotherms, regardless of the dose applied, were well fitted by the Langmuir isotherm model (see Table 6.2.), giving insights about the adsorption mechanism; the adsorption takes place in constant adsorption sites, in a monolayer and without interaction between adsorbed molecules, i.e., each molecule is independently adsorbed. Based on the Langmuir constant (K_L), the sample with a dose of 1 g/L reaches the maximum adsorption capacity more quickly, as it has the highest K_L value. The sample with a dosage of 2.5 g/L follows closely behind, while the sample with a dosage of 0.5 g/L lags behind in terms of reaching q_{max}.

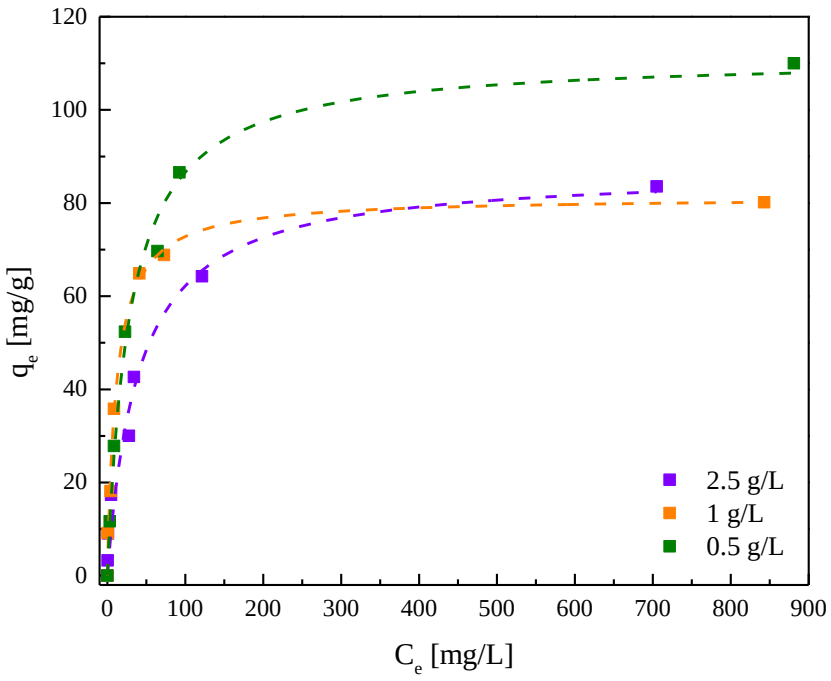

Figure 6.4. Effect of different doses (0.5, 1 and 2.5 g/L) of P-Ca^{2+} films on Ba^{2+} adsorption isotherms. Dashed lines represent Langmuir isotherm fit.

6.4.2. Kinetics

In the kinetic batch experiments, all three doses were tested using a Ba^{2+} concentration of 150 mg/L for 10 to 1440 minutes (see Figure 6.5 (a)). The most suitable model that accurately represents the experimental data is the pseudo-first-order kinetic model (PFO). The equilibrium adsorption capacity, as shown in Table 6.3, was highest for the 0.5 g/L sample, followed by the 1 g/L sample, and finally, the 2.5 g/L sample, with values of 97.8 ± 9.1 mg/g, 64.3 ± 2.3 mg/g, and 41.2 ± 0.8 mg/g, respectively. The removal efficiencies (see Figure 6.5.(b)) followed a different trend, with the highest efficiency observed for the 2.5 g/L dose, followed by the 1 g/L dose, and the lowest efficiency observed for the 0.5 g/L dose, with values of 75.5%, 43.4%, and 29.3%, respectively.

Table 6.3. Adsorption kinetic parameters for Ba^{2+} removal by 2.5, 1, and 0.5 g/l P-Ca^{2+} dosages

Kinetic parameters for P-Ca^{2+} for Ba^{2+} remediation					
Dose [g/L]	**Model**	**R^2_{adj}**	**K_1[min^{-1}]**	**q_{eq} [mg/g]**	**R [%]**
2.5	PFO	0.99	0.019 ± 0.002	41.24 ± 0.78	75.48
1 g/L	PFO	0.98	0.0093 ± 0.0012	64.26 ± 2.29	43.41
0.5 g/L	PFO	0.98	0.0017 ± 0.0005	97.81 ± 9.11	29.31

The model parameter K_1 (see Table 6.3) offers insights into the rate at which the adsorption process unfolds. Higher values of K_1 indicate faster adsorption rates, whereas lower values suggest slower adsorption rates. In this particular case, it is observed that higher dosages lead to more rapid adsorption. Specifically, the values of K_1 are 0.019, 0.0093, and 0.0017 min^{-1} for doses of 2.5, 1, and 0.5, respectively.

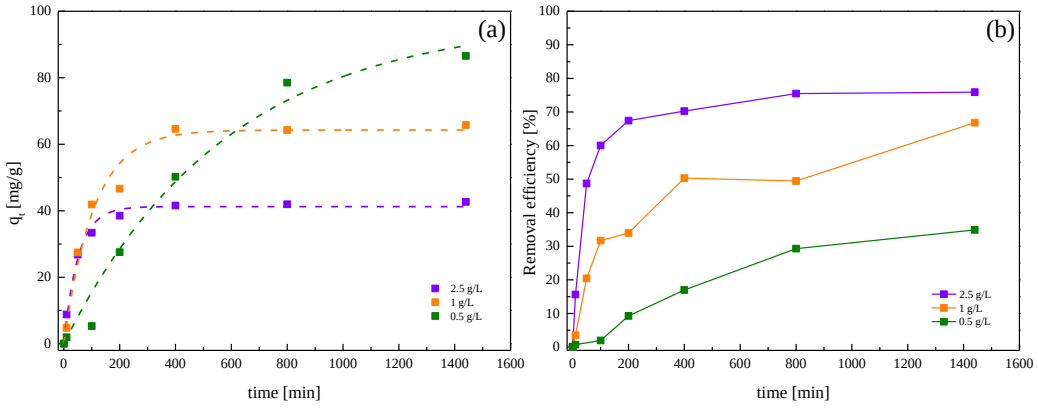

Figure 6.5. (a) Adsorption kinetic curves C_0 = 150 mg/L Ba^{2+}. Dashed lines corresponds to PFO model fit and (b) Removal rate against soaking time.

The optimal dose for achieving high removal efficiency is 2.5 g/L. 75.5% of the barium content in a 150 mg/L solution can be removed at this dose. Considering that polluted water bodies typically contain much lower concentrations of Ba^{2+}, we decided to further investigate the effectiveness of P-Ca^{2+} at a 2.5 g/L dosage using lower initial concentrations of barium through kinetic batch experiments.

6.5. Effect of the initial Ba^{2+} concentration (C_0)

Kinetic batch experiments were conducted using a adsorbent dose of 2.5 g/L to investigate the adsorption behavior of Ba^{2+} at various initial concentrations. Three different initial concentrations, 150 mg/L, 75 mg/L, and 50 mg/L, were examined (see Figure 6.6 (a)). The obtained curves for all three concentrations were effectively fitted using the pseudo first-order kinetic model (see Table 6.4). Analyzing these curves revealed distinct equilibrium adsorption capacities: the highest capacity was observed at 41.2 mg/g for an initial concentration of 150 mg/L, followed by 26.9 mg/g for 75 mg/L, and the lowest adsorption capacity of 19.3 mg/g for 50 mg/L initial concentration.

In terms of removal efficiencies (see Figure 6.6 (b)), a high level of effectiveness was achieved. For initial Ba^{2+} concentrations of 50 mg/L and 75 mg/L, removal efficiencies of 95% and 90%, respectively, were completed within 200 minutes. However, for the initial concentration of 150 mg/L, the maximum removal efficiency of 75% was obtained after 800 minutes of the experiment.

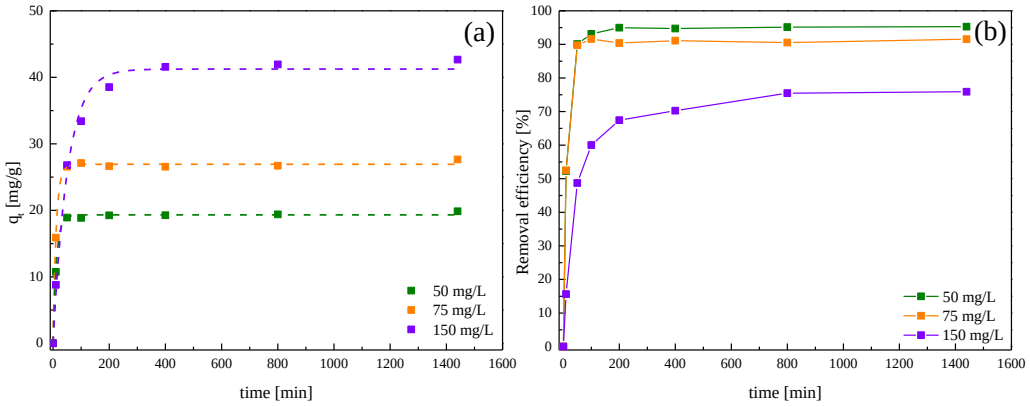

Figure 6.6. (a) P-Ca^{2+} adsorption kinetics on Ba^{2+} different C_0 solutions, dashed lines corresponds to the fitting by PFO kinetic model, and (b) removal rates.

Regarding the K_1 parameter from the fitting of PSO, we can observe that the adsorption rates constants are 0.081, 0.09, and 0.02 min^{-1} for the initial Ba^{2+} concentrations of 50 mg/L, 75

mg/L, and 150 mg/L, respectively. This data is coupled with the time required for a dose of 2.5 g/L of P-Ca^{2+} to reach maximum removal efficiencies.

Table 6.4. Kinetic parameters with different Ba^{2+} initial concentrations.

Kinetic parameters for P-Ca^{2+} for Ba^{2+} remediation					
Ba^{2+} C_0 [mg/L]	**Model**	**R^2_{adj}**	**K_1[min^{-1}]**	**q_{eq} [mg/g]**	**R [%] max**
50	PFO	0.99	0.081 ± 0.004	19.31 ± 0.12	95.15
75	PFO	0.99	0.090 ± 0.004	26.92 ± 0.15	90.55
150	PFO	0.99	0.020 ± 0.000	41.24 ± 0.78	75.48

6.6. Dual simultaneous removal of divalent cations by P-Ca^{2+}

This section focuses on the simultaneous removal of nickel and zinc at lower concentrations than those discussed for Barium. In this case, the concentrations of Ni^{2+} and Zn^{2+} were 500 µg/L (500 ppb). These concentrations are in the range typically observed in water bodies contaminated by these pollutants[10,11].

6.6.1. Single component system: nickel adsorption at low concentrations

To assess the adsorption of P-Ca^{2+} film at low concentrations of divalent metals, adsorption kinetic batch experiments were conducted using initial concentrations of nickel of 500 500 µg/L. The adsorption kinetic curve is depicted in Figure 6.7 (a) and was obtained using a dose of 2.5 g/L of P-Ca^{2+}.

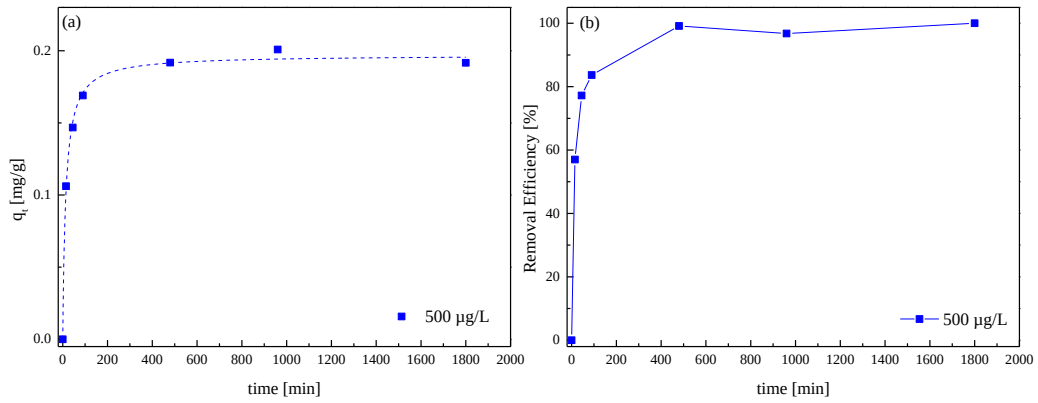

Figure 6.7. Adsorption kinetic plot of P-Ca2+ against 500 µg/L of Ni^{2+} (a) dashed line corresponds to the fitting by PSO kinetic model and removal efficiencies against time (b).

The kinetic adsorption experiments (see Table 6.5) yielded an equilibrium adsorption capacity of 1.5 ± 0.4 mg/g. While this value may appear low, it is a consequence of working with

extremely low concentrations of the adsorbate. The K_2 parameter indicated a rapid adsorption rate, with a value of 0.37 ± 0.03g/(mg min). Remarkably, the removal efficiency reached 100%, indicating that any remaining nickel in the solution was below the detection limit of 1.5 µg/L as determined by ICP-AES analysis.

Table 6.5. Kinetic parameters of the fitting performed with PSO model for zinc and nickel alone.

Adsorbate	R^2_{adj}	K_2 [g/(mg min)]	q_{eq} [mg/g]	RE_{max} [%]
Zinc	0.99	1.5 ± 0.4	0.210 ±0 .004	100
Nickel	0.99	0.37 ± 0.03	0. 200 ± 0.002	100

6.6.1. Single component system: zinc adsorption at low concentrations

The kinetic adsorption investigation was carried out using zinc under identical conditions as the nickel experiments. The outcomes (see Figure 6.8 and Table 6.5) unveiled an equilibrium adsorption capacity of 0.21 mg/g, accompanied by a remarkably high adsorption rate (K_2) value of 1.5 g/(mg min), indicating a rapid adsorption process. The removal efficiency reached 100%, indicating that the concentration of zinc remaining in the solution was below the detection limit of 5 µg/L as determined by ICP-AES analysis.

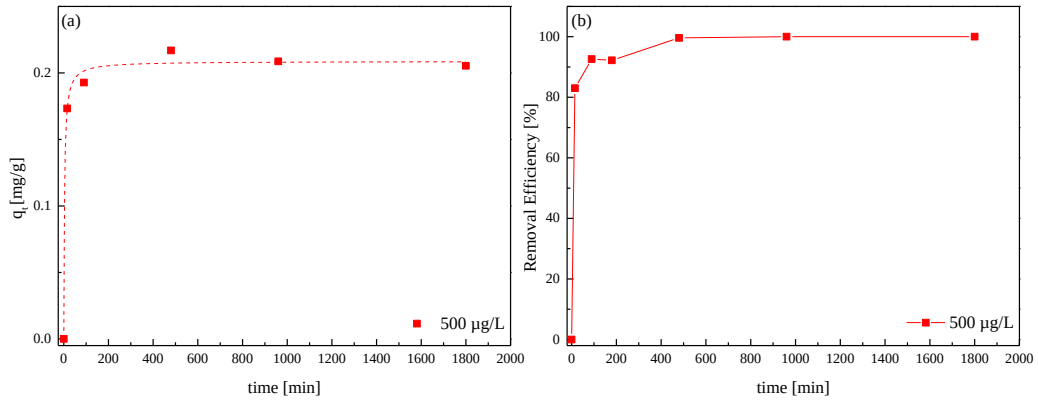

Figure 6.8. Adsorption kinetic plot of P-Ca^{2+} against 500 mg/L of Zn^{2+} (a) dotted line corresponds to the fitting by PSO kinetic model and removal efficiencies against time (b).

6.6.3. Multi component system adsorption: simultaneous removal of nickel and zinc at low concentrations by P-Ca^{2+}

The kinetic batch adsorption experiments were conducted to analyze the adsorption behavior of a multi-component system comprising 500 µg/L of zinc and nickel. The kinetic curves can be observed in Figure 6.9 (a), while the corresponding kinetic fitting parameters are presented

in Table 6.6. In this dual system, the equilibrium adsorption capacity for nickel removal was determined to be 0.21 mg/g, whereas for zinc removal it was found to be 0.18 mg/g. The K_2 values were calculated as 0.23 g/(mg min) for zinc and 0.15 g/(mg min) for nickel, indicating that the adsorption process occurs at a rapid rate for both metals, albeit slightly faster for zinc.

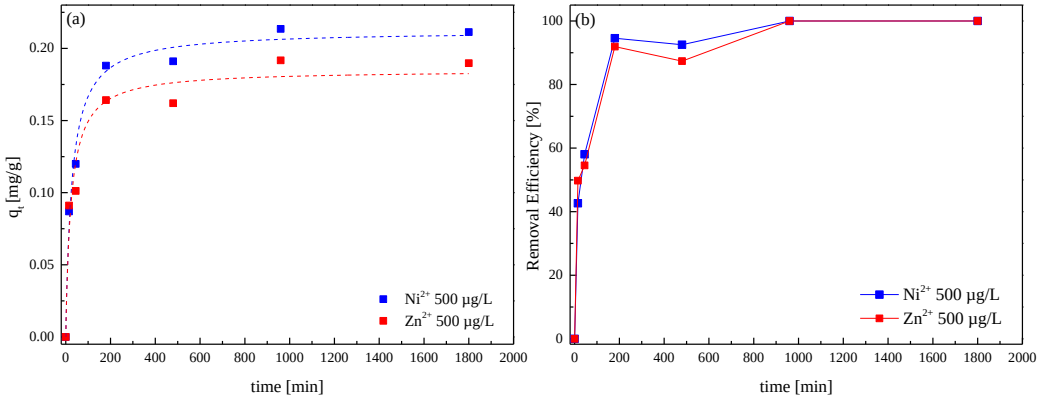

Figure 6.9. Simultaneous adsorption kinetics of P-Ca^{2+} against 500 mg/L of $Zn^{2+}$and Ni^{2+} (a) dotted line corresponds to the fitting by PSO kinetic model and removal efficiencies against time (b).

The removal rates for both metals reached 100% within the initial 960 minutes (16 hours) of the experiment.

Table 6.6. Pseudo second order kinetic parameters for the multicomponent system adsorption.

Adsorbate	**R^2_{adj}**	**K_2 [g/(mg min)]**	**q_{eq} [mg/g]**	**RE_{max} [%]**
Zinc	0.95	0.23 ± 0.07	0.18 ±0.0	100
Nickel	0.99	0.15 ± 0.03	0.21 ±0.01	100

In order to assess the potential influence of one divalent metal on the adsorption of the odther, the ratio of the adsorption capacity in the multi-component system to that in the single-component system was calculated. This ratio serves as an indicator of the interaction between the contaminants. If the ratio is greater than 1, it suggests a promotion of contaminant adsorption in the presence of the other metal (synergism). Conversely, if the ratio is less than 1, it indicates a decrease in contaminant adsorption due to the presence of the other contaminant (antagonism). A ratio of 0 signifies no influence of one contaminant on the adsorptive process of the other. For zinc, the calculated ratio was 0.89, indicating a slight antagonistic effect of nickel on the

adsorption process of zinc by the P-Ca^{2+} film. On the other hand, the ratio for nickel was 1.08, suggesting a small degree of synergism in the adsorption of nickel in the presence of zinc.

Based on the aforementioned results, it is evident that P-Ca^{2+} exhibits remarkable adsorption capabilities for both nickel and zinc, particularly in a multi-component system.

6.7. Reuse of P-Ca^{2+} adsorbent

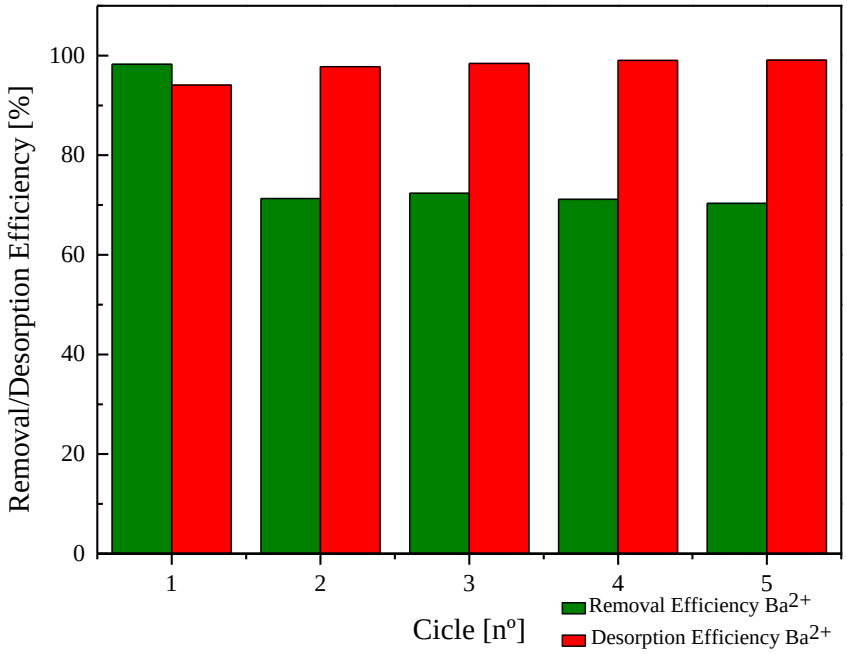

Figure 6.10. Adsorption (green) desorption (red) cycles of P-Ca^{2+} film against Ba^{2+} 25 mg/L solution.

To assess the reuse of the P-Ca^{2+} adsorbent, five consecutive adsorption-desorption cycles were conducted. Each cycle consisted of the following steps: immersing the P-Ca^{2+} film in a 25 mg/L Ba^{2+} solution at pH 7, using a dose of 2.5 g/L for 24 hours. Subsequently, excess water from the film was eliminated using absorbent paper. Next, the film was immersed in a 0.1 HNO_3 solution (pH = 1.2) for 2 hours. The film was then rinsed to remove any excess of the acid before being reused to treat a 25 mg/L Ba^{2+} solution again.

Table 6.7. Removal and desorption efficiencies obtained in the five adsorption-desorption cycles.

Cycle [nº]	Removal efficiency [%]	Desorption efficiency [%]
1	98.3	94.1
2	71.3	97.8
3	72.4	98.4
4	71.1	99.0
5	70.3	99.1

Based on the experimental results (see Figure 6.10. and Table 6.7.), it can be observed that the film achieved a 98.3% removal efficiency and a significant 94.1% desorption efficiency. This indicates that nearly all Ba^{2+} ions in the contaminated solution was effectively adsorbed by the film and subsequently transferred into the acid solution.

However, as the successive cycles progressed, the removal efficiency gradually declined to approximately 70%, specifically reaching values of 71.3%, 72.4%, 71.1%, and 70.3% for cycles 2, 3, 4, and 5, respectively. On the other hand, the desorption efficiency surpassed that of the initial cycle, with values of 97.8%, 98.4%, 99.0%, and 99.1% for cycles 2, 3, 4, and 5, respectively.

6.8. Removal of chlorpheniramine maleate from aqueous media using P-Ca^{2+} adsorbents with different crosslink levels

As discussed in the introduction (chapter 3 section 3.6.1.), pectin crosslinked with calcium has a good adsorption capacity for heavy metals. In this case, the adsorption mechanism of pectin-based adsorbents is described as an ionic exchange between the calcium atoms (forming the "egg-box" zones) and the ions to remediate[12]. However, as far as we know, pectin-based adsorbents have never been used to remediate other types of molecules, such as pharmaceuticals. Therefore, in this section, we investigate the adsorption behavior of chlorpheniramine maleate (CPM) on P-Ca^{2+} adsorbents. Chlorpheniramine maleate is an antihistamine employed to alleviate symptoms caused by allergies, the common cold, or the flu[13].

In the following, we will study three different crosslink levels in P-Ca^{2+} film to analyze how the calcium content influences the adsorption capacity of the adsorbent. The different

crosslink levels were achieved by varying the crosslink time (20, 40, and 400 min) using a solution with 500 mg/L of Ca^{+2}. From the figure 5.2 in Chapter 5, we can calculate the quantity of calcium per gram of pectin. In this way, we obtain the three following samples:

1) Crosslinking time of 20 minutes: 15.41 g of calcium per gram of pectin designated as P-Ca^{2+}(20).

2) Crosslinking time of 40 minutes: 17.9 g of calcium per gram of pectin designated as P-Ca^{2+}(40).

3) Crosslinking time of 400 minutes: 20.74 g of calcium per gram of pectin designated as P-Ca^{2+}(400).

Figure 6.10 shows the kinetic adsorption for the three films with an initial CPM concentration of 50 mg/L at pH 7. The dose of the pectin films was 2.5 g/L for the three adsorbents

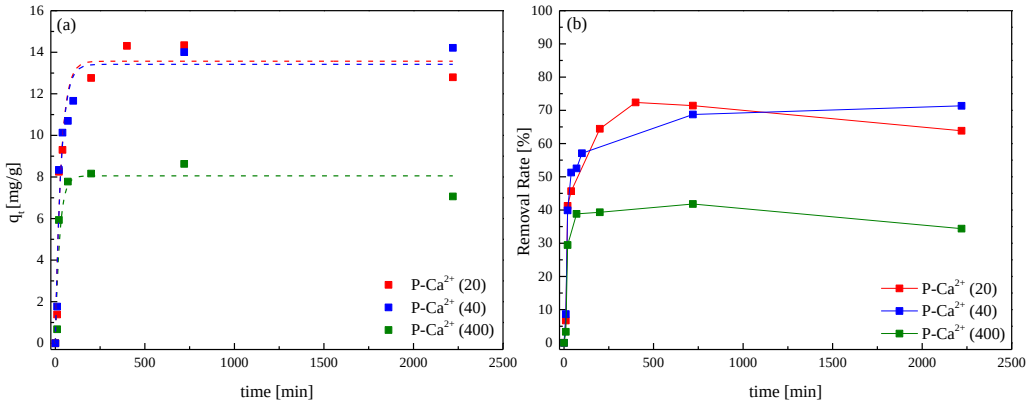

Figure 6.11. Kinetic adsorption curves for CPM adsorption at an initial concentration of 50 mg/L (a) and removal rates (b).

The resulting kinetic curves can be observed in Figure 6.11 (a), and the corresponding kinetic parameters are provided in Table 6.8. The pseudo-first-order kinetic model was selected to analyze the data due to its superior fitting performance with the experimental data.

The equilibrium adsorption capacities obtained were as follows: P-Ca^{2+}(400) reached a value of adsorption capacity of 8.05 mg/g, whereas P-Ca^{2+}(40) and P-Ca^{2+}(20) exhibited a very similar adsorption capacity of 13.4 mg/g and 13.6 mg/g, respectively. Thus, the sample with more calcium content has the lower adsorption capacity. This indicates that calcium is not an active part of the adsorption process of pharmaceuticals, contrary to heavy metals, where an interchange between the metal ion and the calcium ion is produced.

Regarding the adsorption rate constant, the K_1 parameter values were very similar across all the samples, being 0.04 min^{-1} for P-Ca^{2+}(40), 0.03 min^{-1} for P-Ca^{2+}(40), and 0.03 min^{-1} for P-Ca^{2+}(20). The highest removal efficiencies were achieved by the P-Ca^{2+}(20) and P-Ca^{2+}(40) films, with a value of 72.4% and 71.6% respectively (see Figure 6.10 (b) and Table 6.8). Finally, P-Ca^{2+}(400) exhibited a lower removal efficiency of 47.2 %.

Table 6.8. Fitting parameters obtained by pseudo first order kinetic model fit and maximum removal rates for CPM adsorption.

Adsorbent	**Dose [g/L]**	**R^2_{adj}**	**K_1 [min^{-1}]**	**q_{eq} [mg/g]**	**RE_{max} [%]**
P-Ca^{2+}(20)	2.5	0.94	0.03± 0.01	13.57± 0.69	72.4
P-Ca^{2+}(40)	2.5	0.93	0.03 ± 0.01	13.42± 0.86	71.6
P-Ca^{2+}(400)	2.5	0.88	0.04 ± 0.01	8.05 ± 0.66	47.2

Upon analyzing the data obtained, it becomes evident that the P-Ca^{2+}(20) and P-Ca^{2+}(40), with the lower crosslinking times (20 min and 40 min) and, therefore, with the lower calcium contents, displayed the highest adsorption capacities and achieved the most effective removal efficiencies. This behavior is opposite to that observed in the remediation of heavy metals, for which the higher the calcium content, the greater the effective removal efficiency.

To get insights into the remediation of the CPM mechanism, we have analyzed the possible release of calcium ions during the adsorption of CPM by measuring the calcium content of the remediated solutions by ICP-AES. We find that a no-significant quantity of calcium is released during the CPM. Therefore, we can assume that in the case of pharmaceuticals, by contrast to heavy metals, there is no interchange between the CPM molecule and the calcium ions.

This observation can be attributed to the fact that the P-Ca^{2+}(20) and P-Ca^{2+}(40) samples have a lower calcium content and therefore forms small amounts of “egg-box” structure. This is related to higher adsorption efficiency towards CPM because more COO^- and OH groups are available. On the other hand, the P-Ca^{2+} sample with a longer crosslinking time demonstrated a higher calcium content, forming a more pronounced "egg-box" structure compared to the previous films. As a result, there are fewer available COO^- and OH groups in this film. This leads to a lower adsorption capacity by P-Ca^{2+}(400). Evidently, when the film becomes saturated with Ca^{2+}, it appears to interfere with the adsorption of CPM. This phenomenon can be plausibly explained by the film reaching saturation, where the high formation of the "egg-box" structure limits the presence of OH and COO^- groups. This hindered interaction with Chlorpheniramine maleate leads to decreased adsorption on the P-Ca^{2+} (400) film.

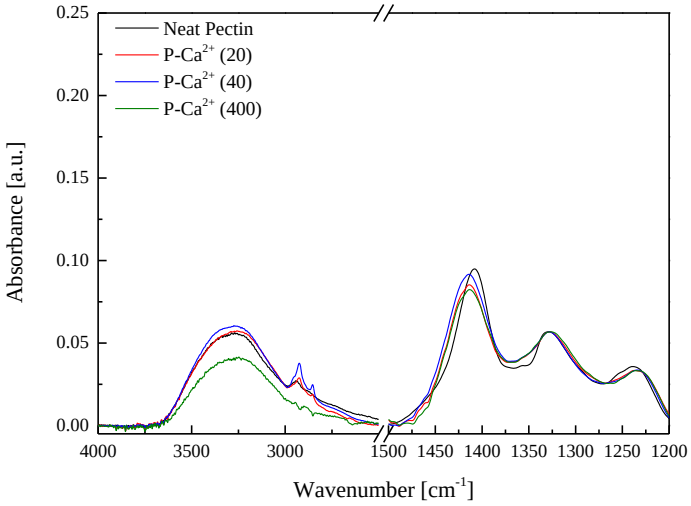

Figure 6.12. FT-IR spectra of the neat pectin and the 3 crosslinked pectin films, P-Ca^{2+} (20), P-Ca^{2+} (40), and P-Ca^{2+} (400).

To assess the differences in CPM adsorption, FT-IR measurements were conducted on the three crosslinked films (P-Ca^{2+}(20), P-Ca^{2+}(40), and P-Ca^{2+}(400)) to determine their OH and COO^{-}content. FT-IR spectra are shown in figure 6.12. Our focus is on the broad band ranging from 3600 cm^{-1} to 3000 cm^{-1}, corresponding to the stretching of the OH groups associated with the intermolecular hydrogen bonds of the galacturonic acid[14]. The intensity of the mentioned band appears similar in neat pectin, P-Ca^{2+}(20), and P-Ca^{2+}(40). However, P-Ca^{2+}(400) shows a lower intensity, indicating a reduced presence of OH groups in the film, which may affect its potential interaction with CPM. In respect to the COO^{-}, we focused on the peak situated at 1408 cm^{-1} which is related to the symmetric stretching of COO^{-}[15]. We can observe a decay in the intensity of the band from P-Ca^{2+}(400) with respect to P-Ca^{2+}(20) and P-Ca^{2+}(40), which indicates less COO^{-} content in P-Ca^{2+}(400) sample. This may explain the differences in adsorption between the 3 different times of crosslink pectin films.

6.9. Conclusions

In a report by the Word Health Organization (WHO)[16], the highest barium concentration found through several studies was in northern Illinois in the USA, ranging from 1.1 to 10 mg/L. This was found in drinking sources such as deep rock and drift wells. The limit concentration for human drinking water established by the WHO[17] is 0.7 mg/L, and 2 mg/L by the US EPA[18] and 1 mg/L by the Health Canada[19]. The European Union has not established a limit for barium in drinking water.

Considering these observations along with the findings from the isotherm batch experiments, it is evident that both 1 g/L and 2.5 g/L dosages of P-Ca^{2+} demonstrate the ability to effectively remediate a 10 mg/L Ba^{2+} solution to a concentration lower than 0.7 mg/L.

Notably, both doses exhibit a remarkable removal rate of 95%, resulting in a maximum Ba^{2+} concentration of 0.5 mg/L in the 10 mg/L Ba^{2+} treated solution. These outcomes establish the P-Ca^{2+} film with a 1 g/L dosage as a highly suitable material for remediating aqueous solutions contaminated by barium

The versatility of this material allows for its reutilization in multiple adsorption cycles, with a minimum of five cycles achievable. While it is worth noting that the removal efficiency declines to 70% starting from the second cycle, it is important to consider that the highest barium concentration reported in water bodies by the WHO study was 10 mg/L.

As previously observed (see section 6.6.), zinc and nickel are present in polluted water bodies at concentrations ranging from µg/L to ng/L. P-Ca^{2+} film was able to remove completely a solution containg 500 µg/L of zinc and nickel. In light of this information, P-Ca^{2+} films serve as suitable material for effectively removing simultaneously these pollutants from contaminated water sources.

Finally, we also explore the remediation of pharmaceuticals using P-Ca^{2+} adsorbents. Three P-Ca^{2+} films with different calcium content where tested against chlorpheniramine maleate. The sample with higher calcium content (P-Ca^{2+}(400)) demonstrated the least favorable outcomes concerning adsorption capacity and removal efficiency, While P-Ca^{2+}(20) and P-Ca^{2+}(40) exhibited very similar adsorption capacities and removal efficiencies. This could be attributed to the limited presence of OH and COO^{-}, as FT-IR measurements revealed, on P-Ca^{2+} (400) due to saturation by calcium ions and larger formation of the “egg-box” structure, resulting in reduced interactions with chlorpheniramine maleate. Moreover, calcium release in the adsorption process was followed by ICP-AES measurements, revealing a marginal calcium release. This evidenced that, unlike heavy metals, the adsorption mechanism of this pharmaceutical º present in the pectin-based adsorbent.

REFERENCES

1. Fishman, M. L. *et al.* Effect of long term cold storage and microwave extraction time on the physical and chemical properties of citrus pectin. *Food Hydrocoll.* **92**, 104–116 (2019).

2. Kohn, R. Ion binding on polyuronates - alginate and pectin. **42**, 371–397 (1975).

3. Dronnet, V. M., Renard, C. M. G. C., Axelos, M. A. V & Thibault, J.-F. Characterisation and selectivity of divalent metal ions binding by citrus and sugar-beet pectins. *Carbohydr. Polym.* **30**, 253–263 (1996).

4. Celus, M., Kyomugasho, C., Van Loey, A. M., Grauwet, T. & Hendrickx, M. E. Influence of Pectin Structural Properties on Interactions with Divalent Cations and Its Associated Functionalities. *Compr. Rev. Food Sci. Food Saf.* **17**, 1576–1594 (2018).

5. Celus, M. *et al.* Fe2+ adsorption on citrus pectin is influenced by the degree and pattern of methylesterification. *Food Hydrocoll.* **73**, 101–109 (2017).

6. Kohn, R. Binding of divalent cations to oligomeric fragments of pectin. *Carbohydr. Res.* **160**, 343–353 (1987).

7. Luzio, G. A. & Cameron, R. G. Demethylation of a model homogalacturonan with the salt-independent pectin methylesterase from citrus: Part II. Structure–function analysis. *Carbohydr. Polym.* **71**, 300–309 (2008).

8. Braccini, I. & Pérez, S. Molecular Basis of Ca2+-Induced Gelation in Alginates and Pectins: The Egg-Box Model Revisited. *Biomacromolecules* **2**, 1089–1096 (2001).

9. Martinez, Y. N., Piñuel, L., Castro, G. R. & Breccia, J. D. Polyvinyl Alcohol–Pectin Cryogel Films for Controlled Release of Enrofloxacin. *Appl. Biochem. Biotechnol.* **167**, 1421–1429 (2012).

10. Zhou, Q. *et al.* Total concentrations and sources of heavy metal pollution in global river and lake water bodies from 1972 to 2017. *Glob. Ecol. Conserv.* **22**, e00925 (2020).

11. Varol, M. & Şen, B. Assessment of nutrient and heavy metal contamination in surface water and sediments of the upper Tigris River, Turkey. *CATENA* **92**, 1–10 (2012).

12. Harel, P., Mignot, L., Sauvage, J.-P. & Junter, G.-A. Cadmium removal from dilute aqueous solution by gel beads of sugar beet pectin. *Ind. Crops Prod.* **7**, 239–247 (1998).

13. Xia, C. *et al.* Removal of Chlorpheniramine from Water by Birnessite. *Water, Air, Soil Pollut.* **225**, 2131 (2014).

14. Santos, E. E. *et al.* Extraction of pectin from agroindustrial residue with an ecofriendly solvent: use of FTIR and chemometrics to differentiate pectins according to degree of methyl esterification. *Food Hydrocoll.* **107**, 105921 (2020).

15. Guo, X., Duan, H., Wang, C. & Huang, X. Characteristics of two calcium pectinates prepared from citrus pectin using either calcium chloride or calcium hydroxide. *J. Agric. Food Chem.* **62**, 6354–6361 (2014).

16. (WHO), W. H. O. WHO. Barium in Drinking-Water. Geneva; 2016. (2016).

17. Herschy, R. W. Water quality for drinking: WHO guidelines. *Encycl. Earth Sci. Ser.* 876–883 (2012). doi:10.1007/978-1-4020-4410-6_184

18. Agency, U. S. E. P. & Water, O. 2018 Edition of the Drinking Water Standards and Health Advisories Tables. (2018).

19. Oram, B. Barium in Drinking Water and Saline/Brine Waters. *Water Res. Cent.* 1–49 (2019).

Chapter 7

Remediation of water by crosslinked pectin with Eu^{3+} and the dual crosslinking system (Ca^{2+}-Eu^{3+})

The main goal of this chapter is to explore the practical use of the newly developed europium-crosslinked pectin-based adsorbents for water remediation. We initially examined the adsorbents' effectiveness in removing heavy metals, specifically zinc, and assessed their ability to adsorb antibiotics such as tetracycline and ciprofloxacin individually. Subsequently, we employed the dual crosslink system to investigate the multi-component system removal of zinc and tetracycline. This step aimed to determine if any competitive effects or inhibitions can be detected in the adsorption process, and to evaluate the material's dual adsorption capabilities for both pollutants. To our knowledge, there are no reports on the adsorption of other emerging contaminants, such as pharmaceuticals using pectin-based adsorbents.

7.1. Kinetics of Zn^{2+} and pharmaceutical sorption on three reticulated pectin adsorbents

7.1.1. Non-simultaneous removal of heavy metals

The section aims to examine the adsorption capacity of the three pectin-based adsorbents against divalent metals, specifically Zn^{2+}. The literature extensively supports the use of pectin crosslinked with Ca^{2+} as an effective material for eliminating divalent metals from aqueous media[1–3], a finding further substantiated in the previous chapter when dealing with Ba^{2+}. However, our objective now is to investigate the adsorption capacity of the P-Eu^{3+} and P-Ca^{2+}-Eu^{3+} films concerning Zn^{2+}.

The three adsorbent developed (P- Ca^{2+}, P-Eu^{3+}, and P-Ca^{2+}-Eu^{3+}) were tested at pH = 7, with a concentration of Zn^{2+} of 150 mg/L. The results are presented in Figure 7.1 and Table 7.1. The experimental data was best described by fitting the kinetic curves with the pseudo-second order (PSO) kinetic model, which provided a superior fit and explanation for the observed kinetics.

The maximum removal efficiency decreased from 75.0 % to 47.2 % and 37.9 % for P-Ca^{2+}, P-Ca^{2+}-Eu^{3+}, and P-Eu^{3+}, respectively. Similarly, the adsorption capacities followed a similar pattern, with P-Ca^{2+} exhibiting the highest capacity of 44.6 mg/g, followed by P-Ca^{2+}-Eu^{3+} at 26.9 mg/g, and finally, P-Eu^{3+} displaying the lowest capacity of 22.4 mg/g.

As anticipated, the adsorption of Zn^{2+} seems to be associated with the formation of the "egg-box" structure resulting from the crosslinking of LM pectin by Ca^{2+} ions. As previously demonstrated (see Chapter 5, Figure 5.6), the P-Ca^{2+}-Eu^{3+} sample contained fewer Ca^{2+} ions than the P-Ca^{2+} sample, resulting in a reduced area of the material adopting the "egg-box" structure. Surprisingly, the P-Eu^{3+} sample also displayed the ability to adsorb Zn^{2+}, albeit with a lower removal efficiency than the P-Ca^{2+} adsorbent. The exact reason behind the Zn^{2+} adsorption capacity of the P-Eu^{3+} sample remains unclear. We do not expect a strong interaction between Eu^{3+} and Zn^{2+}, so the more plausible explanation is that Zn^{2+} is a divalent cation that can crosslink pectin[4] similarly to those explained by Ca^{2+}, and for this reason, Zn^{2+} is adsorbed by the P-Eu^{3+}.

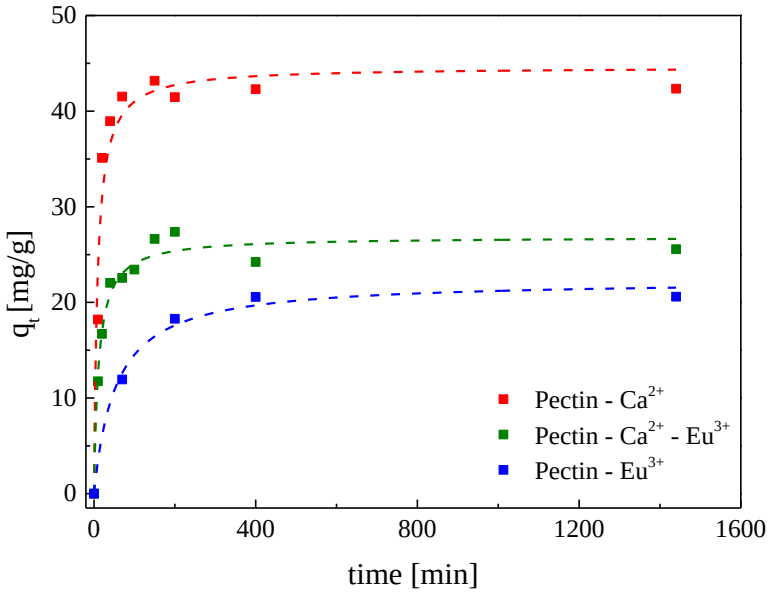

Figure 7.1. Kinetics of Zn^{2+} sorption by pectin crosslinked with Ca^{2+}, Eu^{3+}, and Ca^{2+}-Eu^{3+}. Adsorbent dose: 2.5 g/L, initial Zn^{2+} concentration: 150 mg/L. Dashed lines represent the fitting of the PSO model (see Table 3).

Table 7.1. PSO kinetic parameters for Zn^{2+} sorption into P–Ca^{2+}, P–Eu^{3+}, and P–Ca^{2+}-Eu^{3+}.

Sample	R^2_{adj}	K_2 [g/(mg min)]	q_{eq} [mg/g]	RE_{max} [%]
P–Ca^{2+}	0.96	0.0026 ± 0.0007	44.6 ± 1.6	75.0
P–Ca^{2+}-Eu^{3+}	0.98	0.0032 ± 0.0006	26.9 ± 0.7	47.2
P–Eu^{3+}	0.99	0.0008 ± 0.0002	22.4 ± 0.9	37.9

The results obtained regarding the K_2 parameter, which sheds light on the adsorption rate in the PSO model, reveal distinct patterns. The P-Ca^{2+}-Eu^{3+} sample showcases the most rapid adsorption rate, with a K_2 value of 0.0032 g/(mg min), closely followed by P-Ca^{2+} at 0.0026 g/(mg min). In contrast, the adsorption rate of the P-Eu^{3+} sample is comparatively slower, displaying a K_2 value of 0.0008 g/(mg min).

By associating the adsorption of Zn^{2+} with the "egg-box" structure, we can anticipate the observed outcomes. It is evident that the P-Ca^{2+}-Eu^{3+} sample possesses areas with the already "egg-box" structure formed, albeit in lesser amounts compared to those in P-Ca^{2+}. As a result, the adsorption process is faster and the adsorption capacity for Zn^{2+} is lower for the P-Ca^{2+}-Eu^{3+} adsorbent comparing to P-Ca^{2+}, because less “egg-box” structure is present in P-Ca^{2+}-Eu^{3+} film.

On the contrary, the absence of the "egg-box" structure in P-Eu^{3+} indicates that the adsorption of Zn^{2+} occurs through the crosslinking of pectin by Zn^{2+} in a localized manner, resembling points of crosslink. This mechanism leads to a slower adsorption process by P-Eu^{3+} adsorbent.

7.1.2. Non-simultaneous removal of antibiotics

We performed kinetic adsorption experiments with two antibiotics: ciprofloxacin (CIP) and tetracycline (TC). To our knowledge, there are no previous reports of any pectin-based material capable of removing antibiotics from aqueous media. It was widely reported in literature that europium and these two antibiotics strongly interact. These interactions have been used to develop europium-based sensors to detect tetracycline[5,6] and ciprofloxacin[7]. In this thesis, this interaction between pharmaceuticals and europium is used to remove this type of molecules from polluted aqueous media.

7.1.2.1. Tetracycline removal

7.1.2.1.1 Isotherm

Some preliminary tests were performed using the P-Ca^{2+} adsorbent to remove Tetracycline from a 10 mg/L solution at pH = 7 for 24 hours. As expected, the adsorption was residual, presenting a removal efficiency of 0.33 %. Attending to this result, the adsorbents evaluated for antibiotic removal were P-Eu^{3+} and P-Ca^{2+}-Eu^{3+}.

P-Eu^{3+} and P-Ca^{2+}-Eu^{3+} films were tested on an adsorption isotherm with concentrations ranging 5 to 60 mg/L at pH = 7 with a film dose of 2.5 g/L. Adsorption isotherms (see Figure 7.2) were fitted by Langmuir isotherm model. Fitting parameters (see Table 7.2) revealed a maximum adsorption capacity of 46.2 mg/g and 12.9 mg/g for P-Ca^{2+}-Eu^{3+} and P-Eu^{3+} respectively. This result is coherent, because P-Ca^{2+}-Eu^{3+} has more europium content than P-Eu^{3+} film.

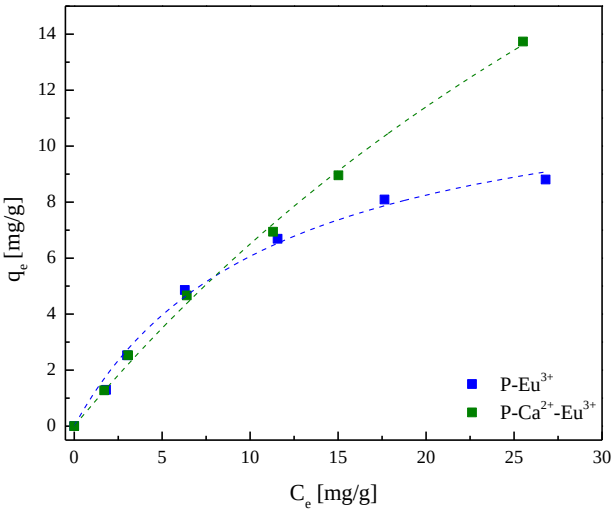

Figure 7.2. Adsorption isotherm for P-Eu3+ and P-Ca^{2+}-Eu^{3+} fo TC removal with a dose of 2.5 g/L. Dashed lines corresponds to Langmuir isotherm fit.

Regarding K_L parameter P-Eu^{3+} exhibited a value of 0.089 L/mg while P-Ca^{2+}-Eu^{3+} reached a value of 0.016 L/mg. This result suggest that tetracycline has stronger affinity towards P-Eu^{3+} film. This could be because P-Eu^{3+} film does not have any "egg-box" structure, which can facilitate the tetracycline diffusion towards europium ions.

Regarding removal efficiencies, at highest concentration tested (60 mg/L), P-Eu^{3+} film was able to remove 44.6 % of the tetracycline present in the solution, while P-Ca^{2+}-Eu^{3+} removed a 57.54 %.

Table 7.2. Adsorption isotherm fitting parmeters. Fitting performed with the Langmuir isotherm model.

Adsorbent	**R^2_{adj}**	**K_L [L/mg]**	**q_{max} [mg/g]**	**RE_{max} [%] C_0 =60 mg/L**
P-Eu^{3+}	0.99	0.089 ± 0.013	12.9 ± 0.9	44.86 %
P-Ca^{2+}-Eu^{3+}	0.99	0.016 ± 0.003	46.2 ± 7	57.52 %

7.1.2.1.1 Kinetics

Kinetic experiments were carried out with an initial antibiotic (CIP and TC) concentration of 50 mg/L at pH = 7 ranging from 10 to 1440 minutes (24 hours).

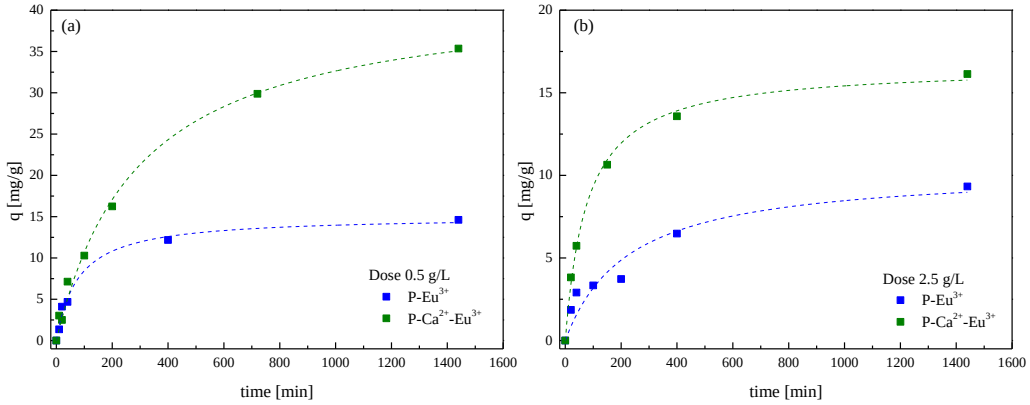

Table 7.3. Adsorption kinetics of P-Eu^{3+} and P-Ca^{2+}-Eu^{3+} for TC removal at doses of 0.5 g/L (a) and 2.5 g/L (b).

Two doses (2.5 and 0.5 g/L) were tested for each type of film (P-Eu^{3+} and P-Ca^{2+}-Eu^{3+}) to assess the kinetics of tetracycline removal. The kinetic curves (see figure 7.3 (a) and (b)) demonstrated distinct adsorption capacities at equilibrium (see Table 7.2) as determined by fitting the data with the pseudo second order kinetic model. The adsorption capacities for P-Eu^{3+} were 15.1 and 10.4 mg/g for doses of 0.5 and 2.5 g/L, respectively. On the other hand, for P-Ca^{2+}-Eu^{3+}, the adsorption capacities were 42.3 and 16.6 mg/g for doses of 2.5 and 0.5 g/L, respectively.

The results obtained for maximum removal efficiencies (refer to table 7.3. and figure 7.4.) are as follows: The highest maximum removal efficiency of 81.24% was achieved by the P-Ca^{2+}-Eu^{3+} sample at a dose of 2.5 g/L. This was followed by the P-Eu^{3+} sample at a dose of 2.5 g/L, which exhibited a maximum removal efficiency of 47.68%. The P-Ca^{2+}-Eu^{3+} film at a dose of 0.5 g/L showed a maximum removal efficiency of 36.78%, while the P-Eu^{3+} sample at a dose of 0.5 g/L had the lowest maximum removal efficiency at 18.45%.

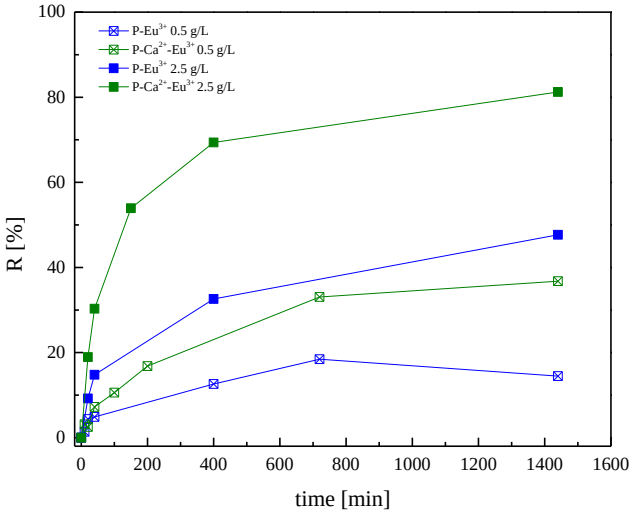

Figure 7.4. Removal efficiencies of P-Eu^{3+} and P-Ca^{2+}-Eu^{3+} adsorbents to remediate TC at doses of 0.5 and 2.5 g/L, The lines are guided for the eyes.

Regarding the adsorption rate determined by the PSO model (K_2 parameter), the quickest rate was observed for the P-Eu^{3+} sample at a dose of 0.5 g/L, closely followed by the P-Ca^{2+}-Eu^{3+} sample at a dose of 2.5 g/L. The P-Eu^{3+} film at a dose of 2.5 g/L exhibited a slightly slower adsorption rate, while the P-Ca^{2+}-Eu^{3+} sample at a dose of 0.5 g/L had the slowest adsorption rate among the tested conditions (K_2 values in table 7.3).

Table 7.3. Kinetic parameters of the batch adsorption experiments of P-Eu^{3+} and P-Ca^{2+}-Eu^{3+} adsorbents to remediate TC at doses of 0.5 and 2.5 g/L.

Sample	**Dose [g/L]**	**R^2_{adj}**	**K_2 [g/(mg min)]**	**q_{eq} [mg/g]**	**RE_{max} [%]**
P–Eu^{3+}	0.5	0.99	0.0008 ± 0.00017	15.06±0.63	18.45
P–Ca^{2+}-Eu^{3+}	0.5	0.99	0.00008 ± 0.000013	42.28±1.86	36.78
P–Eu^{3+}	2.5	0.91	0.00043 ± 0.00021	10.39±1.41	47.68
P–Ca^{2+}-Eu^{3+}	2.5	0.99	0.00077 ±0.000077	16.62±0.36	81.24

7.1.2.2. Ciprofloxacin removal

We conducted tests using three doses (0.5, 1, and 2.5 g/L) of P-Eu^{3+} and P-Ca^{2+}-Eu^{3+} with a pH of 7 on a ciprofloxacin solution with an initial concentration of 50 mg/L. The kinetic data (see Figure 7.5 and Table 7.4) was best fitted using the pseudo first order kinetic model. At a dose

of 0.5 g/L, the equilibrium adsorption capacity was 17.3 mg/g for P-Eu^{3+} and 70 mg/g for P-Ca^{2+}-Eu^{3+}. For the 1 g/L dose, P-Eu^{3+} exhibited an equilibrium adsorption capacity of 10.4 mg/g, while P-Ca^{2+}-Eu^{3+} had a capacity of 27.8 mg/g. Lastly, at a dose of 2.5 g/L, the equilibrium adsorption capacity was 16.05 mg/g for P-Eu^{3+} and 15.4 mg/g for P-Ca^{2+}-Eu^{3+}.

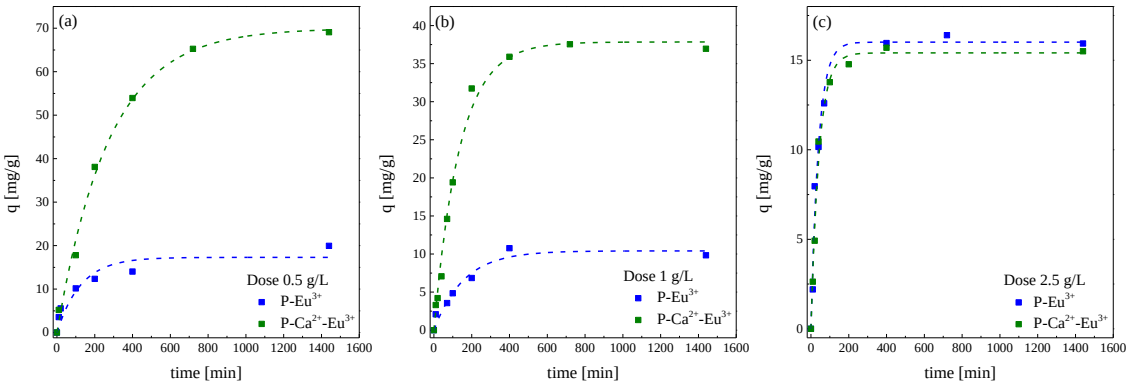

Figure 7.5. Adsorption kinetic curves of P-Eu^{3+} and P-Ca^{2+}-Eu^{3+} at 0.5 (a), 1 (1) and 2.5 (c) g/L to remediate ciprofloxacin.

The maximum removal efficiencies yielded the following outcomes. For the P-Eu^{3+} sample (see Figure 7.6 and Table 7.4), the samples with doses of 0.5 g/L and 1 g/L exhibited very similar removal efficiencies of 23.6% and 25.6%, respectively. However, the sample with a dose of 2.5 g/L achieved a significantly higher removal efficiency of 95.6%. On the other hand, the P-Ca^{2+}-Eu^{3+} samples all demonstrated high removal efficiencies. Specifically, the removal efficiencies were 84.5%, 89.2%, and 91.2% for doses of 0.5 g/L, 1 g/L, and 2.5 g/L, respectively.

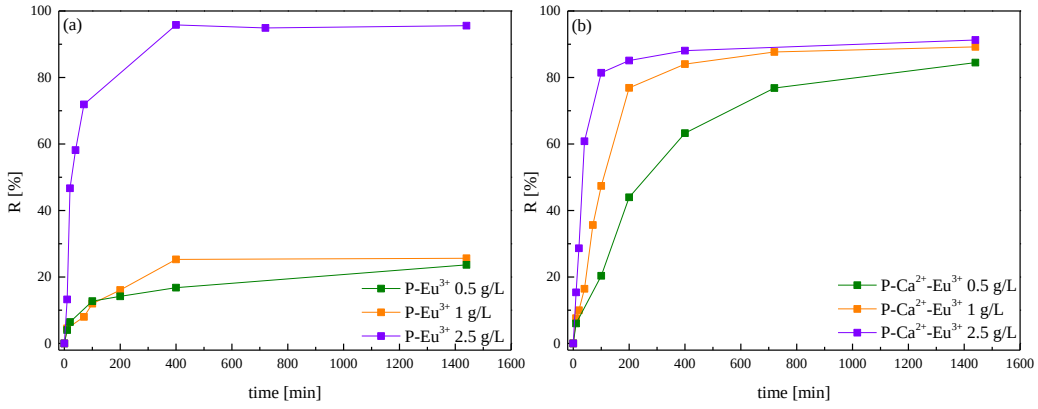

Figure 7.6. Removal efficiencies of ciprofoxacyn in function of time of P-Eu^{3+} (a) and P-Ca^{2+}-Eu^{3+} (b) at 0.5, 1, and 2.5 g/L doses. The lines are guided for the eyes.

The adsorption rate parameters showed a trend of higher values for higher doses. At a dose of 2.5 g/L, the P-Eu^{3+} sample had an adsorption rate of 0.025 L/min, while the P-Ca^{2+}-Eu^{3+} sample exhibited a rate of 0.023 L/min. For the 1 g/L dose, the P-Eu^{3+} sample had a K_2 value of 0.0064 L/min, whereas the P-Ca^{2+}-Eu^{3+} sample had a slightly higher value of 0.0073 L/min. In contrast, the slowest adsorption rates were observed for the 0.5 g/L dose. The P-Eu^{3+} sample exhibited an adsorption rate of 0.008 L/min, while the P-Ca^{2+}-Eu^{3+} sample had a lower rate of 0.0036 L/min. Notably, the P-Eu^{3+} sample deviated from this trend, displaying a higher K_2 value than the 1 g/L samples.

Table 7.4. Pseudo first order kinetic model fitting parameters for ciprofloxacin removal

Sample	Dose [g/L]	R^2_{adj}	k_1 [L/min]	q_{eq} [mg/g]	RE_{max} [%]
P–Eu^{3+}	0.5	0.87	0.008 ± 0.0029	17.3 ± 2.0	23.6
P–Ca^{3+}-Eu^{3+}	0.5	0.99	0.0036 ± 0.0003	70.0 ± 2.0	84.5
P–Eu^{3+}	1	0.94	0.0064 ± 0.0013	10.4 ± 0.8	25.6
P–Ca^{3+}-Eu^{3+}	1	0.99	0.0073 ± 0.0005	37.8 ± 0.9	89.2
P–Eu^{3+}	2.5	0.98	0.025 ± 0.0029	16.0 ± 0.5	95.6
P–Ca^{3+}-Eu^{3+}	2.5	0.99	0.023 ± 0.0021	15.4 ± 0.4	91.3

Upon comparing the obtained results for tetracycline and ciprofloxacin, it becomes evident that both P-Eu^{3+} and P-Ca^{2+}-Eu^{3+} films demonstrated superior adsorption capacities and removal efficiencies for ciprofloxacin. The adsorption mechanism, on the other hand, appears to be influenced by the europium content within the films. P-Ca^{2+}-Eu^{3+} exhibited more favorable outcomes than P-Eu^{3+} due to its higher Eu^{3+} content (see section 5.1 in Chapter 5 for more details). This interaction is likely attributed to the well-established affinity between europium and the molecular structure known as β-diketone[8–12] (see Figure 7.7), present in both tetracycline and ciprofloxacin antibiotics. In all cases, except for high doses (2.5 g/L) against ciprofloxacin where P-Ca^{2+}-Eu^{3+} achieved a removal efficiency of 91.3%, the P-Eu^{3+} adsorbent demonstrated a slightly higher efficacy with a removal efficiency of 95.6% under the same conditions. This exception could be attributed to the abundance of europium in the adsorbent at high doses with respect to the antibiotic available in the solution. Consequently, P-Eu^{3+} adsorbent has more available europium for ciprofloxacin than P-Ca^{2+}-Eu^{3+}, which, despite having a higher europium content, also features calcium forming "egg-box" structures. These structures may potentially hinder the diffusion of ciprofloxacin and its access to europium in P-Ca^{2+}-Eu^{3+} film. This aligns with the

observed K_1 values, reflecting the consistently higher adsorption rate constants for P-Eu^{3+} than P-Ca^{2+}-Eu^{3+}. These results indicate that the adsorption is quicker for P-Eu^{3+}, suggesting an earlier interaction between ciprofloxacin β-diketone and europium.

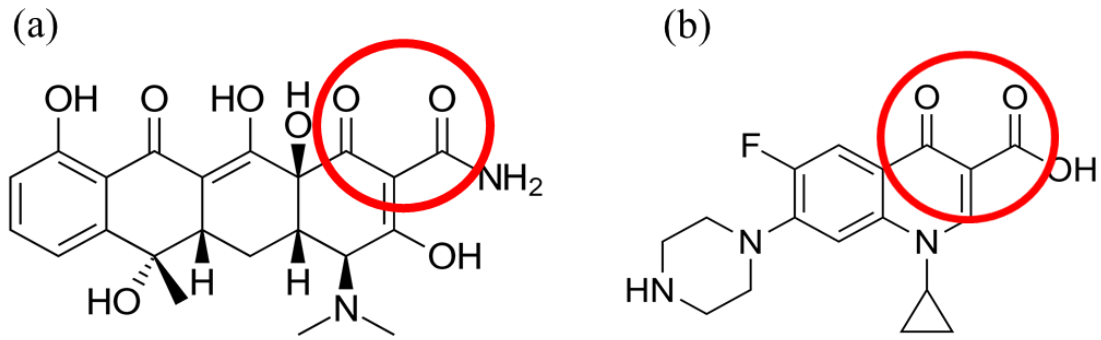

Figure 7.7. Tetracycline (a) and Ciprofloxacin (b) molecules with β-diketone groups highlighted by red circle.

7.1.3. Multi component system adsorption: Simultaneous removal of pharmaceuticals and Zn^{2+}

Traditionally, adsorption studies focus on investigating the behavior of a single pollutant. Nevertheless, water is often contaminated with multiple substances, each playing a different role in the adsorption process. These contaminants can either hinder or enhance the overall adsorption process. For instance, heavy metals may compete with pharmaceutical compounds for available adsorption sites. In the current scenario, we expect heavy metals to interact with the "egg-box" structure formed by Ca^{2+} ions. In contrast, the pharmaceutical compounds will primarily interact with the europium.

Considering these factors and the favorable outcomes observed in this thesis, P-Ca^{2+}-Eu^{3+} emerges as the chosen film for the simultaneously eliminating both heavy metals and pharmaceuticals. Therefore, for the following experiment, we chose Zn^{2+} as a representative divalent metal and tetracycline as a representative pharmaceutical compound. The adsorbent employed is P-Ca^{2+}-Eu^{3+} due to the previous positive results.

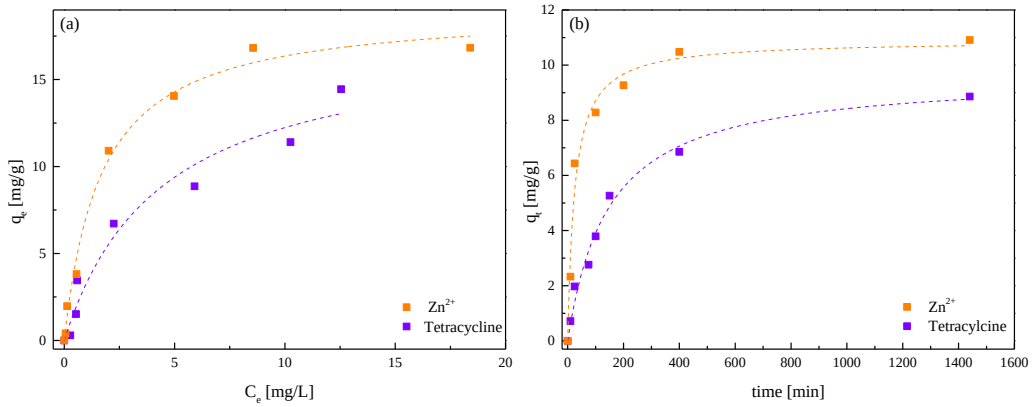

Figure 7.8. (a) Adsorption isotherms and (b) simultaneous adsorption of Zn^{2+} and tetracycline by P-Ca^{2+}-Eu^{3+}. Adsorbent dose: 2.5 g/L, initial Zn^{2+} and TC concentration: 30 ppm. Dashed lines represents the fitting of the PSO model (see Table 5).

The adsorption isotherms were performed using concentrations ranging from 1 to 60 mg/L for both tetracycline and Zn^{2+}, for 1440 minutes (24 hours). The isotherm curves can be seen in Figure 7.8 (a), and the corresponding fitting parameters are presented in Table 7.5 The Langmuir isotherm model provided the best fit for the isothermal data, which assumes that the adsorption takes place in a finite number of adsorption sites, on a homogeneous surface, and in a monolayer, ultimately, the adsorption takes place by chemical interaction (chemisorption). We did not employ the modified versions of the Langmuir isotherm model[13,14] because these models assume a competition for the active site, which is not our case (tetracycline interacts with europium by β-diketone group and zinc with the calcium formed "egg-box" structure).

The experiments revealed a maximum adsorption capacity of 19.1 mg/g for zinc removal and 17.6 mg/g for tetracycline removal. The K_L parameter indicated a stronger affinity between zinc and P-Ca^{2+}-Eu^{3+} compared to tetracycline, with values of 0.6 L/mg and 0.23 L/mg, respectively. At a concentration of 10 mg/L for both zinc and tetracycline, the removal efficiencies were found to be 94.5% and 93.6%, respectively.

Batch adsorption experiments were conducted to investigate the kinetics of zinc and tetracycline adsorption, starting with an initial concentration of 30 mg/L. The experiments spanned a time range from 10 minutes to 1440 minutes. The kinetic curves depicting the adsorption process can be observed in Figure 7.8 (b), while the corresponding fitting parameters are presented in Table 7.5. The pseudo second order kinetic model was employed to fit the kinetic data. The fitting results unveiled equilibrium adsorption capacities of 10.9 mg/g and 9.7 mg/g for zinc and tetracycline, respectively. Furthermore, the K_2 parameter indicated a faster adsorption rate for zinc compared to tetracycline, with values of 0.004 g/(mg min) and 0.0007 g/(mg min), respectively.

Table 7.5. Isothermal parameters of the Langmuir model and kinetic parameters of the pseudo second order kinetic model obtained through experimental data fitting.

Isothermal parameters				
Adsorbate	**R^2_{adj}**	**K_L [L/mg]**	**q_{max} [mg/g]**	**RE_{max} [%] C_0 =10 mg/L**
Zinc	0.99	0.60 ± 0.09	19.1 ± 0.8	94.5
Tetracycline	0.96	0.23 ± 0.09	17.6 ± 0.2	93.6
Kinetic parameters				
Adsorbate	**R^2_{adj}**	**K_2 [g/(mg min)]**	**q_{eq} [mg/g]**	**RE_{max} [%]**
Zinc	0.99	0.004 ± 0.001	10.9 ± 0.4	93.3
Tetracycline	0.99	0.0007 ± 0.0001	9.7 ± 0.5	79.5

These findings show no competition or inhibitory effects were observed between zinc and tetracycline during adsorption. The adsorption continued effectively even when both pollutants coexisted in the same aqueous solution. Additionally, there was no evidence of complexation between tetracycline and zinc. This was confirmed by UV-VIS analysis for tetracycline quantification and ICP-AES analysis for zinc quantification, which verified that the concentration of each chemical agent was accurate. Successful simultaneous removal of tetracycline and zinc was accomplished (C_0 = 10 mg/L, Removal efficiency $_{Zn}$ = 94.5, Removal efficiency $_{TC}$ = 93.6) in a solution where the tetracycline concentration exceeded its typical levels by several orders of magnitude (µg/L-ng/L)[14], and the zinc concentration surpassed the recommended maximum level for irrigation water[15] (2 mg/L) in the polluted water bodies.

The obtained outcomes demonstrate the potential of P-Ca^{2+}-Eu^{3+} as a highly promising material for effectively eliminating both divalent cations and pharmaceutical compounds from polluted water bodies simultaneously.

7.3. Conclusions

We have proven the effective removal of tetracycline and ciprofloxacin from aqueous media by our generated pectin-based adsorbents crosslinked by europium and calcium and europium. We determined that the best sample, in terms of removal efficiency, was P-$Ca2^{+}$-Eu^{3+} with a dose of 2.5 g/L, which yielded a 81.2 % and 91.3 % of removal rate of tetracycline and ciprofloxacin, respectively.

Many adsorbents have been utilized for the multi-component system adsorption of heavy metals and pharmaceuticals, such as activated carbon[16], biochar[17], clays[18], graphene oxide[19] or

chitosan[20]. However, to our knowledge, no pectin-based adsorbent is employed for this purpose. Attending to the results obtained in this section, we can determine that the europium-crosslinked pectin-based adsorbents are a novel and efficient system for removing both, heavy metals and antibiotics and heavy metals individually and simultaneously.

REFERENCES

1. Kohn, R. Binding of divalent cations to oligomeric fragments of pectin. *Carbohydr. Res.* **160**, 343–353 (1987).

2. Thakur, S., Chaudhary, J., Kumar, V. & Thakur, V. K. Progress in pectin based hydrogels for water purification: Trends and challenges. *J. Environ. Manage.* **238**, 210–223 (2019).

3. Kyomugasho, C. *et al.* Pectin nanostructure influences pectin-cation interactions and in vitro-bioaccessibility of Ca2+, Zn2+, Fe2+ and Mg2+-ions in model systems. *Food Hydrocoll.* **62**, 299–310 (2017).

4. Das, S., Ng, K.-Y. & Ho, P. C. Design of a pectin-based microparticle formulation using zinc ions as the cross-linking agent and glutaraldehyde as the hardening agent for colonic-specific delivery of resveratrol: In vitro and in vivo evaluations. *J. Drug Target.* **19**, 446–457 (2011).

5. Courrol, L. C., da Silva, M. N. & Sicchieri, L. B. Characterization of the europium tetracycline complex as a biomarker for atherosclerosis. *Biophotonics Photonic Solut. Better Heal. Care V* **9887**, 98872D (2016).

6. Courrol, L. & Samad, R. Applications of Europium Tetracycline Complex: A Review. *Curr. Pharm. Anal.* **4**, 238–248 (2008).

7. Attia, M. S., Essawy, A. A. & Youssef, A. O. Europium-sensitized and simultaneous pH-assisted spectrofluorimetric assessment of ciprofloxacin, norfloxacin and gatifloxacin in pharmaceutical and serum samples. *J. Photochem. Photobiol. A Chem.* **236**, 26–34 (2012).

8. Singh, D. *et al.* Oxide ancillary ligand-based europium β-diketonate complexes and their enhanced luminosity. *Rare Met.* **40**, 2873–2881 (2021).

9. Uekawa, M., Miyamoto, Y., Ikeda, H., Kaifu, K. & Nakaya, T. Synthesis and Properties of Europium Complexes with β-Diketone Ligands for Organic Electroluminescent Devices. *Bull. Chem. Soc. Jpn.* **71**, 2253–2258 (1998).

10. Zhu, W. *et al.* Red electroluminescence from a novel europium β-diketone complex with acylpyrazolone ligand. *Synth. Met.* **111**–**112**, 445–447 (2000).

11. Wu, F.-B. & Zhang, C. A new europium β-diketone chelate for ultrasensitive time-resolved fluorescence immunoassays. *Anal. Biochem.* **311**, 57–67 (2002).

12. Wang, D., Zheng, C., Fan, L., Zheng, J. & Wei, X. Preparation and fluorescent properties of europium (III) complexes with β-diketone ligand and 2,2-dipyridine or 1,10-phenanthroline. *Synth. Met.* **162**, 2063–2068 (2012).

13. Ahmed, M. J. & Hameed, B. H. Insights into the isotherm and kinetic models for the coadsorption of pharmaceuticals in the absence and presence of metal ions: A review. *J. Environ. Manage.* **252**, 109617 (2019).

14. Zhai, M. *et al.* Simultaneous removal of pharmaceuticals and heavy metals from aqueous phase via adsorptive strategy: A critical review. *Water Res.* **236**, 119924 (2023).

15. Noulas, C., Tziouvalekas, M. & Karyotis, T. Zinc in soils, water and food crops. *J. Trace Elem. Med. Biol.* **49**, 252–260 (2018).

16. Turk Sekulic, M. *et al.* An insight into the adsorption of three emerging pharmaceutical contaminants on multifunctional carbonous adsorbent: Mechanisms, modelling and metal coadsorption. *J. Mol. Liq.* **284**, 372–382 (2019).

17. Luo, J. *et al.* Sorption of norfloxacin, sulfamerazine and oxytetracycline by KOH-modified biochar under single and ternary systems. *Bioresour. Technol.* **263**, 385–392 (2018).

18. Ghemit, R. *et al.* Adsorptive removal of diclofenac and ibuprofen from aqueous solution by organobentonites: Study in single and binary systems. *Groundw. Sustain. Dev.* **8**, 520–529 (2019).

19. Huang, D. *et al.* Novel insight into adsorption and co-adsorption of heavy metal ions and an organic pollutant by magnetic graphene nanomaterials in water. *Chem. Eng. J.* **358**, 1399–1409 (2019).

20. Marrakchi, F., Ahmed, M. J., Khanday, W. A., Asif, M. & Hameed, B. H. Mesoporous-activated carbon prepared from chitosan flakes via single-step sodium hydroxide activation for the adsorption of methylene blue. *Int. J. Biol. Macromol.* **98**, 233–239 (2017).

Chapter 8

Conclusion

This thesis on focused on developing innovative crosslink systems for pectin with a low degree of esterification and using these materials to remediate contaminated water with pharmaceuticals products and heavy metals. Two novel materials have been synthesized and characterized, and their performance has been compared with the conventional system where pectin with a low degree of methylesterification is crosslinked with calcium (chapter 5). Furthermore, the adsorption capabilities and reusability of calcium-crosslinked LM pectin were investigated against various pollutant agents (chapter 6). The adsorption behavior of the synthesized pectin-based europium crosslinked materials (comprising europium alone and calcium-europium combinations) was evaluated. The adsorption tests encompassed heavy metals, antibiotics, and a multicomponent system of metals and antibiotics (chapter 7).

The initial section of the thesis (Chapter 5) focuses on the development of low methoxyl pectin films crosslinked using two different methods: europium alone or a dual crosslink system involving initial calcium crosslinking followed by europium crosslinking. These newly developed materials were compared with the calcium-crosslinked LM pectin using various analytical techniques. The batch adsorption isotherms and kinetics were performed to assess the crosslinking reactions.

In Chapter 5, we first characterized the crosslinking reaction of pectin with a low degree of methyl esterification using three agents using isotherms and kinetics batch experiments. It was observed that the P-Ca^{2+}-Eu^{3+} sample has the highest europium content with the penalty of a significant reduction in the calcium content (approximately 70%) due to the introduction of this lanthanide element. Then, we studied the structural changes produced in pectin when crosslinked with calcium, europium, and a combination of both calcium + europium. The most important result is obtaining a gradual amorphization of pectin (previously reticulated with calcium) by

adding europium as the crosslinking agent. Moreover, the materials crosslinked with europium has more localized crosslinking points. In contrast, the sample crosslinked with both calcium and europium exhibited a combination of "egg-box" structures (associated with calcium crosslinking) and europium-based point-like crosslink spots.

Further investigation is required to unveil the precise mechanisms underlying the interactions between europium and pectin chains, including the determination of the number of carboxyl groups coordinated with europium, whether these groups originate from the same pectin chain or different pectin chains, and the potential involvement of water molecules.

Chapter 6 concentrated on the adsorption capabilities of pectin crosslinked with calcium. Chapter 6 concentrated on the adsorption capabilities of pectin crosslinked with calcium. Although this material was deeply studied in the literature for remediation of water contaminated with heavy metals, barium was not explored. This starting point let us to

Chapter 6 concentrated on the adsorption capabilities of pectin crosslinked with calcium. Although this material was deeply studied in the literature for remediation of water contaminated with heavy metals, barium was not explored. This starting point also allows us to learn on properties of the pectin-based adsorbents (doses of absorbents, crosslinking levels, reuse, etc.). In addition, dual adsorptions were performed for zinc and nickel at microgram-per-liter concentrations. Encouraging outcomes were achieved for the three metal remediation scenarios, with a removal rate of 75.5% observed for a 150 mg/L barium solution and a 100% removal rate achieved for the dual removal of zinc and nickel at an initial concentration of 500 µg/L.

The more critical result in Chapter 6 is the discovery that P-Ca^{2+} adsorbent can remediate water polluted chlorpheniramine maleate (an antihistamine). Maximum removal efficiency at an initial concentration of 50 mg/L was 72.4 % for chlorpheniramine maleate. While removing of this contaminant was not complete, it should be noted that the concentration of 50 mg/L is notably high for pharmaceuticals, which typically appear in the range of µg/L to ng/L in polluted water bodies. At this very low concentrations (that we cannot detect with UV-VIS), the removal efficiency will be probably good. Furthermore, it has been demonstrated through ICP-AES measurements that there is no exchange of calcium ions during the adsorption process.

For future investigations related to Chapter 6, exploring the adsorption capabilities of adsorbents with varying levels of crosslinking would be intriguing. This exploration would show whether a minimal crosslink (the minimum calcium crosslink required for pectin to become insoluble) or a saturated crosslink film is more advantageous for remediation. Furthermore, to build upon the favorable outcomes achieved in removing divalent cations, conducting studies with progressively complex systems would be a logical progression for water remediation research, for instance, assessing systems involving three or more metals would reveal potential competition

for adsorption sites among the different metal ions. In the realm of pharmaceuticals, Conducting batch adsorption experiments within the µg/L to ng/L range is recommended for pharmaceuticals. Additionally, it would be prudent to test the adsorption of multiple antibiotics simultaneously to determine if the efficiencies are sustained. Investigating complex systems involving divalent metals and pharmaceuticals would offer insights into the potential competition between the components and the possibility of complexation between metals and pharmaceuticals before adsorption. Lastly, the most compelling aspect would involve testing the material in real-world polluted waters, where the complexity of the system is significantly higher, providing valuable insights into practical applications.

In Chapter 7, the adsorption capabilities of europium-containing pectin-based films were examined. The contaminants explored were zinc, ciprofloxacin, tetracycline, and a dual system of tetracycline and zinc. The adsorption performance against zinc was found to be more favorable with calcium-crosslinked pectin films reaching a removal rate of 75 %, attributed to the characteristic "egg-box" structure. Nevertheless, both P-Ca^{2+}-Eu^{3+} and P-Eu^{3+} demonstrated the ability to adsorb zinc, achieving removal efficiencies of 47% and 38%, respectively. Europium-containing pectin films exhibited promising results in the removal of antibiotics, achieving high removal efficiencies.

Lastly, the pectin film crosslinked with calcium and europium was applied to remediate a multi-component system comprising a 30 mg/L zinc/tetracycline solution. The film exhibited remarkable removal efficiencies of close to 95% for both pollutants; therefore, the P-Ca^{2+}-Eu^{3+} film is a promising candidate for the remediation of water polluted by pharmaceuticals and heavy metals.

The next step for the topics in Chapter 7 should be to study the adsorption capacities at lower concentrations, more similar to those found in water (µg/L to ng/L). It is crucial to evaluate the potential competition between the antibiotics for adsorption onto europium, considering their interaction through the shared β-diketone-europium mechanism. Furthermore, it is essential to investigate the desorption of antibiotics under controlled conditions to assess the film's reusability. Before testing the system with real polluted water, complex systems involving pharmaceuticals and heavy metals should be examined to determine the occurrence of complexation before adsorption a. Finally, rigorous testing of P-Ca^{2+}-Eu^{3+} should be conducted in real-world scenarios involving water bodies polluted with heavy metals and pharmaceuticals. This would provide valuable insights into the film's performance under complex and realistic environmental conditions.

This research has shown that pectin with a low degree of methyl esterification with an appropriate crosslinked system has the potential to be used in applications of water remediation for contaminants such as pharmaceuticals products and heavy metals.

List of publications

This thesis has contributed to the following publications:

1) A Review of Pectin-Based Material for Applications in Water Treatment
Javier Martínez-Sabando, Francesco Coin, Jorge H. Melillo, Silvia Goyanes and Silvina Cerveny.
Materials **2023**, *16*(6), 2207; https://doi.org/10.3390/ma16062207

2) Dual Crosslinking of Low-Methoxyl Pectin by Calcium and Europium for the Simultaneous Removal of Pharmaceuticals and Divalent Heavy Metals
Javier Martínez-Sabando, Francesco Coin, Juan Carlos Raposo, Aitor Larrañaga, Jorge H Melillo and Silvina Cerveny.
Accepted for publication in *Chemical Engineering Journal, 2023.*

This thesis has associated a patent already in deposit:

"*Composition for removing pharmaceuticals and heavy metals from polluted water*" Authors: J. Martinez Sabando, F. Coin, G.A. Schwartz, S. Cerveny. Submission number 300466912. Application number EP22383090.2, 2023. **Priority countries**: EU.

In addition, Javier Martinez Sabando has contributed to the following papers already published in topics intimately related with the topics of this thesis:

1) An In Situ Approach to Entrap Ultra-Small Iron Oxide Nanoparticles Inside Hydrophilic Electrospun Nanofibers With High Arsenic Adsorption
Nicolás Torasso, Alicia Vergara-Rubio, Reinaldo Pereira, Javier Martínez-Sabando, José Roberto Vega Baudrit, Silvina Cerveny and Silvia Goyanes.
Chemical Engineering Journal, **2023**, https://doi.org/10.1016/j.cej.2022.140168

2) Effect of Ferrocene on Physicochemical Properties of Biochar Extracted from Windmill Palm Tree (Trachycarpus Fortunei)
Abeer M. Adel, Javier Martinez – Sabando, Mona T. Al- Shemy, Silvina Cerveny
Waste and Biomass Valorization, **2023**, https://doi.org/10.1007/s12649-023-02201-9

Finally, part of this work was presented in the following conferences:

1. ***Dynamics of Adsorbed Water on Hydrogels for Water Remediation***
Javier Martínez-Sabando, Francesco Coin, Jorge H. Melillo, Silvina Cerveny.
12th International Conference on Broadband Dielectric Spectroscopy and its Applications.
September 4-10, 2022, San Sebastian, Spain . Poster.

2. ***Pectin-Based Adsorbents for Pharmaceutical Products Removal From Aqueous Media***
Javier Matínez-Sabando, Francesco Coin, Silvina Cerveny.
Workshop on Sustainable water management: use of Nanomaterials for water remediation-
ILSI-Lanotec, November 9, 2022, San José, Costa Rica Oral presentation

3. ***Simultaneous Removal of Zinc and Tetracycline From Aqueous Solution by Pectin-Based Adsorbent Crosslinked by Calcium and Europium***
Javier Martínez-Sabando, Silvina Cerveny

ECOSTP 2023, Junio 26-29,**2023**. Poster, Girona, Spain.

Acknowledgements

Primeramente, me gustaría agradecer a mi directora de tesis Silvina Cerveny. Ella me ha guiado y acompañado durante todo el proyecto durante mi formación como investigador. A lo largo de estos años he aprendido muchas cosas de diferentes ámbitos gracias a ella. También quisiera agradecer aa todos los integrantes del grupo "Polymer and Soft Matter" que en algún momento me han brindado su ayuda.

Quisiera agradecer a la fundación Materials Physics Center (MPC-BERC) por el contrato durante toda mi tesis. También quisiera agradecer el aporte económico de diferentes proyectos (Ministerio de Ciencia, Innovación y Universidades– Agencia Estatal de Investigación, PID2019-104650GB-C21 y CSIC, COOPB20502) que hicieron posible la realización del doctorado, ya sea para la compra de material fungible, insumos y alojamientos para la asistencia a congresos.

También me gustaría agradecer el apoyo técnico de Loli Martin y Juan Carlos Raposo de los servicios de SGIKER (UPV/EHU/ FEDER, EU) por la amabilidad, disponibilidad y paciencia que han demostrado siempre conmigo.

Me gustaría agradecer a varias personas que siempre han estado cerca de mi durante este proyecto, tanto en los buenos momentos como en los malos. Por ello la mención va para Mateo, Nico, Tristán, Juli, Flan, Alvar, Careli, Zuzu, Ima, Peru, Castel, Farru, Alvar, Dani, Orue, Andrea, Cy, Jorge, Maicol y a toda la gente de la cual me este olviando ahora. Gracias a todos por el apoyo.

Por otra parte también quería agradecer a toda la gente que he conocido durante la tesis, con la cual he compartido muy buenos momentos y que en algún momento me ha ayudado. Ellos son Coco, Cuate, Paula, Marito, Xavi, Thomas, Ali, Soheil, Isa, Amaia, Lorenzo, Claudia, Valerio, Andrea, Davide, Alejandro, Jordan y a los que posiblemente me olvidé.

Por último, me gustaría agradecer a las personas más importantes de mi vida, mi familia y Cris. Ellos siempre han estado cuando lo he necesitado y me han demostrado un amor y apoyo incondicional. Y por supuesto también a Verita!